Preface

The present thesis is the final result of a three-years Ph.D course in the frame of the research project PRA-IRIDYA (Integrated reconstructions of ice sheet dynamics during Late Quaternary Arctic climate transitions), coordinated by the National Institute of Oceanography and Applied Geophysics (OGS) with the collaboration of the Universities of Pisa, Ca` Foscari of Venice and the INGV of Rome.

The subject of this study are the episodes of rapid sea-level rise that occurred during the last 30 thousand years, associated with the decay through melting of the paleo Svalbard-Barents Sea Ice Sheet in Northern Europe. The main purposes include the definition and characterisation of the onset, dynamics, trigger mechanisms, and impacts of those events on the paleoenvironment and climate. To achieve these goals, a multi-proxy, sedimentological, micropaleontological and geochemical approach was applied to investigate three sediment piston cores collected along the Western margin of Svalbard and the eastern side of the Fram Strait representing the only deep-water connection between the North Atlantic and the Arctic Oceans.

Most of the analyses were carried out at the SEM and Micropaleontology Laboratory of the University of Pisa. Age calibration and modelling were performed at the Geography Department of the University of Cambridge during a period abroad in April 2024, whereas detailed work on plumites (laminas counting and statistical approach to determine astronomical cyclicity) was assisted during online meetings with Dr. M.E. Weber of the University of Bonn.

I. INTRODUCTION

1.1 A prelude of the Paleoclimatology

The search to understand the climate of the past started two centuries ago, when Agassiz (1840) was the first one to systematically propose the idea of past Ice Ages when large icesheets covered nonpolar areas (Ingólfsson and Landvik, 2013). At first that theory was not well accepted scientific community, but glacial striae and erratic boulders were recognized as unequivocal geomorphological evidence of former ice streams covering large areas in Europe (Torrel, 1878) and in Svalbard (De Greer, 1900). Futhermore, large coal deposits found in regions with incompatible climates were pointed out as clear indication of different former climate conditions and were used as argument by Koppen and Wegener (1925), to support the theory of continental drift from Wegener (1915). Those authors attributed the glaciationsduring the last 800.000 years to changes in solar radiation income. That point of viewwas followed by (Milankovitch, 1930), who theorised that the climate was controlled bycyclicity variations on the geometry of the Earth's orbit, causing changes on summer insolation at 65°N, which should be critical to the growth and decay of ice sheets duringPleistocene. However, testing Milankovitch's theory remained unfeasible for decades.

More evidence of paleoclimate conditions was only possible to achieve after the development of the piston coring technique (Kullenberg, 1948), during the Albatross Deep-Sea Expedition (from 1947 to 1948). Initially, the piston cores led to micropaleontological studies based on relative abundance of cold and warm-water foraminiferal species. Showing an alternation between colder and warmer climate stages in the past (Phleger, 1951; Schott, 1952; Arrhenius, 1953; Ericson, 1953; Hough, 1953; Phleger, Parker and Peirson, 1953). A system to designate those colder-warmer periods was proposed by Arrhenius, (1953), calling the present-day warm period as Stage 1, and using increasing numbers for the preceding stages. Thus, even numbers indicate cold periods, and odd numbers are used for warmer periods. Subsequently, 12 piston cores, including 8 from the Albatross expedition, were used by Emiliani, (1955), for oxygen stable isotopes analyses on foraminifera shells, which recognized the colder and warmer stages by the δO^{18} cyclicity along the Pleistocene period. Emiliani followed the system proposed by Arrhenius, (1953) and made the correlation between the Marine Isotope Stages with Milankovitch's theory, supporting the idea of summer insolation at 65°N as a prediction of word climate. Later, the δO^{18} Pleistocene cyclicity and its relationship with continental ice-sheets dynamics was confirmed and refined by (Shackleton, 1967).

Those pioneering works from the first half of the 20th century provided the fundamental tools for large scale paleoclimate research investigations. During the 1970s a major project called Climate Long-range Investigation, Mapping and Prediction (CLIMAP), was responsible for collecting several hundred of sediment cores around the world, opening space for extensive petrographic measurements and data processing to achieve quantitative data about climate and oceanographic changes like the Last Glacial Maximum (LGM) and the previous glacial and interglacial periods. Using two piston cores collected in the Southern Ocean during the CLIMAP, (Hays, Imbrie and Shackleton, 1976) performed δO^{18} measurements on planktonic foraminifera and radiolarian assemblages along a continuous climate record of the last 450.000 years. That study found that cyclicity in the earth's orbital precession (~21 ky), obliquity (~41 ky), and eccentricity (~100 ky) are the fundamental cause for the Quaternary ice ages (glacial stages), which was the final confirmation to the Milankovitch's theory.

Since 1968, international research projects focused on ocean drilling (e.g. DSDP, ODP and IODP) largely increased the number of sediment sampled sites through ocean drilling techniques allowing to read deeper (older) geological units. Many of these cored sites have been used for a better understanding of climate changes using marine isotope stages. By investigating piston cores from the Labrador Sea, Heinrich, (1988) recognized layers containing massive ice-rafted debris (IRD), revealing periods of greater iceberg discharge from the Laurentide Ice Sheet that were associated with the orbital precession cycle. Those periods, called Heinrich events (H1, H2, H3…) showed a good time matching with both summer maximum and minimum insolations, indicating that large deliveries of icebergs can occur during ice sheet growth but also during its fast retreat. Despite this ambiguous significance, IRDs have become another important paleoclimate proxy commonly used by many studies (e.g. Hald et al., 2004; Taylor et al., 2002), among many others).

Another major improvement to paleoclimate research was achieved when two sites located in the north area of the Greenland Ice Sheet were drilled down to the bedrock (Dansgaard et al., 1993) during the Greenland Ice-core Project (GRIP). Due to the seasonality of the ice accumulation, the ~3 km-long ice cores named GRIP and GISP2, revealed the highest resolution paleoclimate record ever recovered, spanning the last 250 ky. Results from the δO^{18} measurements of those ice cores identified up to 24 abrupt warming (interstadials) and cooling (stadials) events, that were named Dansgaard-Oeschger events (Dansgaard et al., 1993) occurring between the MIS-7 and the MIS-1. Those millennial scale climate cycles showed a good agreement with the Heinrich events recorded in the marine sediments. However, after extensive investigation (e.g. Grootes et al., 1993; Bender et al., 1994; Fuchs and Leuenberger, 1996; Chappellaz et al., 1997; Andersen et al., 2004), it became clear that ice flow caused deformation at the bottom of the ice sheet, and the record was fully reliable only for the last 105 ky. Later, another site thought to be less susceptible to ice flow, was drilled during the North Greenland Ice Core Project (NGRIP) that recovered a reliable record of the last 115 ky (Andersen et al., 2004). In the following, the lack of materials in the ice that could be dated with ^{14}C created the need to revisit chronological calibrations for the NGRIP core, which led to a new δO^{18} curve (T. L. Rasmussen et al., 2014).

After a century of studies, our scientific knowledge on Earth's past climate has become more consistent than ever, and it is now used to forecast future climate shifts related to the present global climate warming. One of the main present concern is the possibility that the ice loss from the Greenland and/or the West Antarctic Ice Sheets would lead to an abrupt acceleration of the relative sea-level rise, with consequent inundation of vast coastal areas and the possible abrupt slowdown of the Global Thermohaline Circulation (i.g. Golledge et al., 2019). Many feedback mechanisms in the climate system still need to be defined and improved. From this, the importance of studying the paleoclimate, the only that can provide us with empirical evidence capable of fuelling models and predictions for phenomena that may occur in the future.

1.2 The Last Glacial Maximum

The global ice sheets started to grow approximately 33.0 thousand years before present (cal ky BP) in response to a series of climate forcings that included reductions in summer insolation in the Northern Hemisphere at 65º latitude, lower atmospheric CO2 concentration (Clark et al., 2004; Clark et al., 2009), and Equatorial Pacific under La Niña like conditions, with sea surface temperatures decreased by >5 ºC from ~35 ka (Martínez et al., 2003). Furthermore, the gradual enlargement of the ice covered area created its own positive feedback by increasing the Earth's albedo, a key component of the surface energy balance over land (Betts and Ball, 1997; Clark, Alley and Pollard, 1999; Shakun, 2017). That cooling process led to the Marine Isotope Stage 2 (MIS-2), also commonly referred to as the Last Glacial Maximum (LGM), which was defined using low-stand sea-level records at the most recent period when global ice sheets reached their maximum volume (Mix et al., 2001; Clark et al., 2004), between 26.5 and 19.0 cal ky BP (Clark et al., 2009).

On Northern Europe, the high topography of the Scandinavian Caledonides maintained persistent mountain glaciers during most of the Quaternary period (Mangerud et al., 1996). Under cooling climate forcing those glaciers gradually become independent of altitude, forming the Fennoscandian Ice Sheet (Fredin, 2002). Geomorphological evidence of the last glaciation compilated by Hughes et al., (2015) indicates that such process started somewhere between 38 and 34 ky, followed by the establishment an ice-margin facing the North Sea at 32 ky. The latter occurred simultaneously to the surge of local icecaps over Svalbard, Novaya Zemlya and Franz Josef Land archipelagos, which enlarged over the Barents Sea until physically bond to each other and form the marine-based Svalbard-Barents Sea Ice Sheet (SBISIS) ~25.0 ky BP.

During the LGM, the Fennoscandian Ice sheet and the SBSIS were connected forming the Eurasian Ice Sheet complex approximately 24.0 cal ky BP (Jakobsson et al., 2014; Hughes et al., 2015; Patton et al., 2016; Brendryen et al., 2020; El bani Altuna et al., 2024). According to computational models, that complex reached the maximum ice volume of ~24 m of global sea level equivalents (s.l.e.) (Stouffer et al., 2006; Hughes et al., 2015). Meanwhile, a large portion of North America was coveredby the Cordilleran and the Laurentide Ice Sheets (Fig. 1.2.1). The latter by itself surely would have been much larger than the Eurasian complex, varying between 40 - 90 s.l.e, but its precise volume remains under a particular ongoing debate and (Licciardi et al., 1999; Dyke et al., 2002; Batchelor et al., 2019). Also, the Antarctic ice sheets were ~14.5 s.l.e. larger than today, but most of that would be in the marine-based West Antarctica (Bentley et al., 2014).

Furthermore, relative sea-level (RSL) data obtained from far-field sites at low latitude areas contains clear evidence of a drop of ~40 m occurred between 31 and 29 ky, that was followed by a steady fall until 21 ka, when global RSL reached a minimum of that varies from 124 m to 134 m below today's level (Fairbanks, 1989; Bard et al., 1996; Hanebuth et al., 2000; Lambeck et al., 2014; Cetto et al., 2024). However, RLS data from far-field sites and near-field sites (close to icesheets at High-latitudes) will always differ from each other due to isostatic responses of the solid Earth to the variations on ice unload. Also, those interactions between ice sheets, oceans and the solid Earth include distinct spatial variation on the gravity field and continental isostatic rebound (Milne and Mitrovica, 2008; Clark et al., 2009), and ocean thermal expansion (Alley et al., 2005).

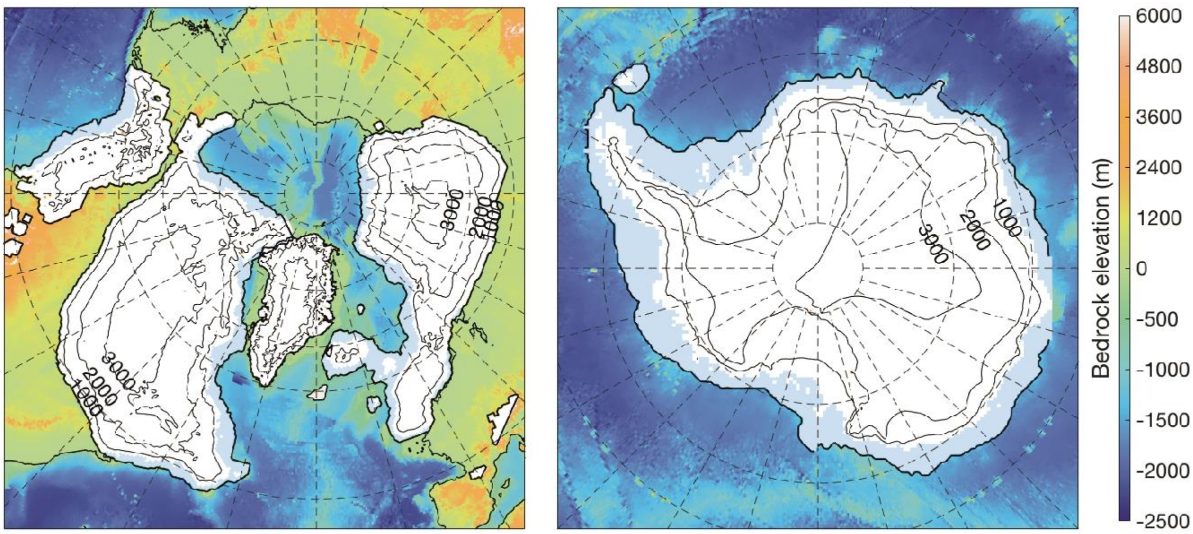

Figure 1.2.1: LGM ice thickness distributions from the ICE-5G reconstruction (Peltier, 2004). Image modified from Barends et al., (2018)

1.3 The Last Glacial Termination (T1) and the Meltwater Pulses (MWPs)

The Late-Quaternary, global glacial cycles varied between 80 and 120 ky in length, but they are typically composed of two asymmetrical phases: A longer cooling trend, that is usually punctuated by small warm periods, causing an oscillative buildup of ice sheets until the maximum ice volume is reached. Followed by an intense warming phase characterised by the global ice sheets collapse (Denton et al., 2010). In this context, the transition from the LGM (MIS-2) to the current interglacial (MIS-1) occurred between 19.0 and the onset of the Holocene period at 11.5 ky cal BP (Vilanova et al., 2019). Meanwhile, the collapse of glacial ice sheets has caused dramatic increases in freshwater flows to the oceans, disrupting ocean thermohaline circulation and global climate (Stocker and Wright, 1991; Manabe and Stouffer, 1995; Rahmstorf, 1995; Bard et al., 1996).

During the Last Glacial Termination, also known as the Termination 1 (T1), global temperature rises were not constant, and occurred in a series of millennial-scale climate shifts found in Greenland ice-core records (stadials-interstadials or Dansgaard-Oeschger events) (Johnsen et al., 1992; Dansgaard et al., 1993; Andersen et al., 2004; Andersen et al., 2004; Rasmussen et al., 2014). Those changes were also found in the Antarctic Ice Dome (EPICA community members, 2004; Shakun et al., 2012), and were followed by a series of steps-rises in atmospheric CO2 levels, with magnitude and pacing that suggest the deep-ocean as dominant source of Carbon (Broecker, 1982; Rae et al., 2014). Usually, changes in ocean circulation, mixing and deep-water formation are capable to induce to significant shifts in ocean-atmosphere carbon transfers (Knox and McElroy, 1984; Sarmiento and Toggweiler, 1984; Seigenthaler and Wenk, 1984; Sigman et al., 2010; Skinner et al., 2010).

As a direct consequence to those global-scale climate changes, the ice-sheets started to decay, leading to RSL rises. The first continuous record of sea-level changes occurred after the LGM was provided by drilling the Caribbean reef-crest of coral Acropora palmata, offshore Barbados (Fairbanks, 1989). Followed by many authors that investigated drowned reef-crest sequences in mid-low latitude areas around the globe, such as Tahiti (Bard et al., 1996; Montaggioni et al., 1997), Sunda Shelf (Hanebuth et al., 2000), Hawaii (Webster et al., 2004) and Brazil (Cetto et al., 2024). Those systematic studies proved that Late-Quaternary sea-level rise was not steady or gradual but marked by a sequence of rapid episodes or Meltwater Pulses (MWPs). By definition, MWPs are short-lived global accelerations in sea-level rise resulting from intense glacial melting, surge of ice streams into oceans and/or intense iceberg discharge during ice sheet disintegration (Blanchon, 2011; Harrison et al., 2019). After the LGM, four of those abrupt events are described to occur: MWP-1A0, MWP-1A, MWP-1B and MWP-1C. Each one of these abrupt events interfered directly on global climate by interfering with ocean thermohaline circulation, and that deeply changed the Earth' physiography.

1.3.1 MWP-1A$_0$

Characterised by a Relative Sea Level (RSL) rise between 10-15 m within a few hundred years caused by a rapid decrease of ~10% in global ice volume, this event is also known as MWP-19ka. It is considered as a tipping point that marks the transition between the LGM and the T1 onset that occurred between 20 and 19 ka BP (Blanchon and Shaw, 1995; Clark et al., 2004; 2009) The current knowledge about the MWP-1A$_0$ correlates it with an increased summer insolation at 65ºN and higher concentrations of atmospheric CO2 (Yokoyama et al., 2000; Clark et al., 2004; Alley et al., 2005; Rinterknecht et al., 2006; Hanebuth et al., 2008; Crocket et al., 2011). That huge amount of fresh cold water interfered with the Atlantic Meridional Overturning Circulation (AMOC) and increased sea-ice covering in the Northern Hemisphere, which would have acted as the negative feedbacks that caused a cold period record in Greenland ice cores called Oldest Dryas (Buizert et al., 2014).

1.3.2 MWP-1A

The second MWP occurred after the LGM was initially discovered with drill-cores on coral skeletons from Barbados by (Fairbanks, 1989), and from the Caribbean by (Blanchon and Shaw, 1995; Bard et al., 1996). Although the sources, magnitude and timing of the MWP-1A have been a subject of controversy over the past decades (Clark et al., 1996, 2002; Hanebuth et al., 2000; Alley et al., 2005; Bassett et al., 2005; Bentley et al., 2010; Deschamps et al., 2012; Lucchi et al., 2013, 2015; Golledge et al., 2014; Brendryen et al., 2020).

Precise radiocarbon dating on samples from the Tahiti cores at a subsidence-corrected depth of 88 m below current sea-level revealed unequivocal evidence of an in-growth position coral-reef colonising a pre-glacial sub-stratum after the major sea-level jump occurred during Late-Quaternary between 14.65 and 13.31 ky BP (Deschamps et al., 2012) (Fig.1.2.3).

However, due to differences in neo-tectonic settings (subsidence and uplifting) between different far field sites, the magnitude of this rise is still debated. Early conservative estimates pointed to a RSL from 14 to 18 m (Blanchon and Shaw, 1995), while other studies suggested a range between 18 and 22 m, with an average of 20 m (Deschamps et al., 2012). Therefore, the rising rate is something between 40 and 60 mm per year, during that 340-year interval (Bard et al., 1990, 1996; Weaver et al., 2003; Fairbanks et al., 2005; Stanford et al., 2006; Deschamps et al., 2012; Lucchi et al., 2013; Brendryen et al., 2020). More recent reconstructions applying computational modelling clearly pointed to the Laurentide ice sheet as the major source for the event, while the ice-sheet complex that was covering Scandinavia and the Barents Sea would have contributed 20 to 35% of the total RSL rise, which is equivalent to 3.2 - 6.4 m of rise (Lin et al., 2021).

Furthermore, the MWP-1A is associated with a strong climate event recorded in Greenland ice sheet known as Bølling Warming or Greenland Interstadial 1 (Bond et al., 1993; Dansgaard et al., 1993; Weaver et al., 2003; Seierstad et al., 2005; Rasmussen et al., 2007; T. L. Rasmussen et al., 2014).

1.3.3 - MWP-1B

The third sea-level jump during T1 was the MWP-1B, and it is clearly the most controversial of its kind. Originally this event was recognized on different depths of the same two drill-cores from Barbados that found the MWP-1A (Fairbanks, 1989), then in

Barbados (Bard et al., 1996), but the precise amplitude and time hiatus between both events remained controversial, and it was the subject of several studies (Edwards et al., 1993; Liu and Milliman, 2004; Bard et al ., 2010; Blanchon, 2011). The time hiatus problem was solved when the end of the MWP-1A was better established to have occurred at 14.31 cal ky BP by (Deschamps et al., 2012). Hence, the 1B would have occurred between 11.50 and 11.10 cal ky BP, at the beginning of Holocene, but establishing the forcing trigger mechanisms and hemispheric origin of the MWP-1B continued to be discussed, and there is no orbital forcing explanation for the 1A-1B separation (Bard et al., 2010; Whitehouse and Bradley, 2013; Harrison et al., 2019).

Also, the relationship between this event and the Younger Dryas cold period (YD) that was recorded shortly afterwards remains not completely understood, partially due to the lack of sedimentological evidence of the MWP-1B, especially in the North Atlantic, where ice-sheets readvanced during the YD (Bard et al., 2010).

1.3.4 MWP-1C

Unlike the events that preceding events, the last meltwater pulse episode occurred already during the Holocene period, approximately 8.2 ka BP, and would have been caused by a catastrophic drainage of the proglacial Lake Agassiz-Ojibway originated from the melting of the Laurentide ice sheet (Kleiven, Kissel and Laj, 2008; Törnqvist and Hijma, 2012). The MWP-1C is clearly the smallest among the Late Quaternary sea-level jumps, nevertheless it has contributed with a RSL of 6 m occurring in a much shorter time-period (Bird et al., 2010; Cetto et al., 2024), being the most intense climate episode of the last 10 ky.

This kind of abrupt freshwater release reduced the North Atlantic deep water formation, and AMOC activity (Rohling and Pa, 2005). Also, Greenland Ice-core evidence indicates a strong atmospheric response to the event, including a temperature drop, with reduced methane concentrations, less moisture and stronger winds (Alley et al., 1997; Spahni et al., 2003; Kobashi et al., 2007). Those climate changes certainly affected early human societies.

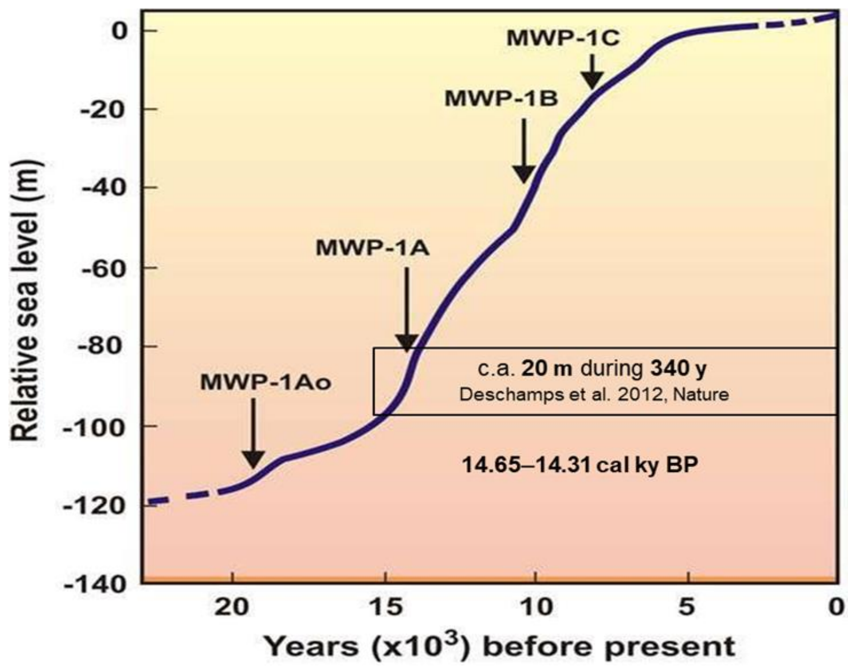

Figure 1.3: Simplified Sea-level curve since the LGM from (Gornitz, 2007). *Downloaded on October, 2024 from: https://www.giss.nasa.gov/research/briefs/archive/2007_gornitz_09/.*

1.4 The High-latitude sedimentological climate archives

High-resolution radiocarbon dating of low-latitude coral skeletons permits precise timing of the MWP events. Although, diffuse neo-tectonic uplift of these areas often led to controversial correlating results and difficult calculation of the magnitude of those events (Lucchi et al., 2015). To solve that problem and recognize which ice-sheet was the source of each event, the investigation of polar sedimentary archives is required. Therefore, during the last decades the sedimentary records from the South-Western margin of Svalbard have been widely investigated to understand the paleoclimate changes associated with the last glacial-interglacial cycle (Elverhøi et al., 1995; Laberg and Vorren, 1996; Vorren and Laberg, 1997; Landvik et al., 1998; Jessen et al., 2010; Pedrosa et al., 2011; Lucchi et al., 2013, 2015; Nielsen and Rasmussen, 2018).

The first clear sedimentological evidence of the Late-Quaternary MWPs found in the Arctic polar records occurred in 2013 (MWP-1A), by (Lucchi et al., 2013), and the MWP-1A$_0$, by (Caricchi et al., 2019). Since then, many other scientists focused on the recovery of the marine evidence of MWPs, trying to identify the initiation area of the major events, the trigger mechanisms, and the effects on the global thermohaline ocean circulation and climate (Nielsen and Rasmussen, 2018; Bellwald et al., 2020; Brendryen et al., 2020; Lin et al., 2021). Many of those studies have recognized Mass Transport Deposits (MTD) of Glaciogenic Debris Flows (GDFs) along the continental slope Those deposits clearly indicate that the Svalbard-Barents Sea Ice Sheet (SBSIS) reached the shelf-edge under full glacial conditions somewhere between 24 and 20 ky BP, (Jakobsson et al., 2014; Patton et al., 2017; El bani Altuna et al., 2024). On the other hand, MDTs disrupt the stratigraphic records by reworking the sediments. To avoid the issue, a few studies recovered continuous sequences at sites beyond the continental slope, in deeper areas of the Fram strait (Hebbeln, 1992; Hebbeln et al., 1994; Dokken and Hald, 1996), but lower sedimentation rates on those deep areas reduces the resolution of the record. Only a small number of studies from this area have recovered continuous and expanded stratigraphic sequences containing MWP events records without MTDs disturbance during the LGM (e.g. Müller et al., 2009; Müller and Stein, 2014; Caricchi et al., 2019).

1.5 Research objectives and thesis organisation

The present study is composed of high-resolution results from a multi-proxy investigation through the LGM and T1 sedimentary records, recovered in 3 marine piston cores collected expanded depositional sequences associated with the depocenters of the Bellsund and Isfjorden sediment drifts on the western margin of Svalbard (Rebesco et al., 2013).

The core IRIDYA-02 was studied for the first time during the present investigation, while the core GS-02 have been already used for palaeomagnetism studies (Caricchi et al., 2019, 2020), and the CAGE-15 was used for clay minerals assemblage and sedimentary provenance (Douss, 2023). Although, the present thesis has incorporated from those previous investigations only the core log visuals descriptions, the physical properties measurements, and seven raw age-dated results of the core GS-02 from Caricchi et al., (2019), that were recalibrated with more recent techniques, which will be detailed described in chapter 1.

A highly accurate chronology for the MWP and Heinrich-like events is provided from a Bayesian age-depth model built with AMS radiocarbon on *Neogloboquadrina pachyderma* and considering a variable regional ^{14}C reservoir effect for each dated level. Furthermore, stable isotopes ($\delta^{18}O$) variations, and depositional fluxes of Ice-Rafted Debris (IRD) and planktonic foraminifera (PF) were calculated over time, revealing new evidence of the interaction and mutual feedback between climate, oceanographic conditions, and ice sheet dynamics in the Arctic. Together, those proxies revealed periods of sea-ice free conditions and high primarily productivity next to Svalbard immediately before each ice-sheet collapse. Those conditions can only be explained by a regional-scale polynya and/or the arrival of North Atlantic relatively warmer waters. In both scenarios deep-water formation would lead to AMOC activity, which is the stronger heat-transfer mechanism from low to high latitudes.

The original results from this thesis shows the time interval between trigger mechanisms and the start of the events. Furthermore, the internal dynamics of the MWP-1A was accessed with a combination of precise age-depth modelling and X-ray image processing, which revealed for the first time which was the most intense period of the event.

As the investigation of the sediment cores includes a variety of different analyses, this thesis has been divided into three main chapters, briefly outlined in the following:

II. Physical Settings of the Study area

2.1 Geological background

The evolution of the Fram Strait, located between Svalbard archipelago and Greenland, played a crucial role in ocean dynamics connecting the Atlantic and the Arctic oceans (Hossain et al., 2021). The opening of this getaway started approximately at 21 Ma, during the early Miocene, with a narrow and shallow water passage (Jokat et al., 2016). The initial opening was followed by a very slow tectonic spreading with strike-slip movements caused by the active ocean ridge systems in the Greenland-Iceland-Norway (GIN) Seas (Gruetzner et al., 2022). It was only at the Late Miocene, around 6 Ma, when the passage has become wide and deep to allow deep ocean circulation between the North Atlantic and the Arctic oceans (Jakobsson et al., 2007; Knies et al., 2014; Stärz et al., 2017). The increasing water mass exchange within the Fram Strait caused a significant influence on the paleoceanographic and paleoclimatic conditions of the Northern Hemisphere (Thompson et al., 2012), with the enhanced contribution of the North Atlantic thermohaline circulation (Knies et al., 2014; Stärz et al., 2017; Bellwald et al., 2020; Hossain et al., 2021).

At the eastern side of the Fram Strait, glacial deposition of sediments eroded from Svalbard stated in the Early-Quaternary, ~2.3 Ma (Faleide et al., 1996), and the Svalbard-Barents Sea Ice Sheet (SBSIS) reached the continental shelf-edge for the first time somewhere between 1.5 and 1.5 Ma, delivering glaciogenic sediments to the upper slope (Butt et al., 2000). Since then, the seafloor morphology at western margin of the Svalbard is the result of repeated advances and retreats of the Ice sheet, during the Late-Quaternary climatic changes (Patton et al., 2016).

Along polar continental margins, ice streams are the main drivers of erosion, transport, and sediment deposition (Gales et al., 2019). During full-glacial periods, those fast-flowing outlets of ice sheets erode cross-shelf bathymetric troughs and deliver enormous quantities of terrigenous glaciogenic debris directly to the shelf edge, which increases oceanward progradation of the continental margin by building fan-shaped piles of highly consolidated detritus (glacigenic diamicton) called Trough Mouth Fans (TMF) (Vorren et al., 1989; Vorren and Laberg, 1997; Laberg et al., 2012; Lucchi et al., 2013; Rebesco et al., 2013; Ó Cofaigh et al., 2013; Gales et al., 2019; Bellwald et al., 2020).

Deposition on TMFs is controlled by meltwater-dominated fans and Glaciogenic Debris Flows (GDF), both accumulated in very short time periods (Bellwald et al., 2020). The meltwater-dominated fans take place under subglacial conditions when MWPs generate hyperpycnal flows and consequently, turbiditic sequences (Lucchi et al., 2013; 2015). At the same time as sediment plumes are being released and deposited, causing high sedimentation rates (Knutz et al., 2002; Tripsanas and Piper, 2008; Lucchi et al., 2013; Ó Cofaigh et al., 2013, 2018; Laberg and Dowdeswell, 2016; Bellwald et al., 2020). The GDFs are originated when the sediment accumulated at the upper slope by ice streams became unstable and flows down-slope. With run outs that can be up to hundreds of kilometres, GDF deposits are poorly sorted, matrix supported with sand content up to 40% (Vorren and Laberg, 1997; King et al., 1998; Dimakis et al., 2000; Nygård et al., 2005; Tripsanas and Piper, 2008; Dowdeswell et al., 2008; Laberg et al., 2012; Ó Cofaigh et al., 2013; Baeten et al., 2014; Laberg and Dowdeswell, 2016; Rashid et al., 2019; Bellwald et al., 2020).

At the Western margin of Svalbard, the Isjorden and Bellsund TMFs cross the relatively narrow continental shelf as extensions of the main fjords of the Spitsbergen Island. Further south, the Storfjorden is the biggest TMF of the study area, with a radius of ~175 km, once it has a bigger paleo-ice drainage covering 82500 km2 over the Barents Sea (Laberg and Vorren, 1995, 1996; Dimakis et al., 2000; Ottesen, Dowdeswell and Rise, 2005; Andreassen et al., 2008; Pedrosa et al., 2011). The sediment accumulated on those concentrically marine deposits are constantly exposed to oceanic bottom currents that transport material along the continental slope, mounding depocenters in between the TMFs, in areas that are mostly protected from direct glaciogenic input from the ice sheet during glacial periods known as Contourite drifts (Lucchi et al., 2013; 2015; Rebesco et al., 2013). Therefore, the Isfjorden and Bellsund drifts are the specific locations where the sediment cores used during this study were taken.

Contrarily to the continental shelf, which is periodically affected by grounded ice sheet erosion during glacial maxima, and the TMFs which are continually reworked by gravitational process and slope instability, the Contourite drifts at deep-sea continental margins are characterized by continuous deposition with alternation of glacially derived sedimentation and bottom current deposition, containing high-resolution paleoclimate records and valuable information about the paleo SBSIS dynamics in response to past environmental conditions, climate changes and meltwater events associated with the decay of the SBSIS (Lucchi et al., 2013).

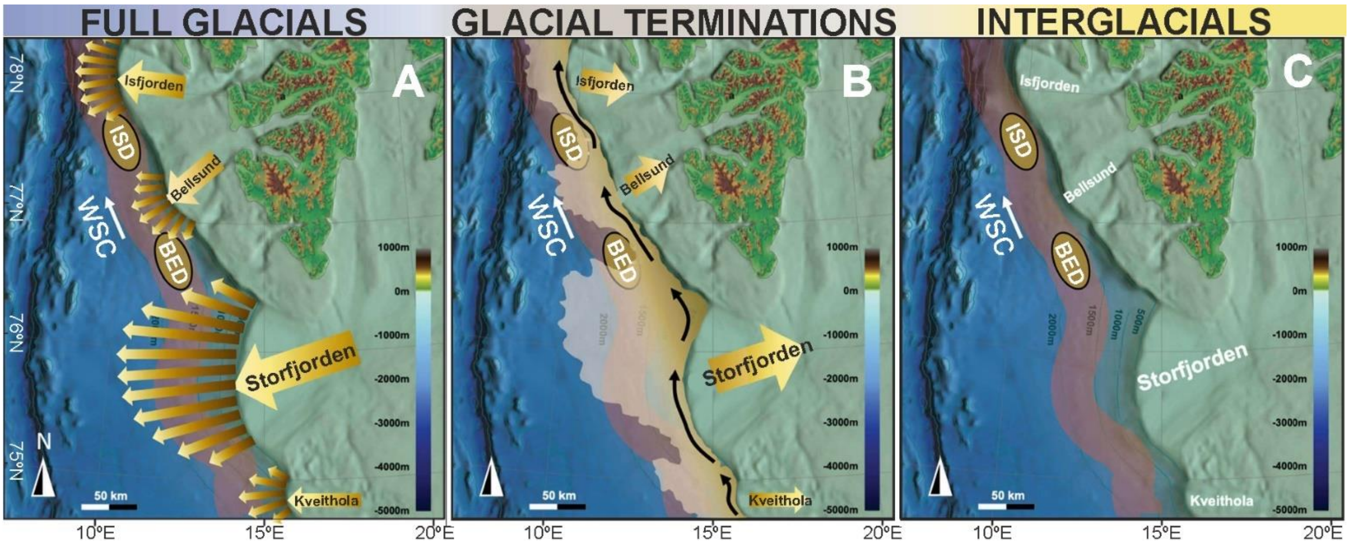

Figure.2.1 Image modified from (Lucchi et al., 2023). Larger golden arrows indicate advances and retreats of ice streams. Thin golden arrows indicate depositional processes contributing sediments to contourite depositional system deposit, BED = Bellsund drift, ISD = Isfjorden drift, WSC = West Spitsbergen Current.

2.2 Ocean Circulation

The north-western continental margin of the Barents Sea represents one of two gateways for flux of warm water from middle latitudes to the Arctic Ocean (Schauer et al., 2004; Melis et al., 2018). The main oceanographic current in the Storfjorden area is the West Spitsbergen Current (WSC) (Nilsen and Nilsen, 2007; Nilsen et al., 2016), a saline, shallow and relatively warm current which is the northernmost extension of the Norwegian Atlantic Current (NwAC), flowing northward along the continental slope. After reaching the Arctic Ocean, the WSC mixes with polar waters, splits into the northern Spitsbergen margin, and flows back to the Storfjorden Trough along the eastern and southern margins of Spitsbergen islands (Melis et al., 2018). Therefore, it becomes the East Spitsbergen Current (ESC), a cold deeper low salinity coastal current) (Johannessen, 1986; Melis et al., 2018) (Fig.2.1.2).

The WSC is the main provider of oceanic heat to the Arctic Ocean (Nilsen et al., 2016), flowing at 0,25m^{s-1}, following the 1000 m isobath (Boyd and D'Asaro, 1994). Beneath the WSC, there is the colder and fresher Norwegian Sea Deep Water (NSDW) influenced by water contribution from Greenland Sea and Eurasian Basin (Swift and Koltermann, 1988; Boyd and D'Asaro, 1994; Bensi et al., 2019).The influx of relatively warm and saline Atlantic Water toward the Arctic plays a very important role on the climate conditions of the environment (Melis et al., 2018). However, the influx velocity presents significant variations over time (Rahmstorf, 2002; Rasmussen and Thomsen, 2008; S´ lubowska-Woldengen et al., 2008; Risebrobakken et al., 2011; Kristensen et al., 2013; Werner et al., 2013; Melis et al., 2018). In this respect, the NW Barents Sea margin is a key area for the study of the paleoceanographic and paleoenvironmental conditions during the LGM and T1.

At the present-day, deep-water formation to the depths greater than 2000m takes place in the North Atlantic and Southern Oceans, been also part of the mechanisms that explain deglacial climate and CO2 change at these regions (Toggweiler et al., 2006; Sigman *et al.*, 2010; Rae *et al.*, 2014). During the LGM, atmospheric CO2 levels rose in a series of steps, associated with millennial-scale shifts in global climate (Shakun et al., 2012; Rae et al., 2014). As only the ocean carbon reservoir is enough large and dynamic to drive such strong variations in glacial-interglacial timescales (Hain et al., 2010), the magnitude and pacing of CO2 rise point to the deep ocean as the dominant source of carbon to the atmosphere (Sarmiento and Toggweiler, 1984; Seigenthaler and Wenk, 1984; Sigman et al., 2010; Sarnthein and Grootes, 2013; Rae et al., 2014).

2.3 The settling of the cores

The cores were taken on the middle-slope portion of this margin, between 1322 m and 1725 m water depth (Table 1). The sites were selected based on previous seismic acquisition on the study area performed during the SVAIS cruise onboard the R/V

Hesperides (2007) and EGLACOM cruise (2008) onboard the R/V OGS-Explora. Detailed seismic interpretation on deep-direction profiles were used by Rebesco et al., (2013) to characterize the Isfjorden and Bellsund drifts as undisturbed continuous stratigraphic sequences. Sub-bottom profiles were also performed during the research cruises when the studied sites were cores (Fig. 2.1.3).

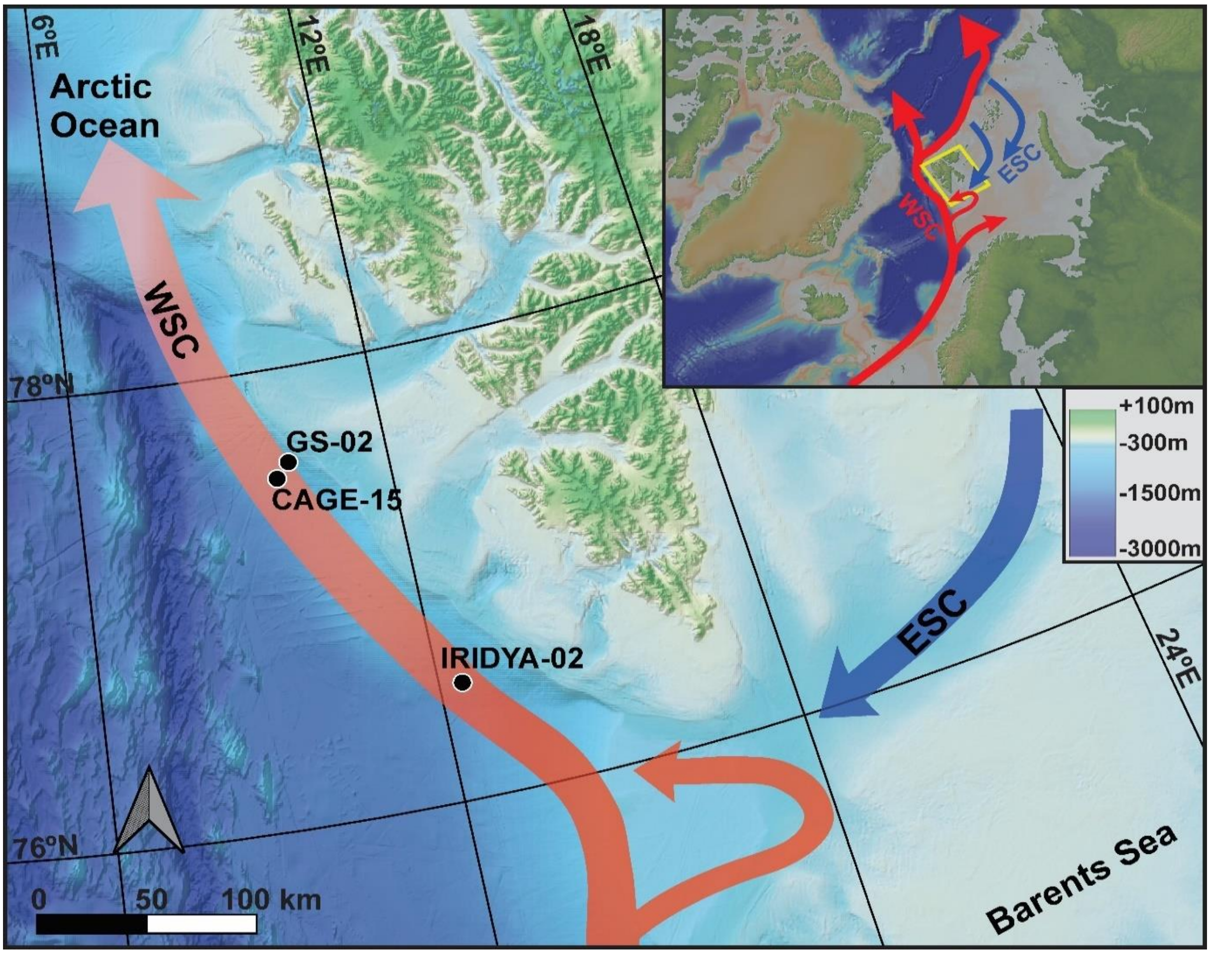

Figure 2.1.2: Study area location map. Black dots indicate the sites of IRIDYA-LB21-02PC (IRIDYA-02), CAGE-19-3KH-15GPC (CAGE-15) and GS191-02PC (GS-02) cores. Red arrow: West Spitsbergen Current (WSC). Blue arrow: East Spitsbergen Current (ESC). Bathymetric data from (Jakobsson et al., 2020). Produced using QGIS. (QGIS Development Team, (2009).

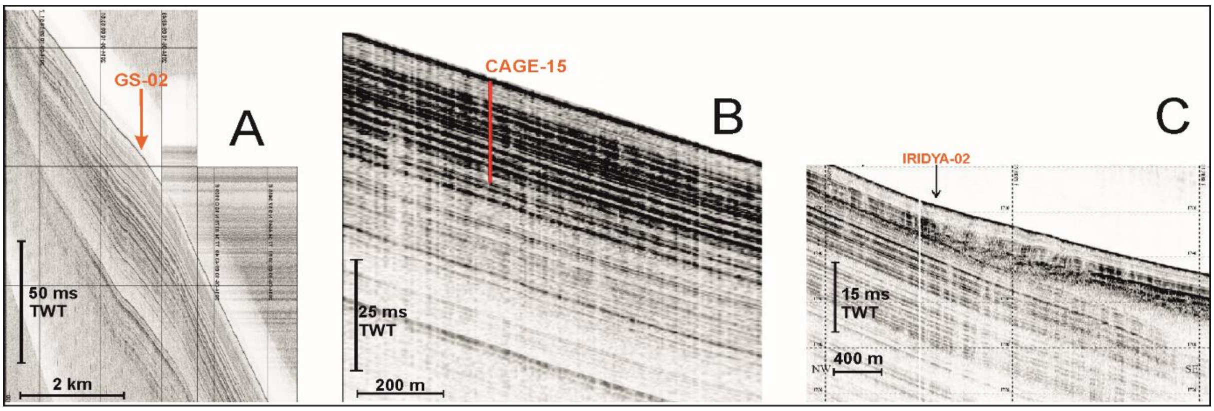

Figure 2.1.3: Sub bottom profiles of the core sites. A: Modified from Lucchi et al., (2014). B: Modified from Knies and Vadakkepliyambatta, (2019). C: Modified from Lucchi et al., (2021).

Chapter 1 - The chronology

1.1 Introduction

Since one of the major goals of this PhD thesis is to build a paleoclimatic and paleoceanographic reconstruction of the last glacial termination T1 and the LGM, a precise chronology control (age-depth model) of the sediment cores is a fundamental aspect of the study. Also, the chronology was used to link different kinds of proxies and better understand the records. Consequently, it makes more sense to start by explaining how the age dating, calibration and age-depth modelling were performed. Only Accelerator Mass Spectrometry (AMS), radiocarbon (^{14}C) dating from intact planktonic foraminifera shells of *Neogloboquadrina pachyderma* were used for this study.

The calibration and modelling steps of this study were performed during a period abroad at the Geography Department of Cambridge University (UK), during April 2024, under the supervision of the professor Dr. Francesco Muschitiello and Dr. Marco Aquino Lopez.

1.1.1 The Radiocarbon method

The nature of the radiocarbon (^{14}C) and its potential to determine the age of organic material have been discovered during a sequence of studies (Libby, 1946; Anderson et al., 1947; Libby et al., 1949; Zeuner, 1950), led by Dr. Willard F. Libby, who was awarded with a Nobel Prize in Chemistry for that contribution. This method has started a revolution in multiple research fields, becoming a standard tool in environmental sciences. Briefly, radiocarbon atoms are produced by the continuous bombardment of high-energy particles (mostly originated from the Sun) to the Earth. Those cosmic rays collide with atoms of our atmosphere, which knock loose protons. When a free proton collides with the nuclei of a Nitrogen atom, it turns into ^{14}C, a radioactive isotope that become oxidized to CO2 gas and join the Earth's carbon cycle being absorbed by the living organisms and has a half-life of 5730 years (Broecker, 2013).

Initially, ^{14}C dating was tested assuming that in all cases, the carbon exchange system was in isotopic balance, and positive results were obtained due to an equilibrium identified between tree-rings of a giant sequoia and atmospheric CO_2, both from in the year 1890 AD (Willis et al., 1960). However, it subsequently became clear that timescales in radiocarbon years were not identical to calendar years when using older known age samples. Thus, the initial assumption of an isotopic balance was not valid for the past and neither between ocean and atmosphere (De Vries, 1958). Therefore, a ^{14}C reservoir effect (ΔR) should be considered to calibrate any raw data (Stuiver and Polach, 1977). Since then, the ^{14}C calibration problem and the effort to precisely calculate ΔR has become a key aspect to paleoenvironmental sciences because each environment can have a particular reservoir that changes during time.

Nowadays, ~70% of the ^{14}C found on our planet is located in the deep oceans, and it has a ~16% lower $^{14}C/C$ ratio than the atmospheric CO_2 due to the loss by radio decay (Broecker, 2013). Thus, ocean circulation and water mixing plays a very significant role in the system. Periods with slower mixing due to strong water stratification causes a higher contrast between deep waters and atmospheric $^{14}C/C$ ratios. Consequently, meltwater releases during glacial terminations strongly interfere with the carbon cycle, and its effects are more pronounced at high-latitude marine environments. The release of meltwater causes intense water stratification, reducing the deep-water formation, weakening thermos-hyaline circulation, and delivering into the ocean great amounts of organic matter eroded from the ice-sheet catchment area (Skinner et al., 2017).

1.1.2 Calibration curves and the reservoir effect

During the last decades, extensive improvements in Accelerator Mass Spectrometry (AMS) combined with the rising number of studies dedicated to this matter (e.g. (Bard et al., 2004; Telford., 2004; Skinner et al., 2017; Brendryen et al., 2020; Heaton et al., 2020) resulted in different calibration curves to specific geographical targets. The *IntCallXX* and *SHCallXX* (where XX indicates the year in which the calibration curve was made), were respectively designed for Northern and Southern Hemispheres atmospheric reservoir effect. Whilst, for the marine environment, the commonly used curve is called *MarineXX*. Furthermore, each one of those curves is periodically actualized, and the current versions available are the *Marine20* (Heaton et al., 2020), *IntCall20* (Reimer et al., 2020), and *SHCall20* (Hogg et al., 2020). All three of them reach the age 55.0 ky, which is approximately ten times the ^{14}C half-life. Together, they provide a practical way to calibrate age-dating results but regional to local scale reservoir effects (ΔR) are naturally softened or not well recognized by those global-scale curves. Hence, a regional curve should be used, when available.

Those global calibration curves can be used through a variety of softwares specifically develop for this purpose, which are available online (i.e. *Oxcall* and *Calib*). These programs always require four basic pieces of information from the user:

- the raw age dating result with its error (standard deviation),
- the ΔR, and the ΔR standard deviation (ΔRstd).

Also, some of those programs offer a tool to calculate the present day ΔR and ΔRstd values for the selected region, using other data from the vicinity, if available. However, the use of present day ΔR values to calibrate samples of organic material that lived in the past, under different reservoir conditions is just not realistic because it overlooks the natural dynamics of the carbon cycle. For the same reasons, applying the same ΔR for multiple samples with different ages (different depths in a core) should be avoided, especially at high latitudes, where the ΔR variations are predominantly driven by enlarged sea-ice cover during glacial periods. Since the sea-ice is impermeable for

CO_2 and restricts air-sea gas exchange, it can strongly reduce the uptake of new atmospheric ^{14}C into the ocean (Heaton et al., 2023). Therefore, the ΔR values can vary from ~80 years (present day Atlantic Ocean reservoir effect at 60ºN) (Fig.1.1.2.1), to over 1750 years during the LGM on the same region (Fig. 1.1.2.2) (Key et al., 2004; Skinner et al., 2017). These variations are the reason why the use of *MarineXX* to calibrate samples from outside the 40ºN-40ºS range without adjustments is not recommended (Heaton et al., 2020; 2023).

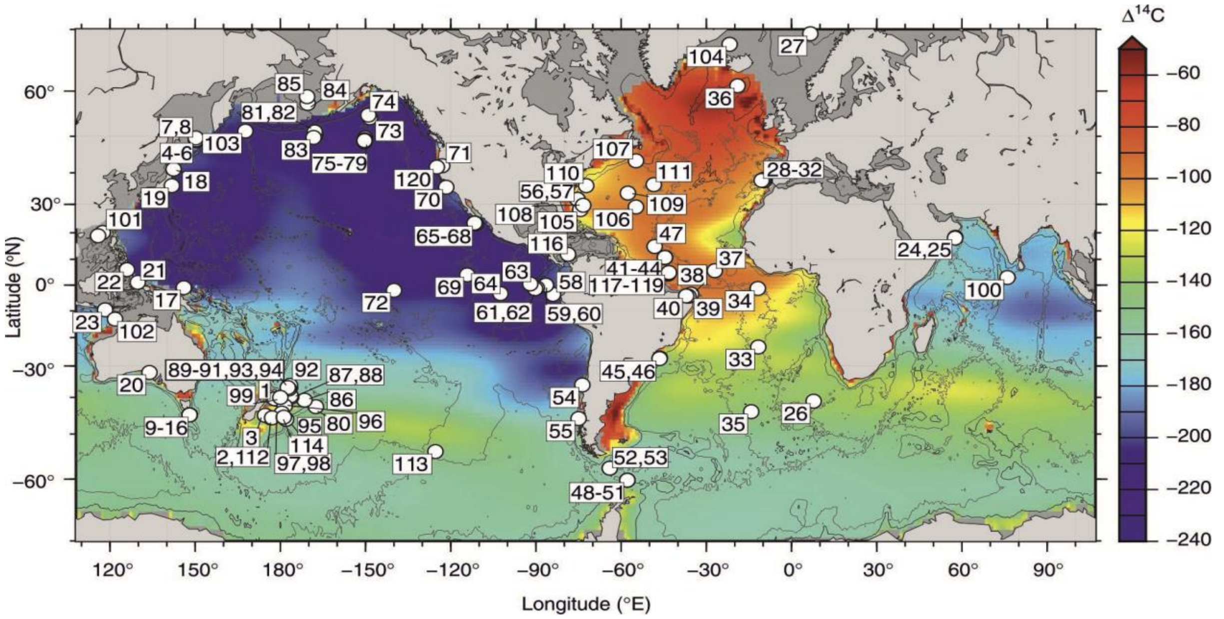

Figure 1.1.2.1: Modern marine radiocarbon reservoir effect measurements (white boxes) from (Skinner et al., 2017), plotted over radiocarbon effect global model (color background) from (Key et al., 2004).

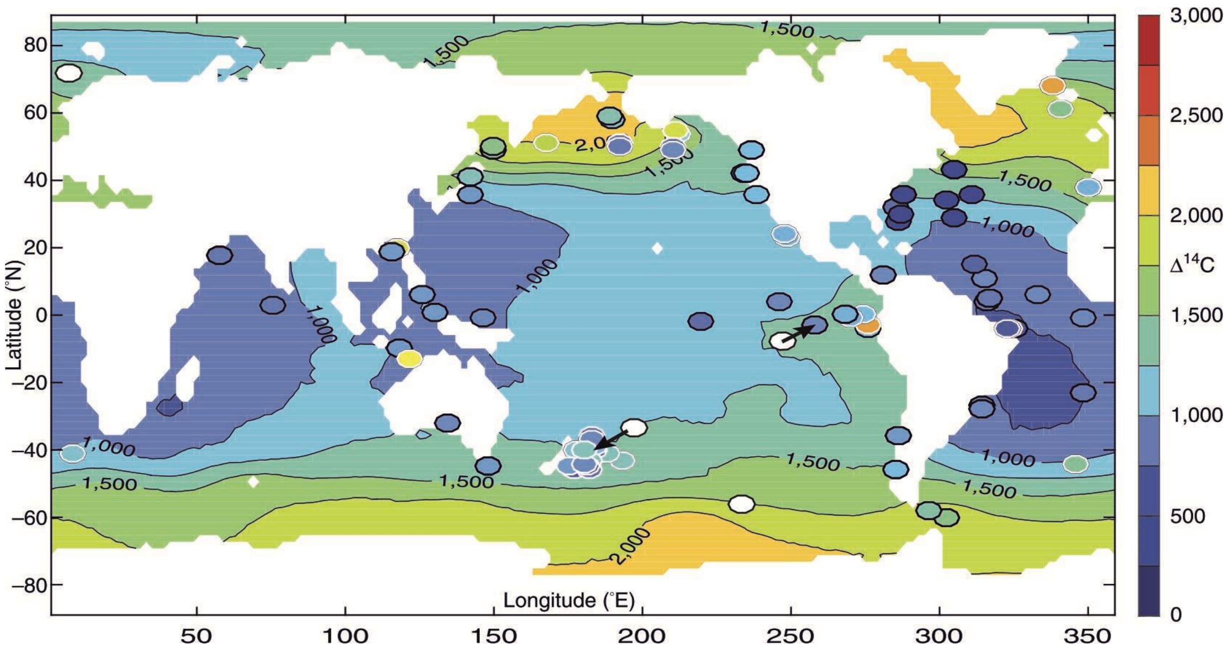

Figure 1.1.2.2: Ocean surface reservoir ages during the LGM period from Skinner et al., (2017).

Hence, the most adequate procedure for ^{14}C age calibration on polar areas is the use of a regional calibration curve, but also considering a variable ΔR effect overtime, which can be done by calculating the difference between the global and the regional calibration curves values for each age-dated interval.

1.1.3 Adopted approach to solve the calibration problem

Since, the ^{14}C dating method is only applicable for materials with no more than 55 ky of age, the Last Glacial Termination (T1) is the most sensitive time interval for this chronological method. As explained above, polar regions present particularly pronounced reservoir effects with significant shifts during meltwater release and sea-ice variations. For those reasons, the present study deals with the calibration problem in one of the most critical conditions, searching for a precise chronological constraint of the trigger mechanisms associated with some of the known most intense sea-level rise events that occurred during the Late Quaternary. Hence, the most sophisticated approach available was applied, taking advantage of the existence of a regional calibration curve recently built for the Norwegian Sea, the *Normarine18* (Brendryen et al., 2020), and using the global calibration curve *Marine20* (Heaton et al., 2020), to calculate a variable ΔR and its standard deviation (ΔRstd) for each dated level of the studied cores. Furthermore, Bayesian statistics were applied to build age-depth models for the cores allowing the understanding of the other data of this thesis during time.

1.2 Materials and Methods

In this thesis, the ΔR of the south-west margin of Svalbard was determined using the difference between two calibration curves, the *Marine20* (Heaton et al., 2020), and the *Normarine18* (Brendryen et al., 2020). For each dated sample, a specific ΔR was calculated by subtracting the uncalibrated ^{14}C values for the same calendar year before present on those curves. As the ΔR on both curves has it owns standard deviations (ΔRstd), it was necessary to calculate also the difference between them by combining the errors of both curves using the geometric mean following the equation:

$$\Delta R\ std = \sqrt{Marine20\ std^2 + Normarine18\ std^2}$$

Once the specific ΔR and ΔRstd were calculated, the raw data was calibrated to the calendar year (1950 AD) using the online software Oxcall V4.4 (Ramsey, 2009). Ten and three samples, respectively collected from cores CAGE-15 and IRIDYA-02, were selected for AMS ^{14}C radiocarbon dating on monospecie planktonic foraminifera tests of *Neogloboquadrina pachyderma* (Table 3). This work also includes six radiocarbon results from the core GS-02, previously measured in the same laboratory (NOSAM in Woods Hole Institute) and previously published by (Caricchi et al., 2019; 2020).

In Table 2 we reported the calibrated age range of ±1σ and ±2σ. However, in this study we have considered the median probability of the probability distribution as suggested by Telford et al., (2004) and the ages will be indicated as Cal yr BP or Cal ky BP. The three topmost age-dated samples on the core GS-02, and the lowermost on the CAGE-15 resulted out of the available *Normarine18* range. For those dates we respectively applied a ΔR = 105 ± 24 (GS-02), as indicated by (Mangerud et al., 2006) and applied by (Caricchi et al., 2019), and ΔR = 1234 ± 106 for the CAGE-15 as indicated by (Skinner et al., 2017).

As multiple levels were age-dated on each sediment core, it became possible to build age-depth models along the studied intervals. That step of the study was conducted at the Downing College, University of Cambridge (United Kingdom). In order to achieve the most accurate models possible, Bayesian statistics has been applied, using the open software *Bacon v.2.3.9.1* (Blaauw and Christen, 2011), through R interface (R Development Core Team 2013). The program divides the core into virtual vertical sections of the same size and estimates the accumulation rates expressed in years/cm, running millions of Markov Chain Monte Carlo (MCMC) iterations for each section. This approach provides more realistic estimates for the accumulation rates because it considers changes within the sections, instead of assuming a constant sedimentation rate between tie points (linear interpolation). A 10 cm interval of vertical section was applied for the cores IRIDYA-02 and GS-02, while a 5 cm interval was possible for the core CAGE-15 due to the higher density of radiocarbon dated levels (representing the tie points) along the studied interval.

To consider the abrupt changes on the accumulation rates, boundaries have been applied to the models in correspondence of the onset of the Holocene period, the MWP-1A, the H1- and H2-like events (Fig. 1.3.1, 1.3.2 and 1.3.3). The accumulation mean rate for each interval in between boundaries was calculated using the difference in depth and median probability age obtained with the initial single calibration on *Oxcall*.

The MCMC log of interactions (which is visible on the age-model figures) should be random and result in a noisy signal without a clear trend, meaning that the model has considered as many different scenarios as possible, based on the given accumulation mean rate and shape. The default accumulation shape (acc.shape) value used by the software is 1.5, any higher value leads to a more peaked acc.shape curve meaning lower variance. The acc.shape values applied for each interval are also visible on the age-model figures, and were tested case-by-case.

To define how the accumulation rate of a particular depth depends on the accumulation of the depth above, the model applies a parameter called *memory* which is determined by the user selecting a value from 0 to 1.0. Low values of memory (<0.5) should be used when the accumulation shape is thought to have changed significantly over time due to intense variations on the environmental conditions that influence the accumulation rate, while higher values (>0.5) are suitable for study areas in which the accumulation rates are thought to have changed more gradually over time. In this study a value of 0.4 has been applied for the *memory*. The software Bacon *v.2.3.9.1* requires from the user the sedimentation rate expressed in years/cm, contrarily to the commonly used cm/years.

A tuned chronology was then built by staking GS-02 and IRIDYA-02 age dating results to the core CAGE-15 (Fig. 1.3.4). The stacked results were associated with the lithofacies transitions or the recurrent presence of oxidized layers, which are well correlated among the studied cores.

1.3 Results

In the following paragraph, the AMS ^{14}C dating results obtained from *N. pachyderma* tests picked from a total of 20 samples from the three cores are reported (Table 1.3.1), together with the age-depth models built for each core (Figs. 1.3.1, 1.3.2 and 1.3.3). Most of the age-dated levels were chosen precisely on lithofacies transitions, associated with the meltwater pulses, Heinrich-like events or the onset of the Holocene period. Additional samples were taken after the micropaleontological analyses were performed (Chapter 2 of this thesis).

Sample ID	Core	mbsf	^{14}C Age	Age Err	ΔR	1σ	2σ	Median probability	Data Source
OS-176482	*CAGE-15*	*2.47-2.50*	*12550*	*230*	*-162 ± 192*	*14146-13514*	*14605-13251*	***13804***	*This study*
OS-176492	*CAGE-15*	*3.34*	*13100*	*250*	*-234 ± 363*	*15148-13901*	*15756-13390*	***14518***	*This study*
OS-176483	*CAGE-15*	*3.53*	*14700*	*130*	*-978 ± 102*	*15965-15479*	*16206-15246*	***15724***	*This study*
OS-176493	*CAGE-15*	*3.78*	*16900*	*170*	*-1048 ± 155*	*18598-18075*	*18837-17780*	***18343***	*This study*
OS-176485	*CAGE-15*	*3.92*	*16950*	*150*	*-1055 ± 155*	*18621-18140*	*18846-17865*	***18384***	*This study*
OS-176486	*CAGE-15*	*4.35*	*19200*	*210*	*112 ± 105*	*22429-21889*	*22738-21546*	***22165***	*This study*
OS-176487	*CAGE-15*	*4.59*	*20900*	*360*	*781 ± 109*	*23704-22875*	*24178-22464*	***23287***	*This study*
OS-176488	*CAGE-15*	*4.91*	*21400*	*320*	*1125 ± 115*	*23821-23067*	*24271-22692*	***23445***	*This study*
OS-176494	*CAGE-15*	*4.96*	*21500*	*320*	*1244 ± 103*	*23809-23044*	*24260-22662*	***23426***	*This study*
OS-176495	*CAGE-15*	*5.16*	*24100*	*420*	*1241 ± 106*	*27778-26976*	*28331-26493*	***27372***	*This study*
OS-176489	*IRIDYA-02*	*1.62*	*10150*	*220*	*-316 ± 86*	*11550-10444*	*12147-9913*	***10978***	*This study*
OS-176490	*IRIDYA-02*	*3.82*	*15200*	*140*	*-1059 ± 75*	*16526-16020*	*16786-15765*	***16268***	*This study*
OS-176491	*IRIDYA-02*	*4.60*	*20300*	*570*	*-554 ± 109*	*23594-22300*	*24354-21640*	***22918***	*This Study*
OS-123787	*GS-02*	*0.26*	*3340*	*25*	*-105 ± 24*	*2961-2797*	*3051-2742*	***2876***	*Caricchi et al., (2019)*
OS-123531	*GS-02*	*0.75*	*8210*	*35*	*-105 ± 24*	*8485-8333*	*85618240*	***8404***	*Caricchi et al., (2019)*
OS-123792	*GS-02*	*1.72*	*9970*	*60*	*-165 ± 25*	*11039-10548*	*11234-10305*	***10798***	*Caricchi et al. (2019)*
OS-123415	*GS-02*	*2.02*	*10950*	*110*	*-195 ± 101*	*12395-11741*	*12621-11389*	***12084***	*Caricchi et al., (2019)*
OS-123532	*GS-02*	*5.67-5.69*	*16850*	*80*	*-1052 ± 162*	*18517-18060*	*18695-17823*	***18285***	*Caricchi et al., (2019)*
OS-123533	*GS-02*	*7.08-7.10*	*19950*	*110*	*343 ± 112*	*22882-22498*	*23072-22324*	***22697***	*Caricchi et al., (2019)*
OS-123534	*GS-02*	*8.24-8.26*	*21200*	*120*	*895 ± 111*	*23671-23237*	*23842-23038*	***23467***	*Caricchi et al., (2019)*

Table 1.3.1: AMS ^{14}C dating on Neogloboquadrina pachyderma. Process: Acidification (hydrolysis). The ΔR effect was calculated for each sample by the difference between the calibration curves Marine20 from (Heaton et al., 2020) and Normarine18 from (Brendryen et al., 2020). The median probability, Sigma 1 and 2 (1σ and 2σ) were obtained using the software Oxcal V4.4 (Ramsey, 2009).

1.3.1 CAGE-15

The CAGE-15 is the main core studied in the present thesis because it was designed for high-resolution micropaleontological analyses at 1-cm sampling spacing along the T1-LGM interval. Hence, a bigger number for age dating analysis was performed on this core (total of 10 dated intervals), resulting in a more detailed age-depth model defined through 55 vertical sections of 5-cm each (Fig.1.3.1).

Two major shifts on the Acc.rate were recognised respectively at the onset of the H2-like event and the MWP-1A, separating the core in three different intervals. The lower interval is located between 5.16 and 4.96 mbsf having a low sedimentation rate of ~200 years/cm, from during 27.37 to 23.42 ky cal BP. This older interval was followed by an interval of 2.66 cm having an average Acc.rate of 55 years/cm, until the onset of the MWP-1A at 3.34 mbsf with an age of 14.52 Cal ky BP, when the rate abruptly rises to 8 years/cm (Fig.1.3.1A).

The log of iterations shows a very consistent noisy signal (Fig.1.3.1B), indicating that the model was able to test thousands of random scenarios for each 5-cm-large vertical section of the core. The Acc.rates followed the given means but within the cloud points there are testing of values varying from 0 to 600 years/cm (Fig.1.3.1C) and the relatively low *memory* (Fig.1.3.1D) shows that the sedimentation rate of a specific section may be very discrepant to the previous section, which is normally expected in a highly dynamic environment.

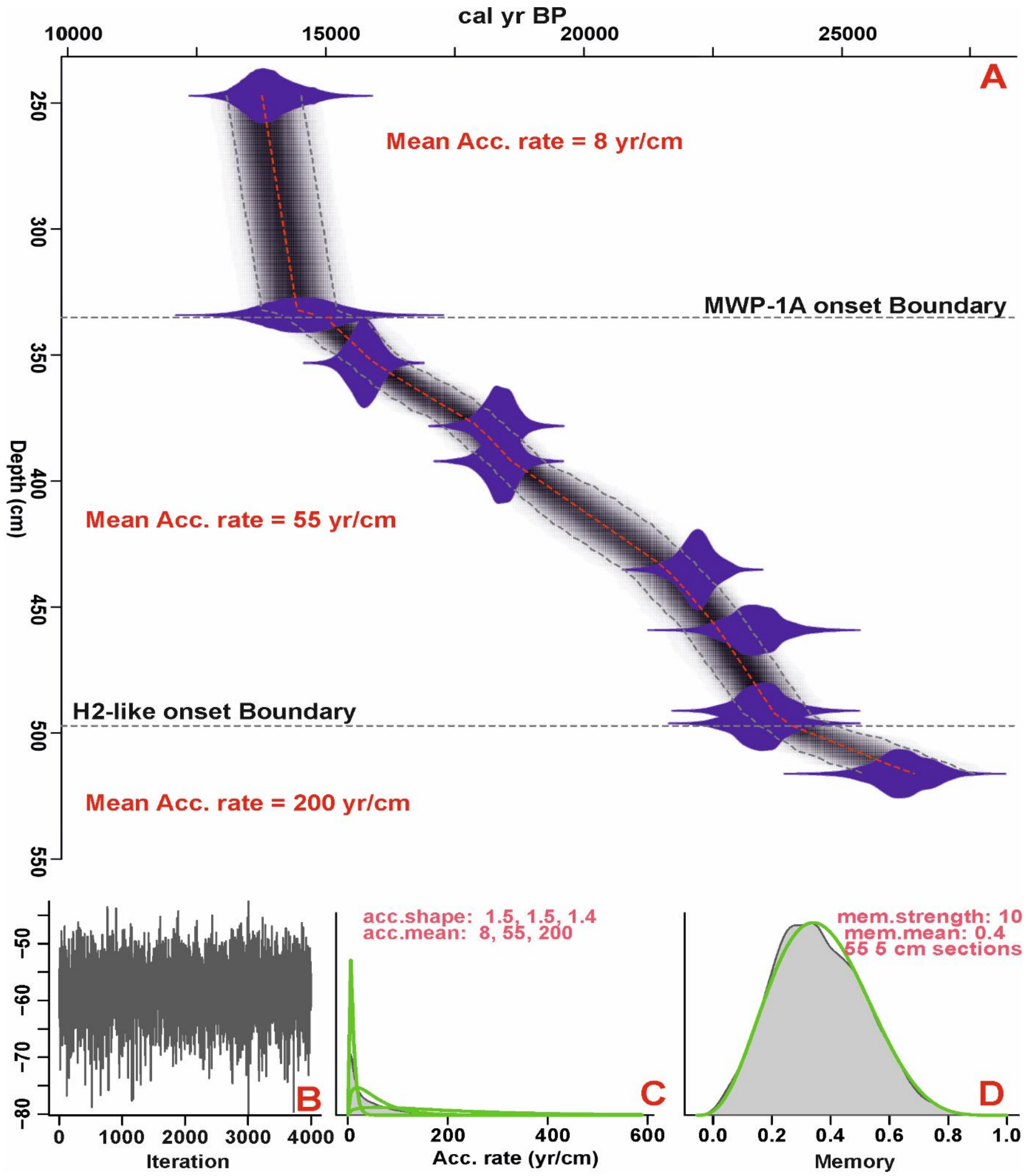

Figure 1.3.1: A) Bayesian age-depth model for the core CAGE-15, applying 55 vertical sections of 5 cm. The boundaries at the onsets of the H2-like and the MWP-1A events separates the core in three intervals with mean accumulation rates of 8, 55 and 200 yr/cm. B) Log of Markov Chain Monte Carlo (MCMC) Iterations. B) Accumulation mean (acc.mean) and accumulation shape (acc.shape). C) Memory.

1.3.2 IRIDYA-02

Three levels were selected for age dating on this core aiming to simply improve core-to-core correlation. The small number of radiocarbon dates limited the resolution of the age model method applied for this core (Fig.1.3.2). However, the dated levels revealed the presence of the H2-like event and allowed us to refine the location of the H1-like event and the base of the Holocene period. Due to differences in the Acc.mean, a boundary was applied in the intermediate dated level (at 3.82 mbsf or 16.26 Cal Ky BP, Table 1.3.1), separating the model in two main intervals with specific average Acc.rates of 85 and 24 year/cm (Fig.1.3.2A).

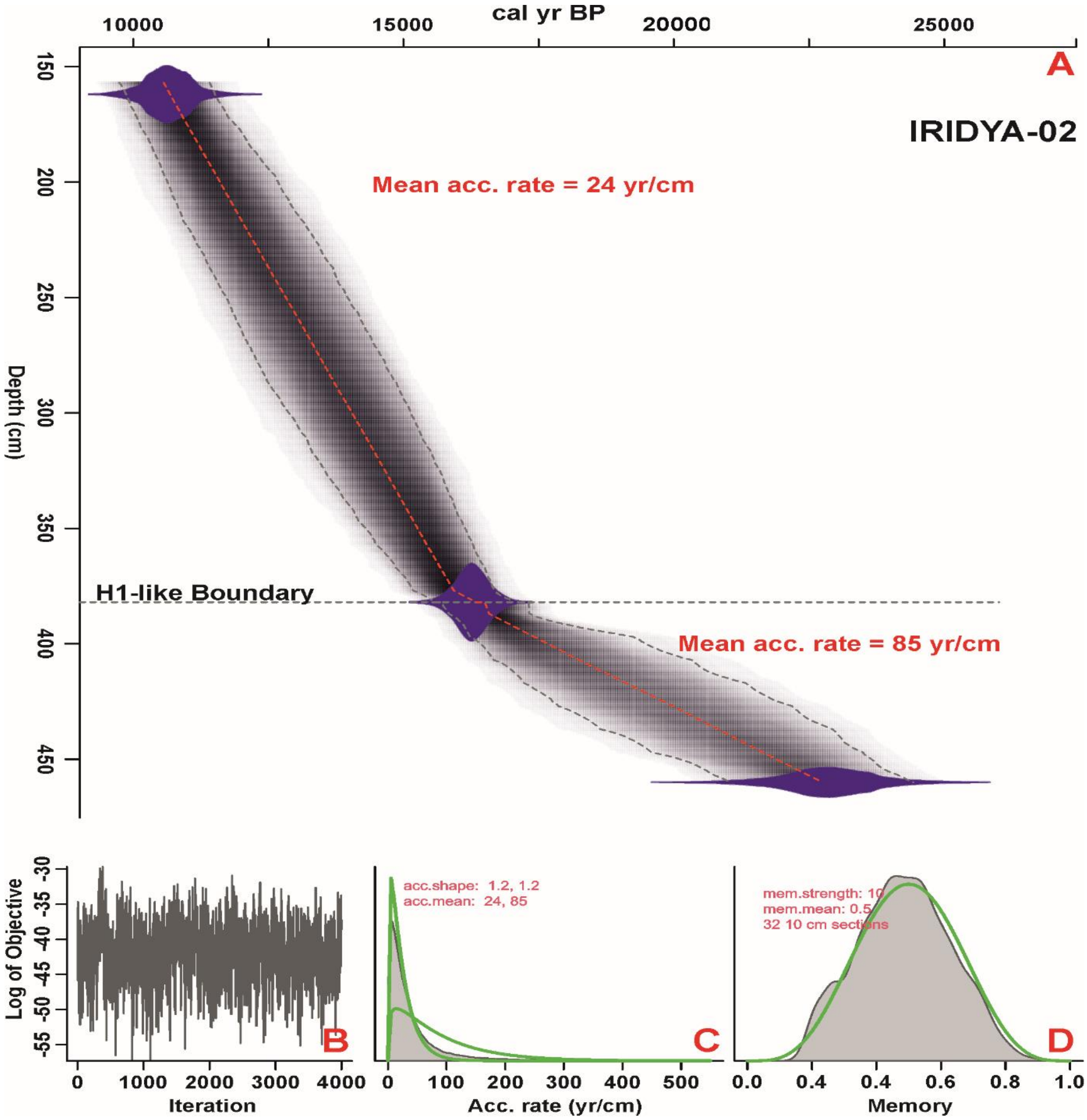

Figure 1.3.2: A) Bayesian age-depth model for the core IRIDYA-02, applying 32 vertical sections of 10 cm. The boundary at the onsets of the H1-like event separates the core in two intervals with mean accumulation rates of 24 and 85 yr/cm. B) Log of MCMC Iterations. B) Acc.mean and Acc.shape. C) Memory.

The log of iterations shows a noisy signal (Fig.1.3.2B), indicating that the model was able to test thousands of random scenarios for each 10 cm vertical section of the core. The Acc.rates followed the given means but within the cloud points there are testing of values varying from 0 to 550 years/cm (Fig.1.3.2C) and the intermediate value of memory (Fig.1.3.2D) shows that the sedimentation rate of a specific section may be not very similar to the previous section, which was expected due to the abrupt changes in sedimentations rates related to Meltwater pulses and Heinrich-like events.

1.3.3 GS-02

The GS-02 is the one that had been age-dated previously (Caricchi et al., 2019), but only the raw data from that study was used here. Furthermore, this is the only core with age-dated levels within the Holocene interval and has the most expanded sedimentary section of the study. The model splitted the studied interval in 81 vertical sections of 10 cm each. Due to shifts in the Acc.mean, boundaries were applied at 7.20 and 1.52 mbsf, in correspondence to the termination of the H2-like event, and at the Holocene inception, respectively. Hence the model was separated in three intervals with specific average Acc.rates of 7, 22 and 113 years/cm (Fig.1.3.2A).

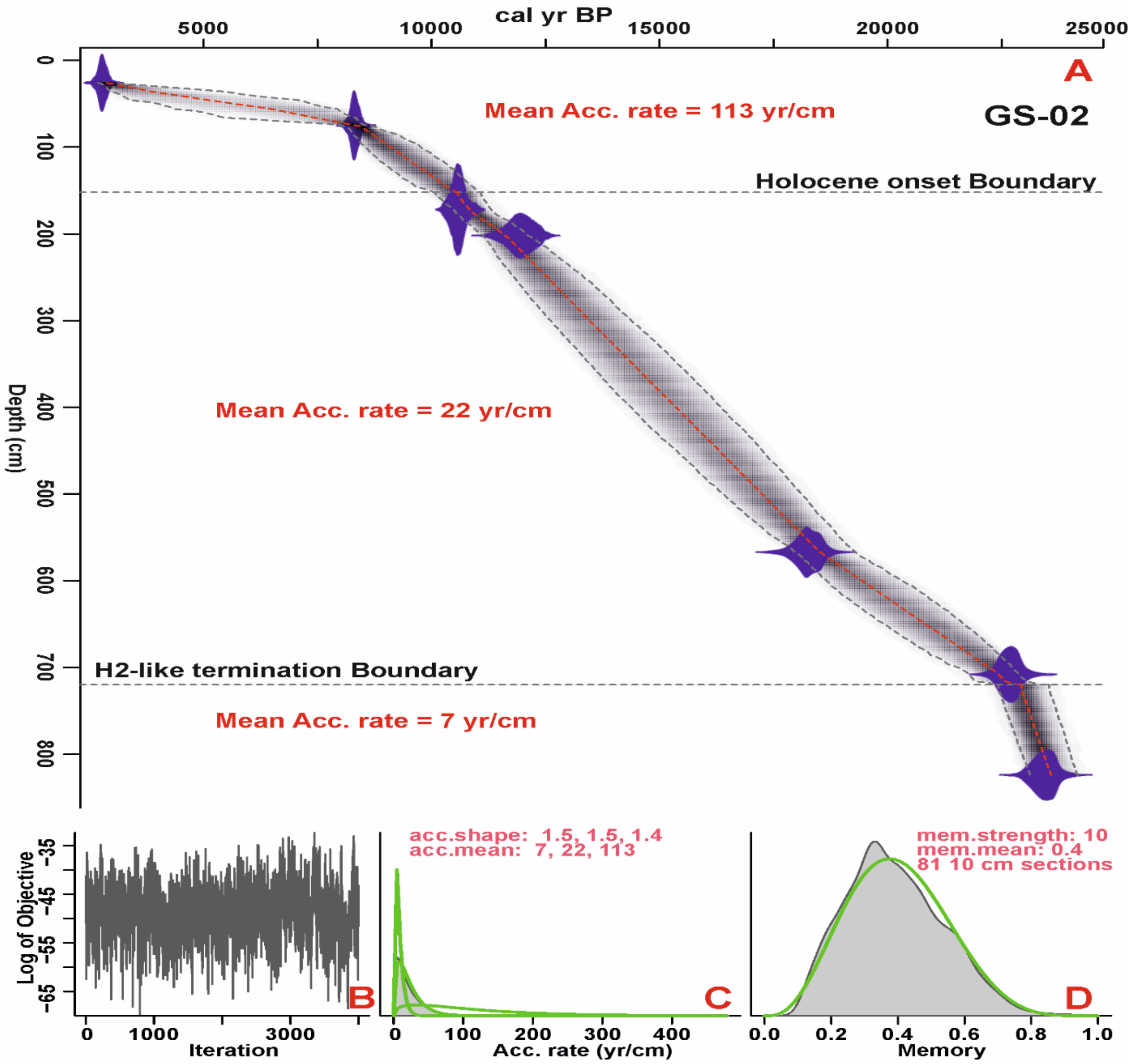

Figure 1.3.3: A) Bayesian age-depth model for the core GS-02, applying 81 vertical sections of 10 cm. The boundaries at the H2-like termination and the onset of the Holocene period separates the core in three intervals with mean accumulation rates of 7, 22 and 113 yr/cm. B) Log of MCMC Iterations. B) Accumulation mean (acc.mean) and accumulation shape (acc.shape). C) Memory.

The log of iterations shows a noisy signal (Fig.1.3.2B), indicating that the model was able to test thousands of random possibilities for each 10 cm vertical section. The Acc.rates followed the given means but within the cloud points included scenarios with values between 0 and 500 years/cm (Fig.1.3.3C), while the memory shows a relatively low value (Fig.1.3.2D), indicating that the sedimentation rate of a specific section can be considerably different from the previous section due changes in sedimentation rates caused by the Meltwater pulses and Heinrich-like events.

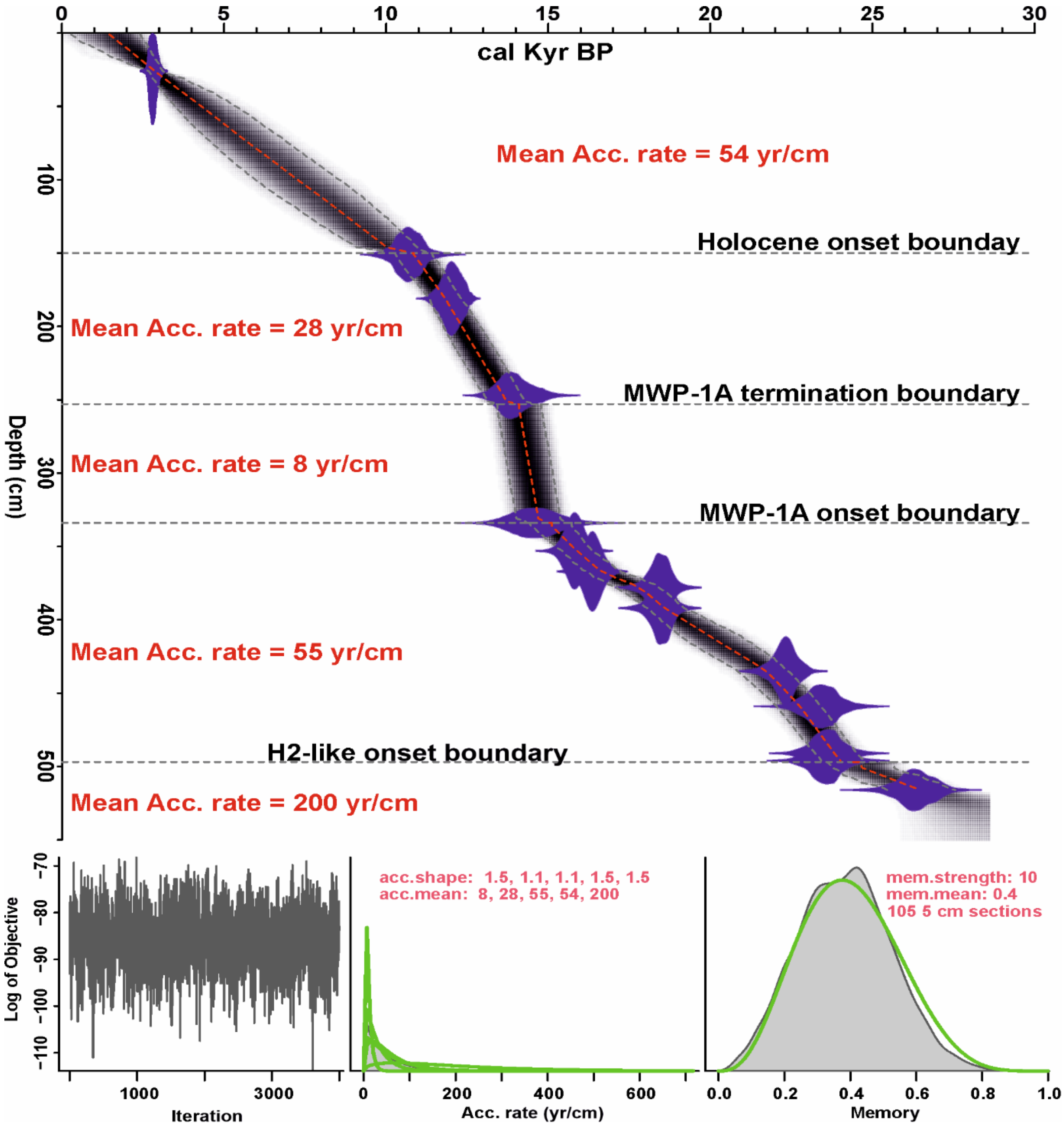

Figure 1.3.4: A) Tuned Bayesian age-depth model stacking to the CAGE-15, one age dating result from IRIDYA-02 core (162 cm) and two other results from GS-02 core (202 and 26 cm). Applying 105 vertical sections of 5 cm. The boundary at the onset of the H2-like event, MWP-1A (onset and termination), and the Holocene period, separates the core in five intervals with mean accumulation rates of 54, 34, 18, 55 and 200 yr/cm. B) Log of MCMC Iterations. B) Acc.mean and acc.shape). C) Memory.

1.3.4 Discussions

The radiocarbon age-dating results presented here precisely identified when the major climate events associated with the last glacial and glacial termination occurred in the studied area. The onset and termination of two H-like events (H2 and H1), and two MWPs (the MWP-1A$_0$ and MWP-1A) were determined and their impacts on the local marine ΔR was considered. From the core CAGE-15 it was possible to achieve a considerably high-resolution model, due to the high-density of age-dated levels with 10 within 11 cal ky, whilst from the cores IRIDYA-02 and GS-02 it was possible to tune the CAGE-15 age-model, making a composed chronology covering the last 28 cal ky BP.

Comparing the results presented in this work for the core GS-02, with the previous results published by (Caricchi et al., 2019), significant time differences were found regarding the timing of the MWP-1A$_0$ and the H2-like events. Here, those events are respectively ~1500 and ~1700 years younger. As the same raw radiocarbon dates were used for both works, the large differences in age estimation were essentially caused by the different calibration methods applied.

The differences between the use of the *Marine13* in (Caricchi et al., 2019 and the *Marine20* used in this thesis, must have contributed to shape the discrepancy described, although the main reason for such discrepancy rely on the determination of the ΔR. The previous study applied a constant value of 105 ± 24 obtained through the *Calib* 7.1 software, which is adequate for the Holocene period, but that is not the case for the glacial termination T1 or the LGM, due to the extremely different environmental conditions related of ocean circulation, deep-water formation, and extreme events of melting such as the meltwater pulses. In this work, the calculated ΔR were -1052 ± 162 for the onset of the MWP-1A$_0$, and 895 ± 111 for the onset of the H2-like event.

However, until 2020 this age-depth model method was not available because the only calibration curve available for the study area was the *Marine13*, hence calculating a variable ΔR for multiple samples was impossible. Actually, the particularities of the ΔR behaviour in the study area during that time period were the motivations for the development of the *Normarine18* curve which allowed to refine the ages in the sub-Arctic area including the calibration performed in this work.

Chapter 2 - Paleoclimatic-paleoceanographic multiproxy reconstruction of the last 28 thousand years at West Margin of Svalbard.

2.1 - Introduction

The oceanic thermohaline circulation is the main driver for heat transport from low to high latitudes, directly affecting the global climate (Hansen et al., 2004; Kuhlbrodt et al., 2007; Meland et al., 2008; Rahmstorf et al., 2015; Knies et al., 2018). In the Northern Hemisphere, the North Atlantic Meridional Overturning Circulation (AMOC) plays that fundamental role by carrying Equatorial warm surface waters that follow a clockwise gyre that follow the South, Central and North America East coasts, passing through the Caribbean Sea, before crossing the ocean towards the Northeast until reach the Greenland-Iceland-Norway (GIN) Seas, and became the West-Spitsbergen current (WSC), before passing through the Fram Strait, the only deep-water gateway between the Arctic and North Atlantic oceans (Aagaard and Carmack, 1989; Klenke and Schenke, 2002; Meland et al., 2008; Hansen et al., 2022) (Fig.2.1.1). Therefore, the Northern Hemisphere climate is highly sensitive to that overflow of and compensating southward flow of cold deep water through the Fram Strait and the Greenland–Iceland–Scotland Ridge (Aagaard and Coachman, 1968; Crocket et al., 2011; Müller and Stein, 2014). The variability in the WSC strength towards the Arctic plays an important role in climatic conditions and significant variations over time have been described (Rahmstorf, 2002; Rasmussen et al., 2007; Ślubowska-Woldengen et al., 2008; Risebrobakken et al., 2011; Kristensen et al., 2013; Werner et al., 2013; Rasmussen et al., 2014; Melis et al., 2018). Also, Physical models suggest that, in the absence of such circulation, heat transport to the Northern Hemisphere can be reduced by 50% and in the open North Atlantic sea-ice limit can migrate southward (Crocket et al., 2011).

Early reconstructions of the LGM oceanographic conditions using oxygen isotopes of benthic foraminifera indicated that the hydrological structure and the circulation of the deep ocean were completely different from the present one (Labeyrie et al., 1992) with colder deep-waters (by 2-4ºC), permanent sea-ice cover in the GIN Seas, weaker northward transport of warm salty water, and deep-water convection restricted to the open North Atlantic in the area south of the Greenland-Iceland-Scotland Ridge (Duplessy et al., 1980; Labeyrie et al., 1987; Duplessy et al., 1988; Labeyrie et al., 1992).

More recent studies indicate the presence of at least seasonally ice-free open water in the GIN Seas with intermittent northward flow of the North Atlantic Current (Rasmussen and Thomsen, 2008). Furthermore, evidences from bottom-water Neodymium (Nd) isotope indicated an intermittently of the southward flow from the Norwegian Sea Deep Waters into the North Atlantic during the LGM, confirming that GIN Seas remained a source of deep water, contrary to the earlier idea of a stagnant glaciated GIN Seas (Meland et al., 2008; Müller et al., 2009; Crocket et al., 2011; Müller and Stein, 2014; Caricchi et al., 2019).

During glacial terminations, that oceanic mechanism can increase the amount of heat delivered to the polar ice shelves that can become unstable. However, it is a sensitive mechanism to meltwater releases that create ocean stratification and interrupt dense water formation, an important branch of the thermohaline circulation itself. Therefore, the relationship between ocean and ice-sheet dynamics can cause non-linear abrupt climate shifts.

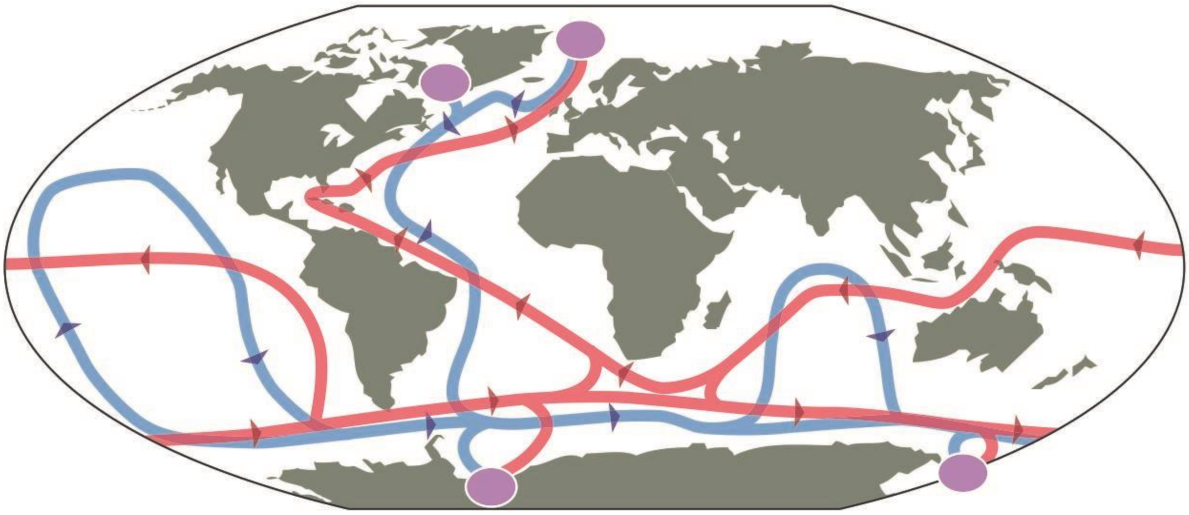

Figure 2.1.1 Illustration of the Ocean Thermohaline circulation, from (Hansen et al., 2004). Red and blue arrows indicate warm and cold currents, respectively. Purple circles indicate the areas where deep-water formation occurs.

In this chapter, a detailed reconstruction of the paleoclimatic, paleoceanographic conditions of the West continental margin of Svalbard is presented using 3 marine sediment cores collected along the study area (Fig. 2.1.2). A multi-proxy approach was applied, including sedimentological description, compositional analyses, stable isotopes ($\delta^{18}O$) measurements on planktonic foraminiferal shells. Also, for the core CAGE19-3KH-15GPC, the analyses were conducted continuously at the high-resolution (1-cm), within the LGM-T1 interval of the expanded depositional sequences associated with the depocenters of the Bellsund and Isfjorden sediment drifts (Rebesco et al., 2013).

Two MWPs and two Heinrich-like events were recognized in the cores, and the chronology explained in the previous chapter of this thesis was used to understand those sedimentary records and the proxy-results in time scale. Hence, the $\delta^{18}O$ variations, and depositional fluxes of Ice-Rafted Debris (IRD) and planktonic foraminifera (PF) calculated over time revealed new evidence of the interaction between ocean circulation, cryosphere and extreme episodes of melting and/or iceberg release in the Arctic during the SBSIS final complete melting.

Periods of high primary productivity during the glacial stage MIS-2, that can only be supported under sea-ice free conditions, pointed to the presence of large polynyas where dense water formation took place (Muller and Stain, 2014; Knies et al., 2018), thereby feeding the thermohaline circulation. However, those periods were followed by the MWP and Heinrich events that delivered large amounts of terrigenous sediments to the slope area of this margin (Lucchi et al., 2013; 2015). Such massive increases in sedimentation rates led to the deposition of intervals of barren sediments found on the cores, while the freshwater releases caused abrupt changes on the oceanographic conditions due to ocean stratification interfering with thermohaline circulation. Therefore, the results presented here point to clear evidence of the trigger mechanisms and onset dynamics interaction and mutual feedback. Also, showing a good agreement with the millennial scale Greenland stadial-interstadial cycle during this time period.

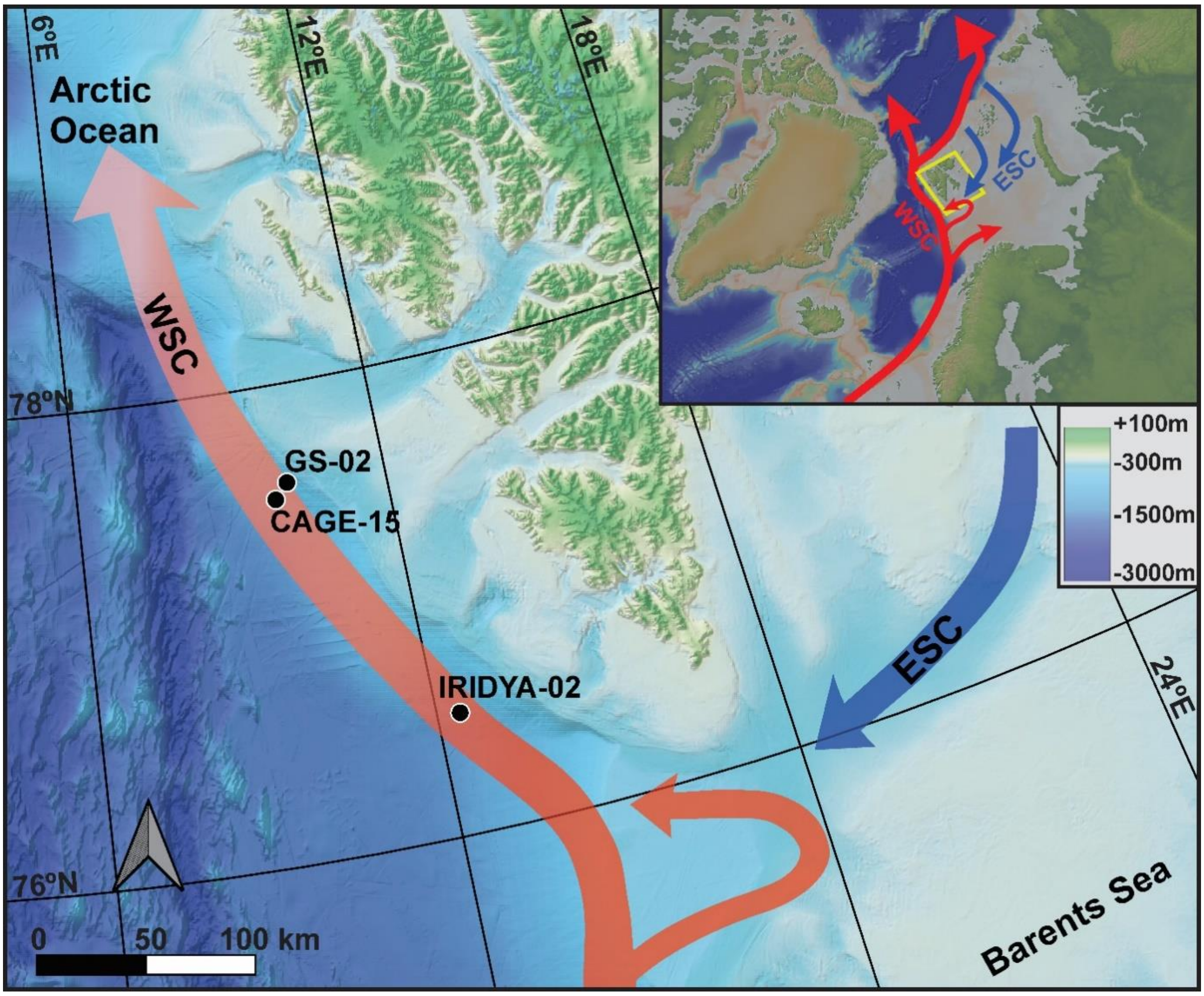

Figure 2.1.2: Study area location map. Black dots indicate the sites of IRIDYA-LB21-02PC (IRIDYA-02), CAGE-19-3KH-15GPC (CAGE-15) and GS191-02PC (GS-02) cores. Red arrow: West Spitsbergen Current (WSC). Blue arrow: East Spitsbergen Current (ESC). Bathymetric data from (Jakobsson et al., 2020). Produced using QGIS (QGIS Development Team, 2009).

2.2 Materials and Methods

This study considered the geological record recovered by three piston cores: the Calypso piston cores GS191-01PC and GS191-02PC (hereafter respectively named GS-01 and GS-02) collected in the framework of the project Eurofleets2-PREPARED, on board the RV G.O. Sars (Lucchi et al., 2014), the Calypso piston core CAGE19-3KH-15GPC (hereafter named CAGE-15) collected during the CAGE-2019 cruise on board the RV Kronprins Haakon (Knies and Vadakkepliyambatta, 2019), and the piston core IRIDYA-LB21-02PC (hereafter named IRIDYA-02) collected within the project PRA-IRIDYA on board the RV Laura Bassi (Lucchi et al., 2021).

These sediment cores were collected along the middle slope of the Southwest margin of Svalbard archipelago, between 1322 m and 1725 m water depth (Table 1), on sites specifically selected to reach a continuous and expanded depositional sequence that were identified with the acoustic survey of the sub-bottom profiles of the area. As this study focused on the LGM and T1 time interval, it was not necessary to use the entire length of the cores CAGE-15 and GS-02, once they reached older records. Therefore, specific study intervals were determined for those cores (Table 2.2.1).

Core ID	Water depth (m)	Core length (m)	Studied interval (m)	Latitude (N)	Longitude (E)
GS191-02PC (GS-02)	1322	17.36	0 - 8.50	77°35'21.01"	10°5'29.72"
CAGE19-3KH-15GPC (CAGE-15)	1579	15.73	0 - 6.00	77°31'34.68"	9°49'18.11"
IRIDYA-LB21-02PC (IRIDYA-02)	1725	4.87	0 - 4.87	76°31'44.4"	12°33'7.2"

Table 2.2.1: Core ID, water depth, core length and location.

2.2.1 – Core scan analyses and visual core-log description

Before opening the cores, physical properties of the sediments were analysed with core-scan techniques using a Geotech Multi Sensor Core Logger (MSCL) and a X-ray CT scan from OGS for the cores CAGE-15 and IRIDYA-02. The core GS-02 was scanned using a MSCL at the University and CSIC of Barcelona, X-ray CT scan from ENI-Italy. The radiograph images were set with the white indicating high-density or coarse-grained sediments, and the dark grey to indicate the low density or fine-grained sediments. After the opening, the cores were visually described, digitally photographed, and analysed for X-ray fluorescence (XRF) spectrometry.

The visual description of the sediments was performed on the archive-half section of the cores and considered: the sediment colour defined using the Munsell Soil Colour Chart (Munsell Color. 2009), the sedimentary structures (e.g. laminations, bioturbation, etc.), unit boundaries (sharp, gradual), granulometric changes, presence of IRD and their distribution (sparse, massive, layered), and presence of oxidized intervals. The cores CAGE-15, GS-01 and GS-02 were already described by previous studies (e.g. Caricchi et al., 2019; Douss, 2023), while the core IRIDYA-02 was described during this study.

2.2.2 – X-ray fluorescence spectrometry

The principle of the XRF analyses has been widely discussed by (Jenkins and Vries, 1970) (Jansen et al., 1998; Dypvik and Harris, 2001; Chen et al., 2006; Thomson et al., 2006), and (Croudace et al., 2019). The XRF core scanners consist of an X-ray source and a detector. The X-ray source emits X-rays which interact with the sample (surface of the sediment core). When the X-rays hit the sample, they cause the atoms in the sample to emit secondary X-rays that are characteristic for each element present. These secondary X-rays are then detected by the detector and measured. A software coupled with the instrument allows the processing of the raw XRF data that includes the instrument calibration, the correction of the background noise, and the conversion of the X-ray intensities into elemental concentrations. The XRF scanning has become a standard tool to understand the element composition of sediments allowing for fast, high-resolution analyses (down to sub-millimetric resolution), that are widely used in paleoenvironmental (Kern et al., 2019) and paleoclimate studies (Croudace et al., 2019).

In this doctoral project, the automated Avaatech XRF-core scan was used working at 10 and 30 Kv settings for light- and medium-weight chemical elements including: calcium (Ca), titanium (Ti), zirconium (Zr), rubidium (Rb), bromine (Br). The elements were plotted as ration following the known element proxies commonly used for paleoceanographic studies:

- The Zr/Rb ratio is a proxy for sediment grain size variations of marine sediments (Dypvik and Harris, 2001; Chen et al., 2006; Wu et al., 2020). The Zr is commonly found in sand-sized sediments, whilst the Rb is commonly forming clay minerals.

- The variations in Ca/Ti are commonly associated with the biogenic $CaCO_3$ contents, reflecting the varying proportions of marine biogenic carbonate (Ca) and terrigenous sediment (Ti) (Hodell et al., 2013; Mesa-Fernández et al., 2022).

- The Br/Ti ration on sediment cores is commonly used as a proxy for ocean surface productivity (Agnihotri et al., 2008; Fagel et al., 2024).

2.2.3 – Total and organic carbon and total nitrogen (CHN) analysis

The total and organic carbon (Ctot and Corg), total nitrogen (Ntot) were measured on discrete sub-samples collected at every 20 cm along all the cores (total of 205 samples). The samples were freeze-dried, ground in a ceramic mortar and sieved on a 250 µm sieve. For each sample, 8-12 mg of sediment was weighed on a micro ultra balance with an accuracy of 0.1 µg, directly into silver (for Corg) or tin (for Ctot and

Ntot) capsules. Carbon and nitrogen content was determined using a CHNO-S elemental analyser (model ECS 4010, Costech, Italy) at OGS-BIO according to (Pella and Colombo, 1973).

Before the Ctot determination, subsamples were treated directly in the capsules with increasing concentrations of HCl (0.1N and 1N) to remove the carbonate fraction (Nieuwenhuize et al, 1994). Standard Acetanilide (Costech, purity ≥ 99.5%) was used to calibrate the instrument, and empty capsules were also analysed to correct for blank. Carbon and nitrogen sample concentrations are expressed as percentages. Quality control of measurements was performed using internal standards and additionally verified for carbon against the certified marine sediment reference material PACS-2 (National Research Council Canada).

The Ntot/Corg ratio was used to depict the origin of the organic matter, considering a marine origin for ratio values below 10 and continental origin for ratios higher than 10 according to Meyers (1994). The calcium carbonate ($CaCO_3$) and the organic matter (OM) were then determined through calculation as: OM = Corg x 1.8 (Gordon, 1970), $CaCO_3$ = Cinorg x 8.33 (molar ratio). Where Cinorg = Ctot – Corg.

2.2.4 – Micropaleontological analyses

The micropaleontological investigation played a fundamental role in this study providing monospecific foraminiferal tests of *Neogloboquadrina pachyderma* for the radiocarbon dating as explained in the previous chapter, and for the oxygen stable isotopes analyses and clumped elements that are discussed in this chapter. The sinistral (left-cooling morphotype) was used because it was much more abundant than the dextral form. In addition, some cores levels had very little foraminiferal content (e.g. in the MWP and H-like events intervals).

Individual sub-samples for qualitative micropaleontological analyses were collected every 5-10 cm, on the cores CAGE-15 and IRIDYA-02, totalizing 57 and 59, respectively. As the core GS-02 had been studied in a previous investigation (Caricchi et al., 2019), only 7 additional samples were used for that core. Furthermore, to obtain a high-resolution understanding of the LGM and T1 periods, additional 234 samples were continually taken at every 1 cm for quantitative analyses along the interval containing the deposits associated with the H2, MWP-19 and MWP-1A events, between 2.39-2.60 and 3.19-5.24 mbsf (metres below the seabed) of the core CAGE-15. Although, the 1cm resolution sampling was not performed between 2.60 and 3.19 cm because this interval is inside the MWP-1A deposits where the number of foraminifera is very close to zero which makes analysis unfeasible. Hence, during this study, a total number of 357 samples were qualitatively analysed for microfossils, 234 of which were quantitatively analysed.

Initially, all samples were wet sieved at 63 µm using distilled water only. Then, they were dried at 40ºC, for 24 hours for the sandy fraction (> 63 µm), and 7 days for the muddy fraction (<63 μm). Both fractions were weighed separately with a precision balance. The fine fraction was achieved in the laboratory, remaining available for future analysis (e.g. clay mineral assemblage) and the coarse fraction was analysed using a binocular microscope with up to 32x magnification.

Since it is very likely that broken shells were transported by bottom currents, only intact (well-preserved) planktonic individuals were considered as *in-situ* material and were counted using the microscope. Sediment splitting was necessary to sub-sample the sandy residues containing a high foraminifera concentration. In some cases, only 1/32 of the sandy fraction was used, and yet numbers over 1000 planktonic foraminifera were reached. Also at this step, the Ice-rafted debris (IRD) present on the samples also were counted, but using the fraction >500 μm, to exclude the possible influence of bottom current transport.

The concentration of Planktic Foraminifera (PF) and IRD grains present in the sediments were described as units/grams (PF/g sed and IRD/g sed). Both were used along with the mass accumulation rate of the sediments (g/cm²/year), obtained from the age-depth model (described on the Chapter 1) to calculate the depositional fluxes of PF and IRD (hereafter called PF flux and IRD flux) along the core CAGE-15, following the equation: Flux (PF/cm²/year) = PF/g sed · Mass accumulation rate.

As the majority of benthic foraminifera specimens were not well preserved or reworked (possibly relocated), a precise quantification would require a significantly time-consuming separation between intact and reworked individuals. Therefore, the benthic content was described only qualitatively.

2.2.5 – Oxygen stable isotopes

Stable isotopes ($\delta^{18}O$ and $\delta^{13}C$) were measured on the PF *Neogloboquadrina pachyderma* at a sample spacing of 1 cm between 2.39 and 5.24 mbsf. An average of 40-60 specimens were picked from the >150 μm size fraction and were used for analysis in order to reduce statistical variability, except in the few samples that contained fewer than this number. Very few samples, between 4.68 and 4.87 mbsf, did not provide enough specimens for the isotopic analyses and, in this interval, individuals picked from two adjacent samples were grouped together for analysis. Between 2.59 and 3.18 mbsf, specimens of *N. pachyderma* were either absent or too scarce to provide a sufficient quantity of carbon dioxide for a reliable measurement. Hence, a total of 224 measurements were performed along the core CAGE-15.

This particular analysis was carried out by the professor Patrizia Ferretti (UNIVE) at the Godwin Laboratory for Paleoclimate Research at the Department of Earth Sciences, University of Cambridge (United Kingdom) on a Thermo MAT253 IRMS coupled to a Kiel IV carbonate preparation device. Measurements of $\delta^{18}O$ and $\delta^{13}C$ were determined relative to the Vienna Peedee Belemnite (VPDB) standard, and the analytical precision was better than 0.08‰ for $\delta^{18}O$ and 0.06‰ for $\delta^{13}C$.

2.2.6 – *Mg/Ca measurements*

Unlike the previous analyses, sub-sampling for Mg/Ca was not performed continuously along the LGM/T1 interval of the core CAGE-15. Instead, specific levels (Table 2.3.2) associated with peaks on the FP flux and/or $\delta^{18}O$ curves have been selected (Fig 2.3.5). The Mg/Ca ratio was measured on the planktic foraminifera tests of *N. pachyderma* (212-300 µm) of 7 samples and the sea-surface temperatures were estimated following the (Kozdon et al., 2009) calibration. Clumped elements such as Al, Fe, Sr, Li, Br and B were also measured.

An average of 45 individual foraminifera were gently crushed between two glass plates to open the chambers and aid the removal of contaminants during the cleaning process. The foraminiferal samples were cleaned using the modified full reductive and oxidative cleaning procedure (Rosenthal et al., 1997) and analysed for Mg/Ca using the Thermo Element ICP-MS-XR at Rutgers University following the method of (Rosenthal et al., 1999). Repeated analysis of a laboratory internal consistency standard (Mg/Ca = 3.3 mmol/mol) indicates that the precision of the instrument for this run was <1.5%. Contaminant ratios of Al/Ca and Fe/Ca were < 45 µmol/mol for both ratios except for the youngest sample showing Fe/Ca = 300 µmol/mol (Table 2.3.2) and therefore none of the samples were discarded.

2.2.7 – Calcareous nannofossils

Calcareous nannofossils were studied from 23 selected samples of CAGE-15 sediment core. Samples for the nannofossil quantitative analysis were prepared using the filtering method (Okada, 2000) and were analysed with a light-polarised microscope at X1250 magnification. The specimens were counted in 314 fields of view, corresponding to an area of 6.28 mm^2 following the method described by Backman and Shackleton (1983) and Rio et al. (1990).

The absolute abundance (number of specimens per gram of sediment; n/g), was calculated. The identification of calcareous nannofossil species follows the taxonomic identification of (Young et al., 2003) and (Jordan et al, 2004). However, for the purpose of this study, the specific differentiation of coccolithophores will not be discussed. The in-situ specimens are expressed as Total Coccoliths, and their abundances were interpreted as an indicator of coccolithophore productivity. The abundance of reworked nannofossils (taxa of older stratigraphic levels, e.g. Paleogene and Cretaceous) was calculated against in situ species. The reworked abundance was used to confirm the pristine deposition of in situ species as their abundances are often used to investigate the continental input at the study site (e.g. (Ferreira, Cachão and González, 2008; Carbonara et al., 2016).

2.3 – Results

2.3.1 Sediment lithofacies

Along the studied interval of the sediment cores (Table 1) three main lithofacies were recognized through visual core description, radiograph images, digital photographs, composition and X-ray fluorescence spectrometry: a) Bioturbated IRD rich; b) Interlaminated sediments; c) Heavily bioturbated. The stratigraphic sequence recovered is highly similar among all the cores. From the bottom of the studied intervals until approximately 1.50 metres below sea floor (mbsf), there is a clear alternation between two different sedimentary facies, the Bioturbated IRD rich and the Interlaminated sediments. Above that alternation, on the interval between 1.50 and the core tops (sea floor surface), only the heavily bioturbated facies are recognized in the cores. Furthermore, four oxidised layers were recognized at specific intervals, being very useful for core-to-core correlation.

In the following, it is reported a detailed description of the lithofacies and oxidised layers defined. The characteristics of the sediments are summarised in Table 2.3.1 and Figs. 2.3.1, 2.3.2 and 2.3.3.

Lithofacies	Intervals (GS-02) (mbsf)	Intervals (CAGE-15) (mbsf)	Intervals (IRIDYA-02) (mbsf)
Heavily bioturbated	0 - 1.50	0 - 1.51	0 - 1.60
Bioturbated IRD rich	1.50 - 2.84 3.96 - 4.70 5.64 - 7.20 8.15 - 8.50	1.51 - 2.53 3.34 - 3.77 3.87 - 4.61 4.90 - 6.00	1.60 - 2.92 3.45 - 3.98 4.03 - 4.61
Interlaminated sediments	2.84 - 3.96 4.70 - 5.64 7.20 - 8.15	2.53 - 3.34 3.77 - 3.87 4.61 - 4.90	2.92 - 3.45 3.98 - 4.03 4.61 - 4.87
Ox-0	0 - 0.10	Not recovered	Not recovered
Ox-1	1.96 - 2.01	1.78 - 182	2.15 - 2.20
Ox-2	4.28 - 4.35	3.60 - 3.67	3.83 - 3.89
Ox-3	8.29 - 8.31	5.21 - 5.23	Not recovered

Table 2.3.1: Occurrence depths of the lithofacies on the cores in metres below sea floor (mbsf).

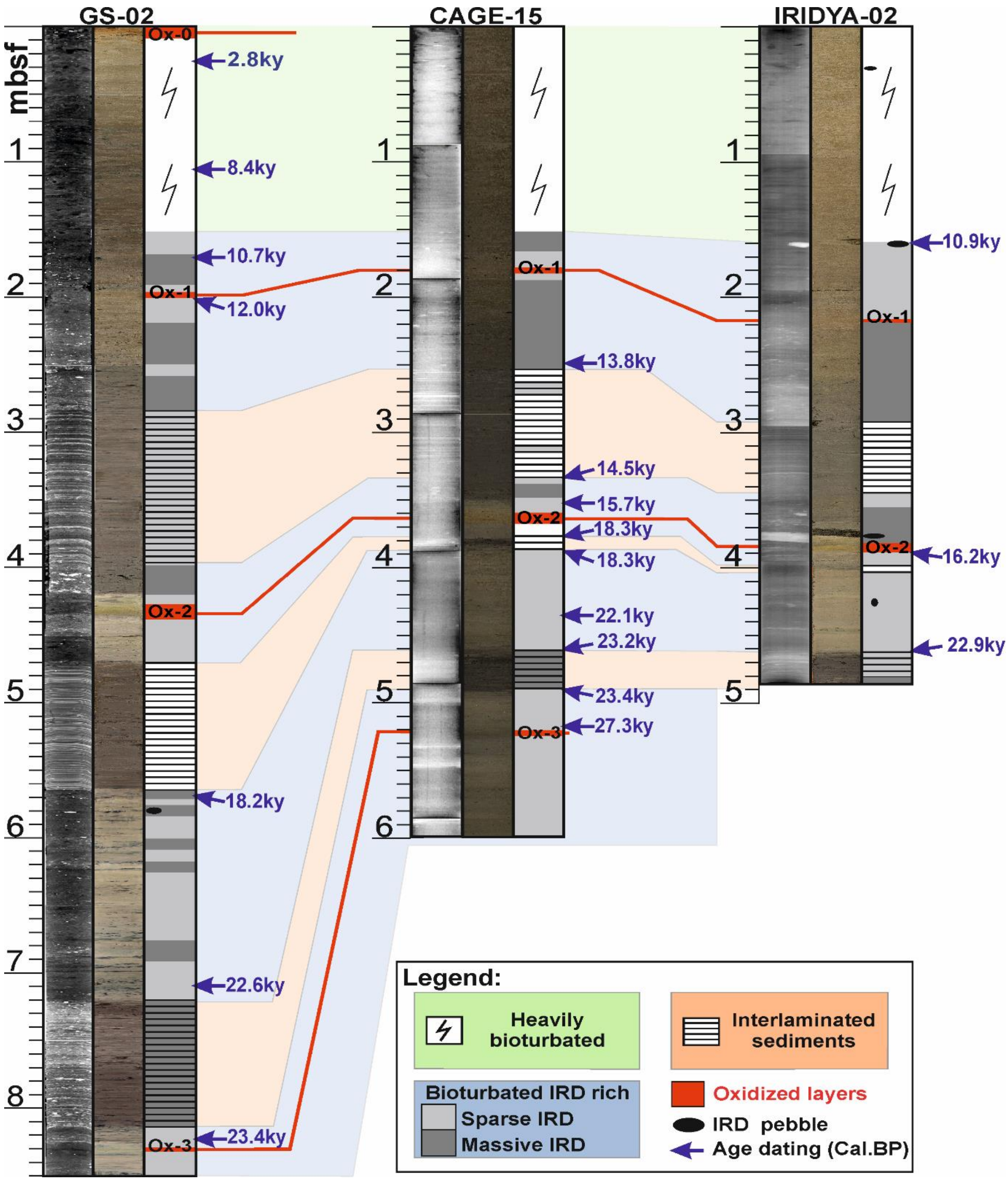

Figure 2.3.1: Stratigraphic correlation and lithofacies recognized along the studied interval of the cores using radiograph images, digital photographs and core log description of the studied intervals. Shaded areas indicate the three lithofacies: in pink the interlaminated sediments, in light blue the bioturbated IRD rich sediment and in green the heavily bioturbated sediments.

2.3.1 – Bioturbated IRD rich sediments

This lithofacies consists of sparsely bioturbated silty clay sediments, containing higher amounts of IRD, and highly variable biogenic content. It was recovered from the bottom of the studied interval until 2.54 mbsf of the cores, in alternance with interlaminated sediments (Fig.2.3.1). Above that alternance, approximately between 1.50 and 2.54 mbsf the Bioturbated IRD rich sediments were recognized in all the cores, with IRD content more abundant at the base while it is rather sparse at the top. Hence, we have applied the terms and Massive-IRD-rich sediments, to better describe the levels with greater quantity of IRD grains. This characteristic was recorded also on the XRF Zr/Rb (proxy of grain size) ratios that slightly decrease upward along that interval in each core. While Br/Ti (proxy for bio productivity) and Ca/Ti ratios (proxy for biogenic/terrigenous sediment source) slightly increase from 0.09 to 1.13 and from 0.68 to 2.71 respectively.

The $CaCO_3$ and O.M. contents are relatively low, oscillating from 1.13 to 5.00% and from 1.4 to 2.2%, respectively. While C_{org}/N_{tot} ratios decrease upward from 14.3 to 9.0 (Fig.2.3.3). The sediment colour varies from 2.5Y 5/1 grey, on the core GS-02, 5Y4/1 dark grey on CAGE-15, and 5Y4/2 olive grey on IRIDYA-02.

2.3.2 – Interlaminated sediments

The interlaminated sediments were easily recognized on x-radiographs images due to its internal structure formed by continuous alternation of millimetric silty-clay laminae with millimetric to centimetric fine sand layers. We identified three intervals of this lithofacies on each studied core, the younger of which is always topped by the bioturbated IRD rich mud. These sediments are rarely bioturbated and mostly barren. Sparse or layered IRD can occur on the upper two intervals of this facies while the lowermost interval differs from the other two due to a massive occurrence of IRD within the interlaminated structure (Fig.2.3.1).

In comparison with other lithofacies, these sediments have very low ratios of Br/Ti (0.06 - 0.42) and Ca/Ti (0.63 - 2.01) that is compatible with the low $CaCO_3$ content (below 5,80%), while the Zr/Rb is very high, reaching 3.70. This facies is also characterised by the higher content of O.M. and C_{org}/N_{tot} ratios (up to 3.46% and 21.35 respectively) (Fig 2.3.3). Its colours are 5Y4/2 olive grey, 5Y3/2 dark olive grey on the core IRIDYA-02, 2.5Y4/1 dark grey, 5Y4/1 dark grey on CAGE-15, and 5Y3/1 very dark grey on GS-02.

Along the Western Svalbard, interlaminated deposits are typically associated with hyperpycnal and hypopycnal flows (c.f. Lucchi et al., 2013) and sediment plumes, causing very high sedimentation rates during the intense melting episodes of glacial terminations (Hesse et al., 1997; Knutz et al., 2002; Tripsanas and Piper, 2008; Lucchi et al., 2013; Ó Cofaigh et al., 2013; Laberg and Dowdeswell, 2016; Bellwald et al., 2020). Thus, each interval of this particular facies was associated with a specific MWP or Heinrich-like event (Fig.2.3.3) based on the ^{14}C results detailed in the Chapter 1.

2.3.3 – Heavily bioturbated sediments

This lithofacies was recovered at the uppermost ~1.50 mbsf of all three cores (Fig.2.3.1), and it is characterised by silty clay sediments, which are pervasively bioturbated, very rich in bioclasts, and poor on IRDs contents. The sediment colour varies among the cores between 2.5Y5/1 grey on the core GS-02, 5Y4/1 dark grey on CAGE-15, and 5Y4/2 olive grey on IRIDYA-02, according to Munsell (2009).

Considering all the cores and the other lithofacies, the Heavily bioturbated are characterised by the higher values of Br/Ti, and Ca/Ti. With a clear increasing upward trend that reaches the maximum values found in this study, of 1.94 for Br/Ti, and 21.71 for Ca/Ti. In agreement with the $CaCO_3$ contents, which also shows an upward increase from 3.95 to 16.56%. While the organic matter (O.M.) slightly decreases upwards from 2.24 to 1.42%, with the C_{org}/N_{tot} ratio having a similar trend, dropping from 9.9 to 8.0 (Fig. 2.3.3). The Zr/Rb ratios also increase upward but with a slighter tendency with values between 1.09 and 3.05.

Based on the characteristics of those sediments, and the position of this facies, on the topmost of the sedimentary sequence, the Heavily bioturbated interval obviously represents the Holocene period on the study area.

2.3.4 – Oxidized layers

Three oxidised layers (Ox-0, Ox-1 and Ox-2) were described to occur on the upper and middle slope portions of the Storfjorden trough by (Lucchi et al., 2013). This thesis followed the same designation system since each one of those layers have been recovered. In addition, a fourth layer was identified during the present study, and named Ox-3.

Due to high concentrations of Fe-oxides minerals, the colour of those levels are quite different from the other sedimentary facies, varying between 2.5Y 4/3 olive brown (Ox-0), 2.5Y4/4 olive brown and 2.5Y5/3 light olive brown (Ox-2), 5Y4/3 olive (Ox-3). The colour characteristic facilitated the visual identification of those layers during the description of the cores, and also caused the strong peaks that were recognised in the red/green ratio obtained from the colour scan of these cores (Lucchi et al., 2013)..

The Ox-3 is the lowermost level, occurring on the cores GS-02 and CAGE-15, below the oldest interlaminated interval but it was not reached by the core IRIDYA-02, probably due to its shorter length. In all three cores, Ox-2 and Ox-1 were recovered, Ox-2 occurs below the uppermost interlaminated interval, and the Ox-1 is located within the uppermost IRD reach interval. The uppermost layer is the Ox-0, which is located at the sea-floor surface marking the present-day oxidation front that was recovered only in core GS-02.

Lithofacies	Bioturbated IRD rich	Interlaminated	Heavily Bioturbated
Photograph			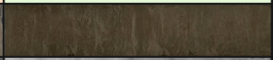
X-radiograph			
IRD content	Rich	Varies from poor to very rich	Rare
Foraminifera	Varies from poor to very rich	Barren	Rich
Sediment colour	Dark gray	Dark gray	Olive gray
CaCO3	1.13 - 5.00%	0.41 - 5.80%	3.95 - 16.56%
Org. matter	1.40 - 2.20%	0.44 - 3.46%	1.42 - 2.24%
Corg/Ntot	9.0 - 14.3	12.5 - 21.3	8.0 - 10.0
Org. matter provenance	Continental-marine transition	Continental	Marine
Zr/Rb	≤ 2.42	≤ 3.70	≤ 3.05
Br/Ti	≤1.13	≤0.42	≤1.4
Ca/Ti	≤2.71	≤2.01	≤21.71

Figure 2.3.2: Synthesis of the main lithofacies physical and compositional characteristics. Dark gray on X-radiographs indicates low-density sediment.

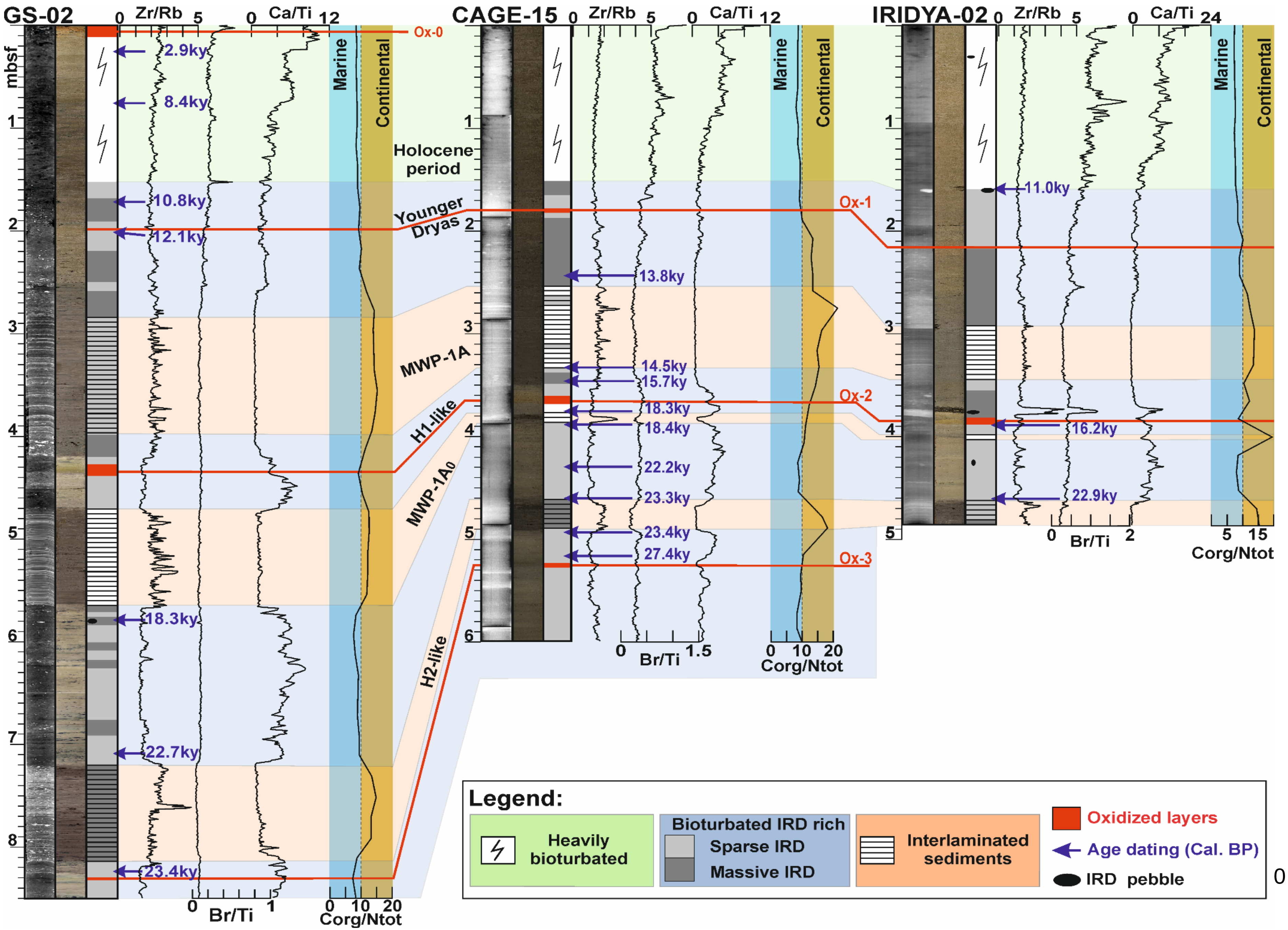

GS-02
CAGE-15
IRIDYA-02
mbsf
Zr/Rb
Ca/Ti
Br/Ti
Corg/Ntot
Marine
Continental
Ox-0
Ox-1
Ox-2
Ox-3
2.9ky
8.4ky
10.8ky
12.1ky
18.3ky
22.7ky
23.4ky
13.8ky
14.5ky
15.7ky
18.3ky
18.4ky
22.2ky
23.3ky
23.4ky
27.4ky
11.0ky
16.2ky
22.9ky
Holocene period
Younger Dryas
MWP-1A
H1-like
MWP-1A0
H2-like
Legend:
Heavily bioturbated
Bioturbated IRD rich
Sparse IRD
Massive IRD
Interlaminated sediments
Oxidized layers
Age dating (Cal. BP)
IRD pebble

0

Figure 2.3.3: The figure reports the X-ray images (dark = low density), photographs, lithofacies synthetic log, XRF sediment ratio of Zr/Rb, Br/Ti, and Ca/Ti and CHN profiles of the cores. Shaded indicates the three lithofacies: in pink the interlaminated sediments, in light blue the bioturbated IRD rich sediment and in Green the heavily bioturbated sediments. Some age dating results of ore CAGE-15 are not shown on this figure due to difficult visualisation, for more detail see Fig. 2.3.4.

2.3.5 – Micropaleontological content

2.3.5.1 – Planktonic foraminifera

The micropaleontological investigation of the studied sediment cores was performed quantitatively along the LGM-T1 interval of core CAGE-15 (2.39-5.24 mbsf). The planktonic foraminifera (PF) dominant species found on the samples is *Neogloboquadrina pachyderma* (Fig.2.3.4*). Neogloboquadrina incompta, Globigerina bulloides* and *Turborotalita quinqueloba* were also present, but more commonly found in the heavily bioturbated lithofacies on the top of the cores.

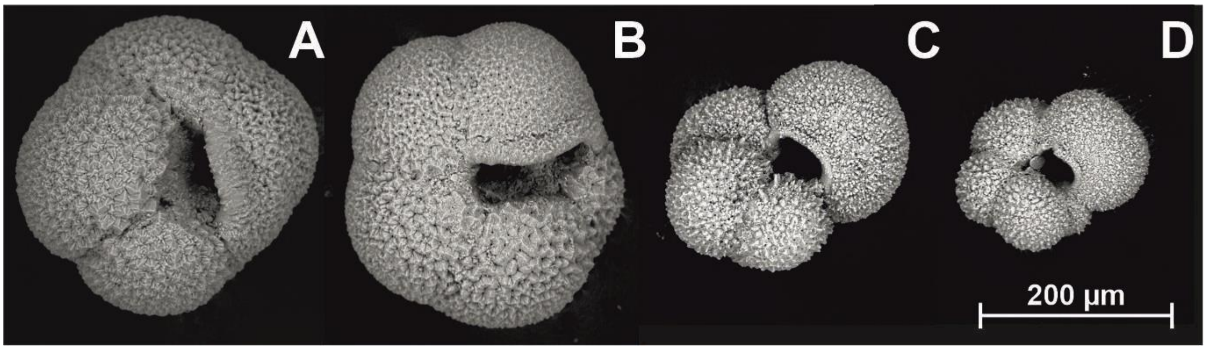

Figure 2.3.4: Scanning Electron Microscopy (SEM) images of planktonic foraminifera. A to D: Neogloboquadrina pachyderma.

Between 5.24 and 3.50 mbsf of the core CAGE-15, the flux of PF per cm² per year (PF/cm²/yr) shows several prominent oscillations that occur within the bioturbated IRD rich mud intervals (Fig.2.3.7), while the three interlaminated intervals are characterised by extremely low PF fluxes or barren intervals that reaches zero PF/cm²/yr, due to samples with no PF.

Prominent peaks on the curve of PF Flux were observed just a few centimetres below each one of the interlaminated facies (Fig.2.3.7). The base limit of the H2-like interval is located at only 6 cm above a concentration peak of $0.81e^5$ PF/cm²/yr (4.96 mbsf), having an age of 23.42 cal ky BP. While the base of the MWP-1A0 is located 8 cm above a peak of $0.94e^5$ PF/cm²/yr at 3.92 mbsf, having an age of 18.38 cal Ky BP, whereas the base of the MWP-1A is preceded by the highest PF flux concentration found along the T1 in this study ($1.54e^5$ PF/cm²/yr), at 3.53 mbsf having an age of 15.72 cal Ky BP.

Remarkable peaks of PF flux were recovered inside IRD rich mud intervals. Reaching $1.07e^5$ PF/cm²/yr at 4.35 mbsf with an age date of 22.16 Ky cal BP, and 3.97 e^5 PF/cm²/yr at 5.16 mbsf with an age date of 27.37 Ky cal BP, followed by the highest peak recognized along the study ($4.29e^5$ PF/cm²/yr) at 5.12mbsf. In these cases, after the peak the concentration decreases are less intense, falling to values that are still relatively high ($0.70e^5$ PF/cm²/yr).

2.3.5.2 – Benthic Foraminifera

Although the micropaleontological investigation performed and described on this thesis focus on the planktonic foraminifera, the benthic specimens remain an important source of information about bottom waters conditions and should not be left aside in any paleoceanographic reconstruction. Therefore, the benthic assemblage on the sediments was observed, and one aspect was particularly noticeable: the majority of the individuals are slightly or completely broken (Fig.2.3.6), while the intact tests represent a very little fraction of the recovered material.

Also, the dominant species recognized is the *Cassidulina laevigata* (Fig.2.3.5.A and Fig.2.3.5.B). The species Cibicides wuellerstorfi (Fig.2.3.5.C and Fig.2.3.5D), which commonly occurs in the heavily bioturbated lithofacies of the uppermost part of the core (0-1.5 mbsf), was also recovered in the intervals characterised by peaks of the PF concentration (Fig.2.3.7).

The other species identified occasionally on the samples includes *Astrononion gallowayi, Cassidulina laevigata*, *Dentalina advena*, *Elphidium incertum, Globobulimina auriculata f. artica*, *Islandiella norcrossi*, *Lenticulina* spp., *Melonis barleeanum*, *Nonionella iridea*, *Quiqueloculina agglutinata*, *Spiroloculina norvegica*, and *Triloculina trihedra*.

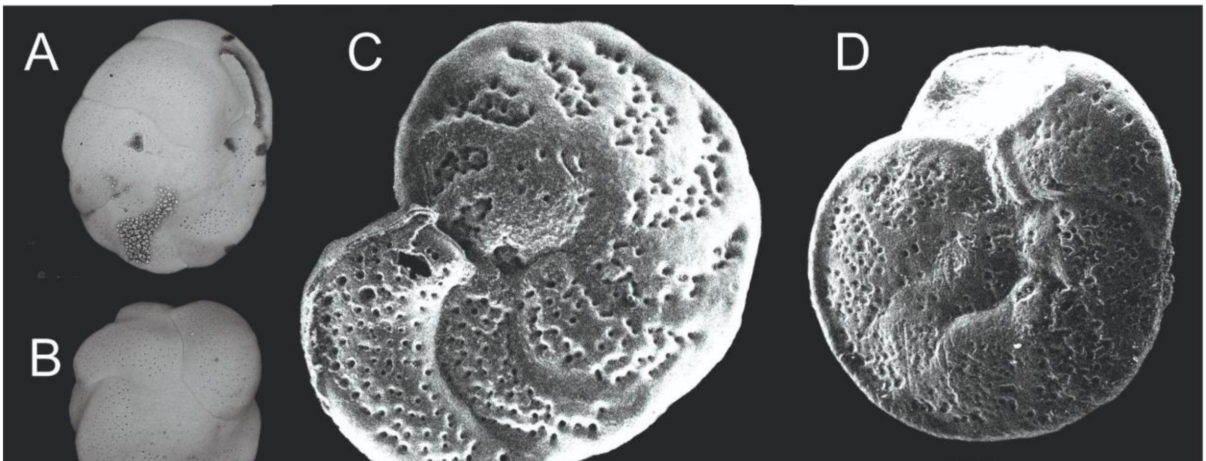

Figure 2.3.5: SEM images of benthic foraminifera. A and B: Cassidulina laevigata; C and D: Cibicides wuellerstorfi.

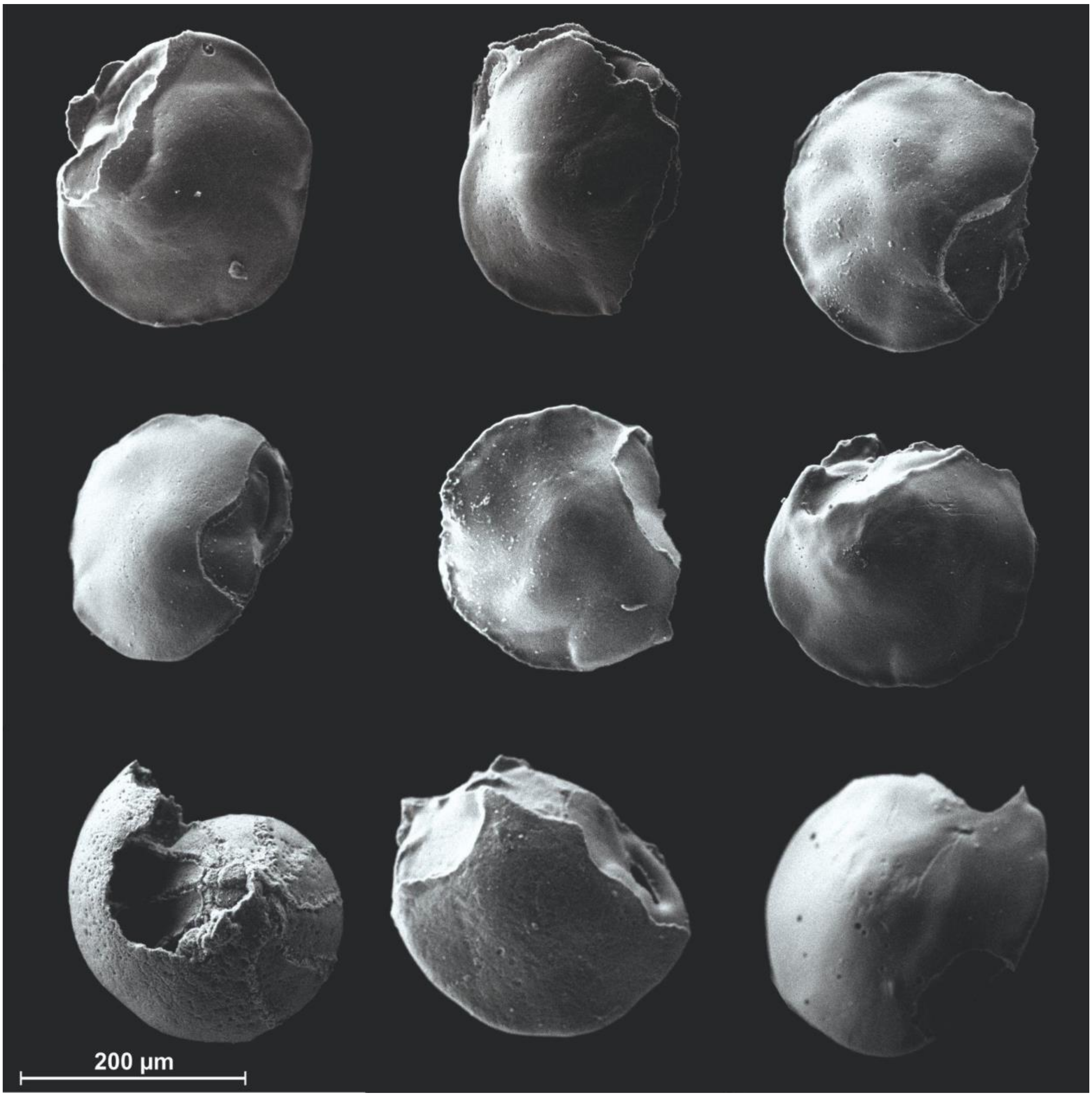

Figure 2.3.6: SEM images of broken or ruined benthic foraminifera, mainly rotalids (Cassidulina ssp. and Cibicides spp.).

2.3.6 – Ice Rafted Debris

Likewise, the micropaleontological content, the IRD (>0.5 mm) present in the samples of core CAGE-15 were quantified, revealing a great variation on the IRD flux along the high-resolution studied interval (LGM-T1). The higher IRD/cm²/yr values were recognized on strong peaks, always below the bottom boundary of the interlaminated sediment lithofacies, and usually 2-3 cm above the major PF/g.sed peaks (Fig.2.3.7).

The H2-like interlaminated interval (4.67-4.91 mbsf), has the highest concentration at the bottom (1147 IRD/cm²/yr), followed by an oscillation between 461 and 129, until the top of the event. While the H1-like event is composed of two separated peaks (603 and 679 IRD/cm²/yr). The first one, at the base limit of the Ox-2, at 3.65 mbsf, and the second at 3.50 mbsf (Fig.2.3.7).

The lower values for IRD flux were identified within the interlaminated facies associated with the MWP-1A$_0$ (from 3.79 to 3.84 mbsf) and the MWP-1A (between 2.54 mbsf and 325 mbsf). During both events, the IRD fluxes remain below 20 IRD/cm²/yr, reaching zero several times.

2.3.7 – Oxygen isotope ($\delta^{18}O$)

Along the 1-cm resolution sampling interval of the core CAGE-15, the oxygen isotope measurements were performed on *N. pachyderma*. Two general trends were recognized on the $\delta^{18}O$ curve. The first with a gradual increase (progressive cooling), between the base of the H2-like event and the base of the MWP-1A$_0$, followed by a second opposite trend, with a decreasing tendency (warming), from the MWP-1A$_0$ to the top of the H1-like event. Additional sharp shifts on the curve were present within the cooling trend. In total, four sharp decreases on the $\delta^{18}O$ curve were recognized, corresponding with the main meltwater events recorded on the sediments (Fig.2.3.7).

The first sharp decrease, on the curve was also the smallest (4.45 to 4.01 within 4 cm) and occurs during the onset of H2-like event; The second occurs along the MWP-1A$_0$ (5.24 to 3.93 within 9 cm); The third marks the onset of the H1-like and was the most abrupt one (4.72 to 3.61 within only 1 cm); The last decrease was recognized at the final stage of the H1-like event (4.65 to 3.28 within 5 cm). Each one of these episodes were followed by increases on the curve. Unfortunately, PF barren sediment along the MWP-1A interval, made impossible to carry out continuous analyses also within this event.

Additionally, the $\delta^{18}O$ curve from the North Greenland Ice Core Project (NGRIP) from Rasmussen et al., (2014) was selected in order to compare the results from this thesis with other paleoclimate records from the Arctic region. The interval used covers the period between 28 and 13 ky BP, and contains the records of the Bølling Warming, and the Greenland interstadials 1 and 2 (GS-1 and GS-2) (Fig.2.3.9).

2.3.8 Magnesium Calcium ratios

The highest Mg/Ca ratio (0.77) was recognized at 5.12 mbsf (table 4), corresponding with the PF/cm²/yr peak at ~27.0 cal ky BP (Fig 2.3.8), with an estimated temperature of 3.2 ± 0.5ºC. Also, very similar ratios (0.65 and 0.66) were measured at 4.96, 3.90 and 3.52 mbsf. Those levels correspond respectively to the PF flux peaks found beneath the H2-like, MWP-1A$_0$ and MWP-1A events, indicating sea surface estimated temperatures of 2.3 ± 0.5ºC for all three levels (Fig.2.3.8).

Along the interval with relatively high PF/cm²/yr between the H2-like and the MWP-1A₀ events, relatively low ratios of 0.60 and 0.58 were measured respectively at 4.35 and 4.21 mbsf. Those ratios lead to estimated sea surface temperatures of 1.9 ± 0.5ºC and 1.7 ± 0.5ºC for the period ~22.0 and 20.8 ky cal BP. The lowest Mg/Ca ratio of 0.56, was measured at 381 mbsf, corresponding to a relatively small PF/cm²/yr peak located at the top of the MWP-1A₀ deposit (~18.0 ky cal BP).

Core	Depth (mbsf)	Mg/Ca	Al/Ca	Fe/Ca	Sea Surface Temperature
CAGE-15	352	0.65	44.88	300.04	2.3 ± 0.5ºC
CAGE-15	381	0.56	10.56	19.11	1.6 ± 0.5ºC
CAGE-15	390	0.65	15.22	42.25	2.3 ± 0.5ºC
CAGE-15	421	0.58	8.05	17.35	1.7 ± 0.5ºC
CAGE-15	435	0.60	4.96	35.58	1.9 ± 0.5ºC
CAGE-15	496	0.66	7.53	39.23	2.3 ± 0.5ºC
CAGE-15	512	0.77	8.61	34.24	3.2 ± 0.5ºC

Table 2.3.2: Samples analysed for Mg/Ca, Al/Ca and Fe/Ca measurements. Sea surface water temperature estimations based on the Mg/Ca ratios and following (Kozdon et al., 2009).

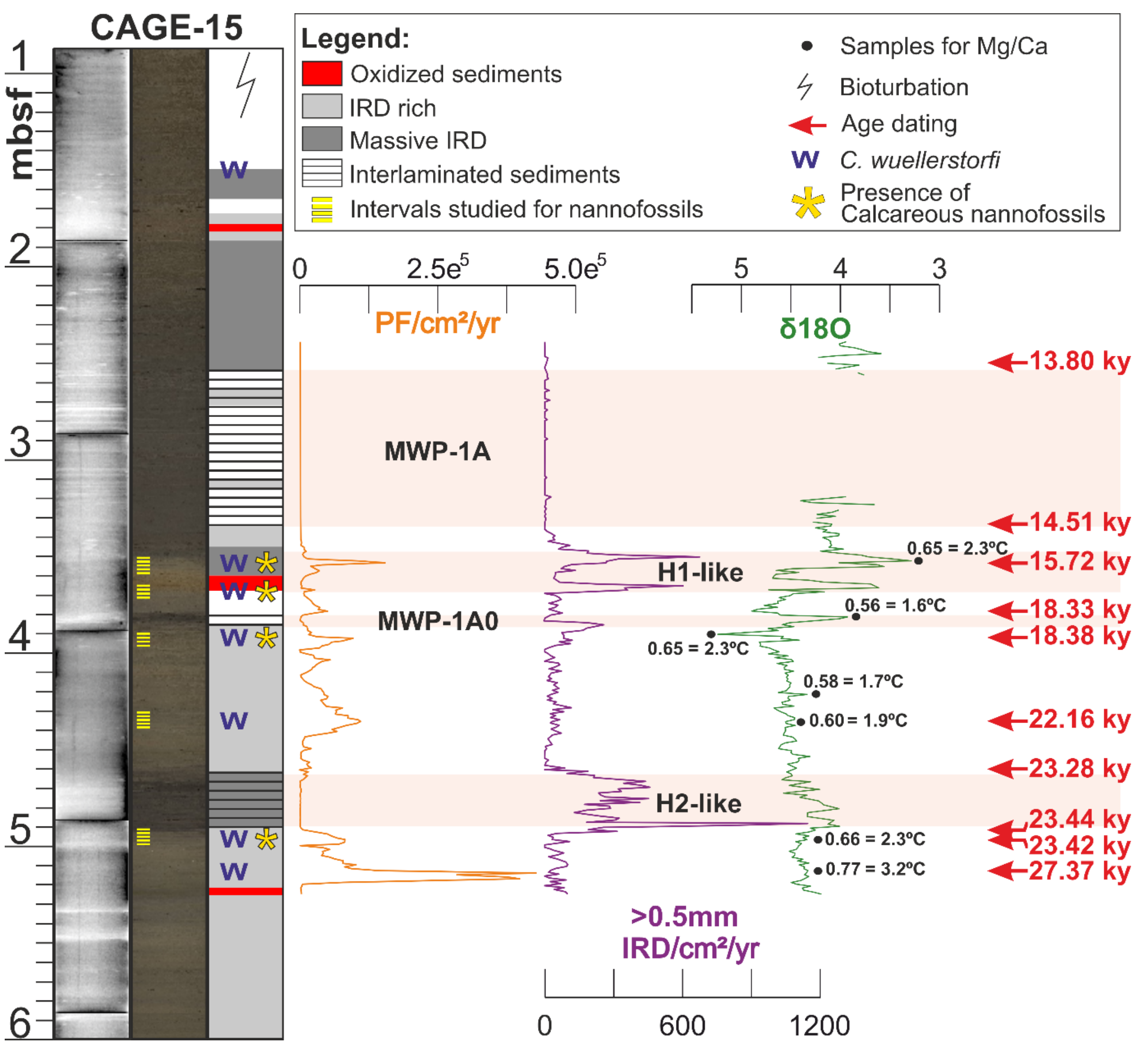

Figure 2.3.7: Interval between 0.90 and 6.00 mbsf of the core CAGE-15. The figure reports the X-ray images (dark = low density), photographs, lithofacies synthetic log with indication of the occurrence of the benthic foraminifera C. wuellerstorfi (blue W) and nannofossils (yellow star), and the diagrams of PF flux (orange curve), IRD flux (purple curve), and δ^{18}O (green curve). Black dots indicate the measured Mg/Ca ratios used to estimate water temperature following (Kozdon et al., 2009).

2.3.9 - Calcareous nannofossils

The absolute abundance of calcareous nannofossils per gram of sediment (n/g), was calculated for the 23 selected sub-samples of the core CAGE-15 (Table 2.3.3). These particular samples were collected with a 2 cm spacing and covered the intervals where the major PF concentration peaks were previously recognized (Fig 2.3.4). The highest values identified are 1.82 and 1.54x10^8, respectively found at the base of the H2-like (4.91 mbsf), and below the MWP-1A deposits (3.53 mbsf). In both cases with relatively low abundance of reworked nannofossils (0.62 and 0.29x10^8, respectively), coinciding with the PF/g.sed peaks, and the presence of *Cibicides wuellerstorfi (*Fig.2.3.8). Thus, it can be associated with periods when there were predominant sea ice free conditions and bottom currents activity in the study area.

Also, relatively high values of nannofossil abundance (1.03 and 1.10x10^8 n/g) were found again respectively at the base of the H1-like and the MWP-1A$_0$ (3.69 and 3.89 mbsf respectively), with low abundance of reworked material (0.59 and 0.47x10^8). Those intervals also coincide with the presence of *Cibicides wuellerstorfi* and foraminiferal peaks (Fig.2.3.8).

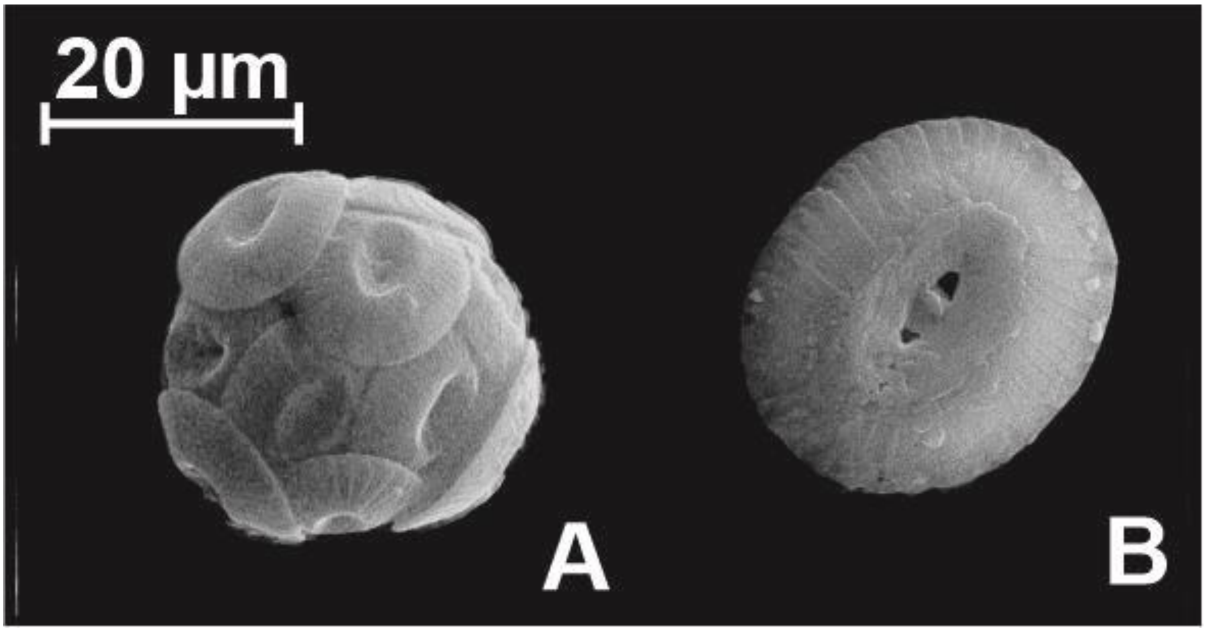

Figure 2.3.8: SEM images of calcareous nannofossils. A and B: Coccolithus pelagicus.

Core	Depth (mbsf)	Total abundance	Total Reworked	Meaning
CAGE-15	3.51	$1.26x10^8$	$0.18x10^8$	Sea ice free conditions
CAGE-15	3.53	$1.10x10^8$	$0.39x10^8$	Sea ice free conditions
CAGE-15	3.55	$1.55x10^8$	$0.62x10^8$	Sea ice free conditions
CAGE-15	3.57	$0.28x10^8$	$0.40x10^8$	Intense sea ice cover
CAGE-15	3.59	$0.13x10^8$	$0.34x10^8$	Intense sea ice cover
CAGE-15	3.65	$0.10x10^8$	$0.25x10^8$	Intense sea ice cover
CAGE-15	3.67	$0.39x10^8$	$0.42x10^8$	Intense sea ice cover
CAGE-15	3.69	$0.87x10^8$	$0.59x10^8$	Seasonal sea ice
CAGE-15	3.71	$1.03x10^8$	$0.59x10^8$	Sea ice free conditions
CAGE-15	3.90	$1.10x10^8$	$0.47x10^8$	Sea ice free conditions
CAGE-15	3.92	$0.31x10^8$	$0.30x10^8$	Seasonal sea ice
CAGE-15	3.94	$0.78x10^8$	$0.62x10^8$	Seasonal sea ice
CAGE-15	3.96	$0.65x10^8$	$0.43x10^8$	Seasonal sea ice
CAGE-15	4.31	$0.45x10^8$	$0.38x10^8$	Seasonal sea ice
CAGE-15	4.33	$0.38x10^8$	$0.30x10^8$	Seasonal sea ice
CAGE-15	4.35	$0.28x10^8$	$0.24x10^8$	Seasonal sea ice
CAGE-15	4.37	$0.36x10^8$	$0.27x10^8$	Seasonal sea ice
CAGE-15	4.39	$0.39x10^8$	$0.26x10^8$	Seasonal sea ice
CAGE-15	4.92	$1.82x10^8$	$0.29x10^8$	Sea ice free conditions
CAGE-15	4.94	$1.11x10^8$	$0.23x10^8$	Sea ice free conditions
CAGE-15	4.96	$0.64x10^8$	$0.26x10^8$	Seasonal sea ice
CAGE-15	4.98	$0.29x10^8$	$0.22x10^8$	Intense sea ice cover
CAGE-15	5.00	$0.29x10^8$	$0.31x10^8$	Intense sea ice cover

Table 2.3.3: Samples analysed for calcareous nannofossil content. Relatively higher values of calcareous nannofossils total abundance (above $1.0x10^8$), intermediate values (from $0.3x10^8$ to $1.0x10^8$) and lower values (< $0.3\ x10^8$) were respectively considered to be indicative of sea-ice free conditions, seasonal ice cover, and intense sea ice cover conditions. *Shaded lines indicate levels that correspond to planktonic foraminiferal peaks.*

2.3.5 Core correlations and stratigraphy

The stratigraphic sequence is very consistent among the three cores, the same lithofacies were recognized and the presence of the oxidised layers was also considered. Our new 13 radiocarbon dates from the cores IRIDYA-02 and CAGE-15 are in good agreement with the age model previously reconstructed by (Caricchi et al., 2019) on the GS-02 core from which we used 7 results here (Table 1.3.1). Furthermore, the new data revealed new information regarding the time lapse between oceanographic changes recorded by planktonic foraminifera abundance and the onset of the main climatic events during T1.

Recognized at the bottom of the studied interval, the Ox-2 could be related to the early phase or inception of the LGM in this area, once it precedes our oldest age dated interval of the core CAGE-15, with result of 27.37 cal ky BP.

The onset of the lowermost interlaminated facies was dated in the proximity of the bottom of cores GS-02 and CAGE-15, showing results of 23.46 and 23.44 cal ky BP, respectively. Instead, the top limit of those interlaminations was dated on the cores GS-02 and IRIDYA-02, with respective results of 22.69 and 22.91 cal ky BP (Fig. 2.3.3). Hence, it has a good match with the timing of the Heinrich Event 2 (H2) (Heinrich, 1988; Bond et al., 1993; Bard et al., 2000; Mix et al., 2001)Therefore, hereafter we refer to this interlaminated interval as Heinrich-like Event 2 (H2-like).

The deposition of the second interlaminated interval started at 18.285 and 18.384 cal ky BP on the cores GS-02 and CAGE-15, respectively (Fig.2.3.3), concomitantly to the MWP-1A0 (Hanebuth et al., 2008; Clark et al., 2009; Crocket et al., 2011; Lucchi et al., 2013, 2015). Followed by the Ox-2, that was age dated in the core IRDYA-02 and resulted in 16.268 cal ky BP (Fig.2.3.3), coinciding with the timing of the Heinrich Event 1 (H1) (Bard et al., 2000; Clark et al., 2009). Also, the major concentration peak of planktonic foraminifera was found on the CAGE-15 core, only 7 centimetres above Ox-2 showed an age dating result of 15.72 cal Ky BP.

Furthermore, bottom and top limits of the uppermost interlaminated interval was dated on the core CAGE-15, respectively resulting in 14.518 and 13.80 cal ky BP, which matches with the MWP-1A (Deschamps et al., 2012; Lucchi et al., 2015). Above this event, occurs the last bioturbated IRD rich mud, which was dated in GS-02 and IRIDYA-02 with results of 12.08 and 10.97 cal ky BP, respectively (Fig. 2.3.3). Also, this last IRIDYA-02 age dating result is exactly on the transition to the Heavily bioturbated sediments and coincides with the onset of the Holocene period. Finally, the Ox-0, recognized only on the GS-02 core, is stated to be deposited somewhere after 2.87 cal ky BP and still represents the current oxidation front.

As most of the age dated levels were taken on the lithofacies transitions, it was possible to build a composed chronology for the last 27.5 cal ky BP, by stacking on the core CAGE-15, four age dating results from the other two cores. More specifically, the bases of the Ox-2 and Ox-1 layers, the base of Heavily bioturbated sediment, and the uppermost dated sample GS-02 next to seafloor (Fig.2.3.4).

Since the acc. rate was identified, the age-model was built, and the sediment density was measured in gr/cc by the Multi Sensor Core Logger, it was possible to analyse these different proxies on a time scale, along the 1-cm resolution sampling of the core CAGE-15. Hence our dataset could be compared with other climate records available for the Arctic region, such as the Greenland Ice Core (NGRIP) $\delta^{18}O$ record (Fig 2.3.9). Two Greenland Interstadials (GI), and the Bølling warming occurred during the time period investigated by this thesis.

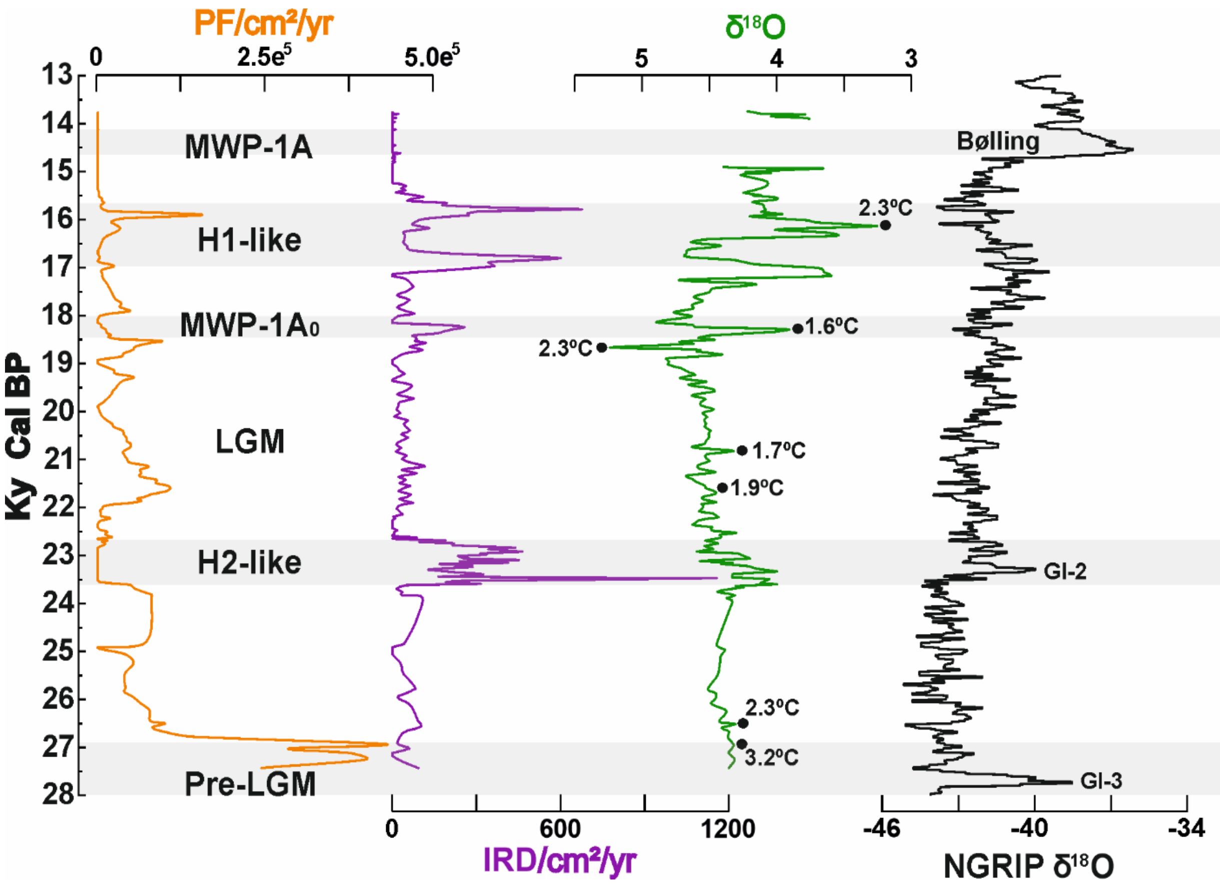

Figure 2.3.9: PF flux (orange curve), IRD flux (purple curve), and δ^{18}O (green curve) along the Bayesian age-depth model built for the 2.47-5.16 mbsf interval of the core CAGE-15. Black dots indicate Mg/Ca-derived sea surface temperatures. The Greenland ice core (NGRIP) δ^{18}O record (black curve), from Rasmussen et al., (2014), with the indication of main Greenland Interstadials (GI) (Bølling warming, GS-2, GS-3).

2.4 Discussions

At high latitudes marine environments, fluxes of PF and IRD are closely related with changes in ocean surface conditions over time. Thus, they can be used as proxies for paleoceanographic reconstructions (Cayre et al., 1999; Rashid et al., 2019).

The prominent peaks of PF flux identified in the core CAGE-15, suggest high productivity occurred during last glaciation. The high abundance of the carbonate biogenic fraction and the high productivity are also depicted by the values of Ca/Ti and Br/Ti ratio which trend was consistently observed in the other two studied sediment cores indicating similar environmental conditions between the Bellsund and Isfjorden sediment drifts. The presence of calcareous nannofossils within the PF peaks indicate the deposition occurred during seasonal or ice-free conditions such as those associated with polynyas. Periods with sea ice free conditions during the LGM were also recognized through biomarker proxy (IP25) from a site north-west of Svalbard by (Knies et al., 2018; El bani Altuna et al., 2024). These studies appear in good agreement with our results and interpretations, and the combined information points to the possible existence of a large-scale (regional), dynamic polynya that developed along the western margin of Svalbard during last glaciation, likely deriving from intense katabatic winds blowing from the adjacent ice mass.

Polynyas are known areas of dense water mass formation and sinking due to brine rejection that, in turn, drives the global thermohaline circulation (Tamura et al., 2008). The presence of mainly abraded or broken benthic foraminifera (*e.g. Cassidulina* ssp. and *Cibicides* spp.) together with taxa typical of shelf environment (e.g. *E. excavatum and C. reniformis*) can be associated with brine formation generating down-slope density currents remobilising the local benthic fauna. Intact tests of the large diameter (> 1.0 mm) and robust C. wuellerstorfi within the benthic foraminifera assemblage (Fig. 4) confirm the presence of vigorous bottom currents (up to 22 cm^{s-1} according to Saupe et al., 2023). On the contrary, the little fragmentation of the planktonic species can be related to a mainly in situ settling. According to (Rasmussen et al., 2007) and (Jessen et al., 2010), the presence of the benthic foraminifera C. wuellerstorfi in sediments is also indicative of warm Nord Atlantic Water influx that may have contributed to support both the bio productivity and the maintenance of polynyas in the studied area just after LGM. At the present day, dense waters sinking from the Arctic polynyas are the main source of the North Atlantic Deep Water, acting as a forcing mechanism of the northern part of the Atlantic meridional overturning circulation (AMOC) (Stouffer et al., 2006; Kuhlbrodt et al., 2007). A similar mechanism was described to occur during last glaciation in the Ross Sea (Antarctica) with the presence of grounded ice moving the coastal polynya seaward during the LGM and maintaining them directly above the continental slope until the retreat of the ice sheet (Weber et al., 2011).

The profile of $\delta^{18}O$ clearly indicates an overall cooling occurred from the base of the studied interval, considered to represent the pre–Late Weichselian glaciation, to the base of the MWP-$1A_0$, after which the profile switches to a general warming trend. However, within the general cooling trend, there are intervals characterised by sharply reduced $\delta^{18}O$ values that can be explained with either the onset of warm conditions or by the presence of fresh waters. Such intervals correspond to the interlaminated, IRD-rich facies of plumites deposited during the H2-like, MWP-$1A_0$, and H1-like events. The Ca/Mg ratio measured within the PF peaks located at the base of said events suggest that the evidence of ice sheet destabilisation (IRD peak) and melting recorded in the plumites was driven by episodic strong influx of heat transported in the area by the oceanic circulation. Therefore, the lower values of $\delta^{18}O$ measured within plumites, is associated to the presence of fresh water released during short periods of ice melting, and the presence of the benthic foraminifera C. wuellerstorfi in the sediments preceding the onset of melting conditions, confirm the occurrence of episodic incursions of the warm WSC during the last glacial period, modulating the dynamics of the paleo SBSIS.

2.4.1. A 7-step reconstruction from the LGM to the Holocene

According to what is discussed above, we provide a 7-step reconstruction of the evolution of the mutual interaction that occurred between the paleo SBSIS and the onset of paleoceanographic conditions during LGM and T1.

2.4.1.1 LGM inception

The oldest sediments investigated by this study are the bioturbated IRD rich, recovered at the bottom of the cores CAGE-15 and GS-02. According to our XRF and CHN data, it corresponds to a period of high primary productivity on the sea surface, due to high $CaCO_3$ (~10%), Ca/Ti (>4) and Br/Ti (>0.5) ratios, with O.M. coming from a marine source (C_{org}/N_{tot} >10) (Fig.2.3.3).

Also, our 1-cm resolution investigation of the core CAGE-15 highlighted an intense PF flux until 27.37 Cal ky BP (Fig 5), which precedes the inception of the LGM in Northern Europe occurred at ~26.0–25.0 ky BP (Clark et al., 2009; Patton et al., 2017). Our age-depth model showed very low accumulation rates for that interval (Fig.1.3.4.A), and the Mg/Ca ratio from PF shells has the higher value for this study (0.77), with an estimate sea surface temperature of 3.2ºC, which is close to current interglacial conditions of 3.5ºC (Boyd and D`Asaro, 1994; Nilsen et al., 2016; Bensi et al., 2019).

Together, those different proxies are clear evidence of predominant sea-ice free conditions due to higher temperatures (or a polynya), and active bottom currents. Indicating water circulation coming from the North Atlantic (WSC) before the LGM inception in the area. We interpret the interval between the Ox-2 and the H2-like event as contourites drift deposits, previously described on this region (Andreassen et al., 2008; Pedrosa et al., 2011; Rebesco et al., 2013).

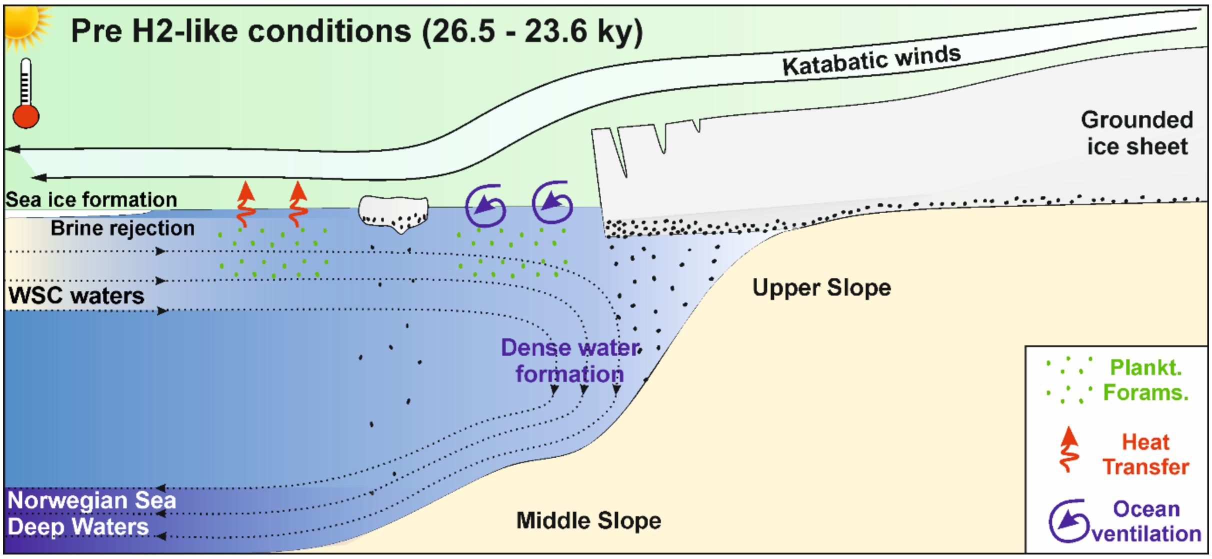

Figure 2.4.1: Conceptual model of the climate and oceanographic setting during the period between the onset of the LGM and the H2-like event. WSC: West Spitsbergen Current.

2.4.1.2 Heinrich-like Event 2

At 23.44 ky cal BP, the age-depth model for the core CAGE-15 clearly indicates a significant increase in accumulation rates (Fig.1.3.4.A), which is in good agreement with the one published by (Caricchi et al., 2019) for the core GS-02. At this point, a peak of $0.81e^5$ PF/cm²/yr is ended by a drop towards zero, immediately followed by the arrival of the oldest interlaminated sediments and most intense IRD deposition recorded in our data (1147 IRD/cm²/yr). The decrease in $\delta^{18}O$ and Mg/Ca ratios on N. pachyderma tests (Fig.2.3.5) indicates an intense arrival of meltwater from the ice sheet. This remarkable event is well recorded in all three cores, especially on the XRF ratios and CHN data with up to 3% of O.M. with continental sources. Our age-dated result of 22.91 ky cal BP from the core IRIDYA-02 agrees with the 22.69 ky cal BP from a level previously dated on the core GS-02 and indicates the end of this event in the study area.

The timing of this interlamination deposition matches with the H2 event recorded at the Labrador Sea (Heinrich, 1988; Bond et al., 1993; Mix et al., 2001). Hence, our dataset indicates a massive delivery of icebergs to the North Atlantic also coming from the SBSIS (hereafter called Heinrich-like event), synchronously with the discharge from the Laurentide Ice Sheet. The large release of fresh water usually associated with Heinrich events (Pedro et al., 2022; Fan et al., 2023), has probably weakened the AMOC affecting climate beyond the Arctic (Kuhlbrodt et al., 2007; Tamura et al., 2008; Rae et al., 2014; Knies et al., 2018; Fan et al., 2023). The increase in the accumulation rate due to the terrigenous material input should be the main reason for the drop in PF fluxes. Our data shows that the H2-like event induced those conditions in the study are for at least 0.51 ky.

Once the H2-like was ended, the iceberg discharge ceased. The sedimentary facies on our cores changed and the IRD/cm²/yr on the sediments rapidly decreased to zero. Concomitantly, the PF/cm²/yr curve shows the slow foraminiferal repopulation process that was interrupted once, suggesting a period with widespread sea ice covering the shelf break region (Fig.2.4.2). This event was probably caused by strong ocean stratification forced by large amounts of cold freshwater released on the surface. With the freshwater perturbation ending, the iceberg discharge returned to pre-H2 conditions, and the PF population began to grow back intensely until reaching a concentration peak of $1.07e^5$ PF/cm²/yr at 22.16 ky cal BP, indicating a possible polynya, and consecutively deep-water formation and AMOC during the LGM.

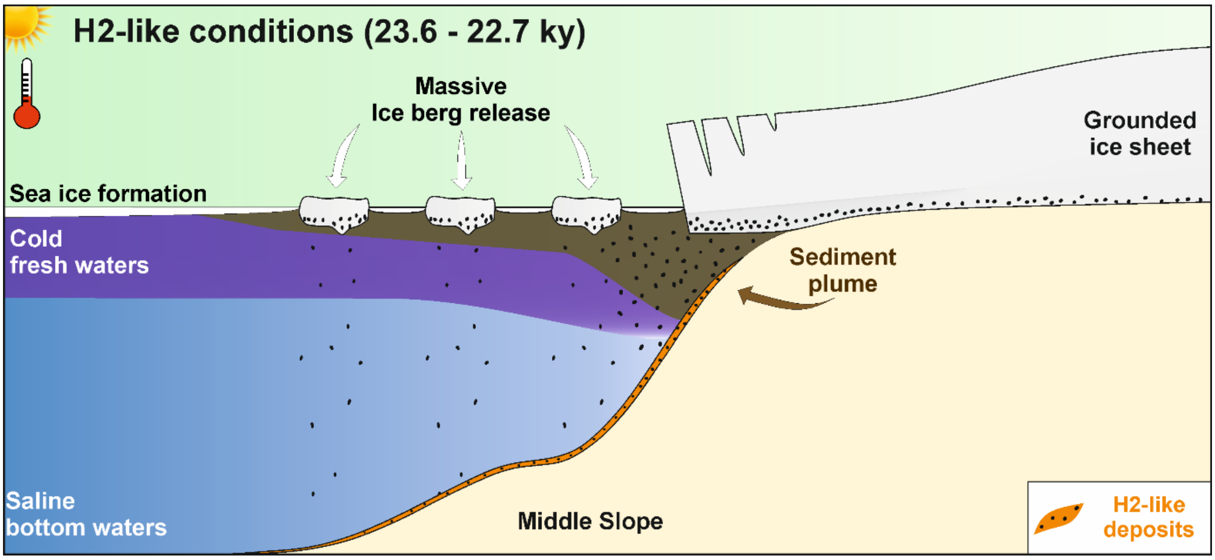

Figure 2.4.2: Conceptual model of the climate and oceanographic settings during the H2-like event.

2.4.1.3 Early deglaciation phase and MWP-1A$_0$

The following period is characterised by intense oscillation of the PF population until a peak of 0.94e^5 PF/cm²/yr, occurred at 18.38 ky cal BP. A period when increased Northern Hemisphere summer insolation (Broecker et al., 2010) triggered the partial collapse of multiple ice sheets (Clark et al., 2004), causing the MWP-1A$_0$ (Fig.2.4.2). This event is associated with a rapid global RSL rise between 10 and 15 m after the LGM, which marked the T1 onset (Yokoyama et al., 2000; Rinterknecht et al., 2006; Hanebuth et al., 2008; Clark et al., 2009; Crocket et al., 2011; Lucchi et al., 2013).

As expected, the oceanographic perturbation during the MWP-1A$_0$, shut down the polynya adjacent to the SBSIS, PF flux drops to zero, followed by another peak of 3.06 IRD/g.sed, while $\delta^{18}O$ rapidly decreases from 5.24 to 3.93 (Fig.2.3.7). Interlaminated deposits of terrigenous sediments were recovered by all three cores with low (close to zero) $CaCO_3$, Ca/Ti and Br/Ti ratios, high Zr/Rb (up to 4.0) and continental sourced O.M (always >10, and reaching 20 on the core IRIDYA-02) (Fig.2.3.3). In comparison with the previous event (H2-like), our data show that MWP-1A0 onset is characterised by a smaller release of icebergs which is stopped right after the beginning of the event, followed by close to zero fluxes of IRD and PF. Although, Mg/Ca on PF indicates similar temperature/salinity conditions.

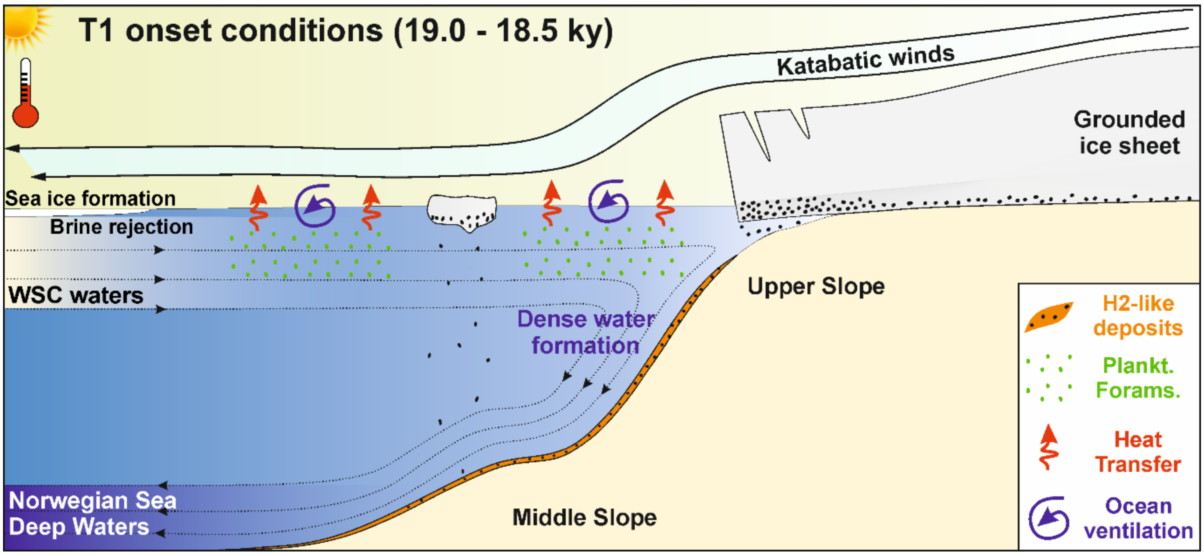

Figure 2.4.3: Conceptual model of the climate and oceanographic settings during the onset of the T1. WSC: West Spitsbergen Current.

This early deglaciation phase was followed by a few thousand years of weaker AMOC induced by the MWP-1A$_0$ perturbation (Bard et al., 2000; Clark et al., 2004; Rinterknecht et al., 2006). The large amount of freshwater released caused the lowest values on our $\delta^{18}O$ and Mg/Ca data. Inducing predominant sea ice covering over the slope area of NW Svalbard between ~19 and 17.6 ky (Müller and Stein, 2014). However, a small-scale planktonic repopulation began after this period, suggesting at least intermittent open waters SW of Svalbard causing low PF fluxes that oscillate between $0.45e^5$ and $0.47e^5$ PF/cm²/yr. until the Ox-2 layer. Previous studies on this region also recognized an oxidized layer associated with massive IRD deposition after the LGM (März et al., 2011; Lucchi et al., 2013, 2015; Carbonara et al., 2016; Caricchi et al., 2019).

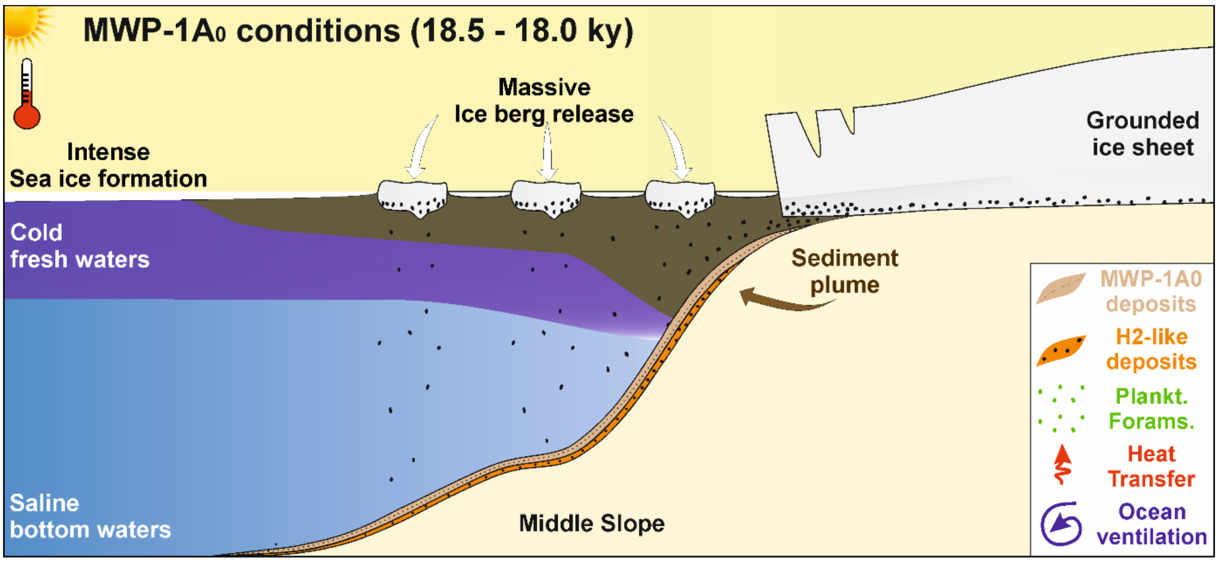

Figure 2.4.4: Conceptual model of the climate and oceanographic settings during the MWP-1A0.

2.4.1.4 Heinrich-like Event 1

The Ox-2 is found in all three cores, and it was stated to be deposited at 16.26 Ky cal BP on the IRIDYA-02 site. The bottom limit of this layer, in the 1-cm resolution investigation of the core CAGE-15, shows an episode of intense iceberg discharge with an initial peak of 603 IRD/cm²/yr., during an intense decrease on the $\delta^{18}O$ curve (Fig.2.3.7) caused by meltwater. Followed by momentaneous zero PF flux. Hence, we interpret that IRD episode as the onset of the H1-like in our data, also referred to as H1 first pulse or H1b which was described to occur ~17.5 ky (Bard et al., 2000; Clark et al., 2009). The difference between our age dating results and those previous works could be explained by the improvements in ^{14}C age calibration along the last decades.

However, the H1-like onset (or H1b) was followed by the most intense period of PF repopulation, when the flux reached the highest value here recognized for the T1 ($1.54e^5$ PF/cm²/yr). Clearly indicating sea ice free conditions SW of Svalbard at 15.72 ky cal. Furthermore, our measured $\delta^{18}O$ reached the lowest value (3.28) at this level, with Mg/Ca of 0.65, the same value found before the H2-Like and MWP-1A$_0$ events (Fig.2.3.7). This evidence agrees with the low values of sea ice biomarker proxy (IP25) for this period (Müller and Stein, 2014).

Furthermore, the presence of *C. wuellerstorfi* in this level indicates active AMOC delivering warm Atlantic waters to the area (Rasmussen et al., 2007; Lucchi et al., 2013). During a period with high summer insolation in Northern high latitudes (Clark et al., 2009; Broecker et al., 2010; Knies et al., 2018), the rising of atmospheric CO_2 and temperatures in Greenland (Buizert et al., 2014; Pedro et al., 2022), and the concurrent sea-level rise forcing the lift-off of shallow marine grounded ice streams along the Svalbard margin and the Barents Sea (Lucchi et al., 2013).

Those conditions exposed this marine based ice shelf to a heat flux that triggered another enormous iceberg discharge (Fig.2.4.2), comparable with the one during the H2-like onset, highlighted by the peak of $679e^5$ IRD/cm²/yr in our data. Here we interpret this moment as a second pulse of the H1, also known as the H1a that occurred at ~16.0 ky (Bard et al., 2000; Clark et al., 2009). The following decrease in foraminiferal population is the most abrupt one recorded for the entire deglaciation, reflecting the massive input of meltwater which caused immediate sea-ice covering on the Fram Strait and affected the thermohaline circulation (Knies et al., 2018).

2.4.1.5 Late Deglaciation and MWP-1A

The topmost interlaminated facies found in all three cores correspond to the MWP-1A event, the most drastic RSL rise (~20 m) during the T1 (Fairbanks, 1989; Bard et al., 1990, 1996; Hanebuth et al, 2000; Weaver et al., 2003; Fairbanks et al., 2005; Stanford et al., 2006; Deschamps et al., 2012; Lucchi et al., 2013). The interlaminated deposits in this area have been well described as plumites by (Lucchi et al., 2013, 2015). The MWP-1A onset is simultaneous with the climate warming that marked the beginning of the Bølling transition, ~14.7 ky (Stanford et al., 2006; Rasmussen et al., 2007; Patton et al., 2017), while our radiocarbon results show that the event was already finished before 13.80 ky cal BP. This consideration is in good agreement with the timing of 14.65–14.31 ky cal BP indicated by (Deschamps et al., 2012) from Tahiti records.

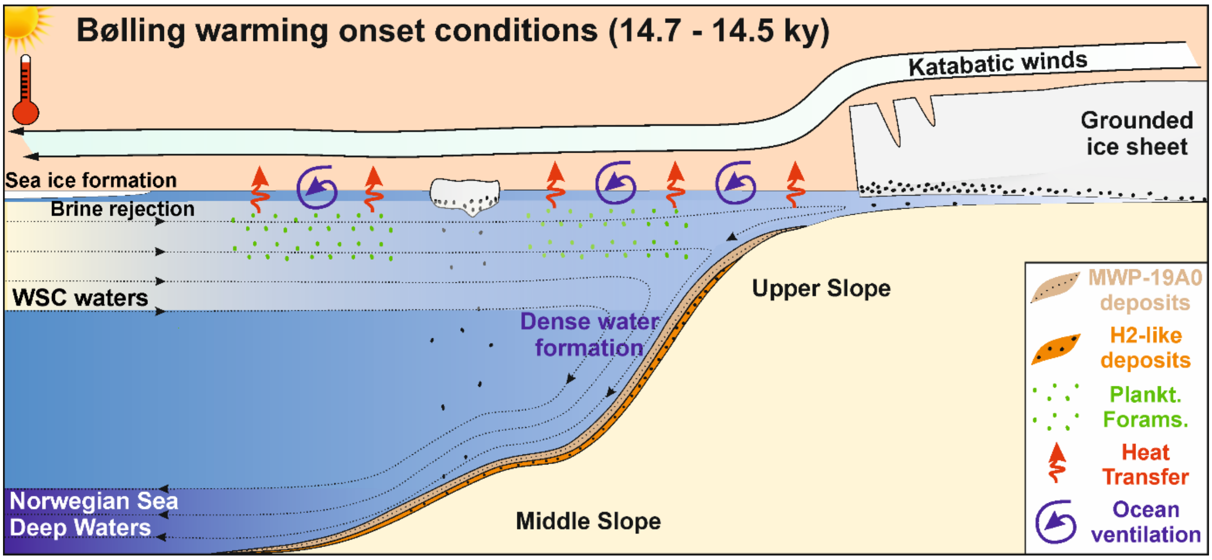

Figure 2.4.5: Conceptual model of the climate and oceanographic settings during the Bølling warming. WSC: West Spitsbergen Current

The complete absence of PF during the MWP-1A interval of our data demonstrates the enormous impact of this event in terms of sedimentation rates, oceanographic conditions and AMOC activity. Also, during this event the IRD/cm²/yr remained near zero. It suggests episodes when the icebergs were blocked on the shelf area, probably by the thick layer of permanent sea ice.

Beneath the sea ice, the plume formed by fine sediments and transported by the meltwater flux created the deposits of plumites. Furthermore, it reduced sunlight penetration acting as an extra obstacle to primary productivity and foraminiferal repopulation. The plumites deposition in the area is followed by a period of rising IRD/cm²/yr, due to icebergs freely floating again over the slope region, most likely coming from the main ice-streams South of Svalbard, the Storfjorden and Byørnøyrenna Trough Mouth Fans (Laberg and Vorren, 1995; 1996; Andreassen et al., 2008; Rebesco et al., 2011; Carbonara et al., 2016). However, zero PF/cm²/yr concentrations on our data indicate a long period of meltwater perturbation after the MWP-1A also recorded by low IP25 measurements of Müller and Stein, (2014), Knies et al., (2018) and Stein (2014).

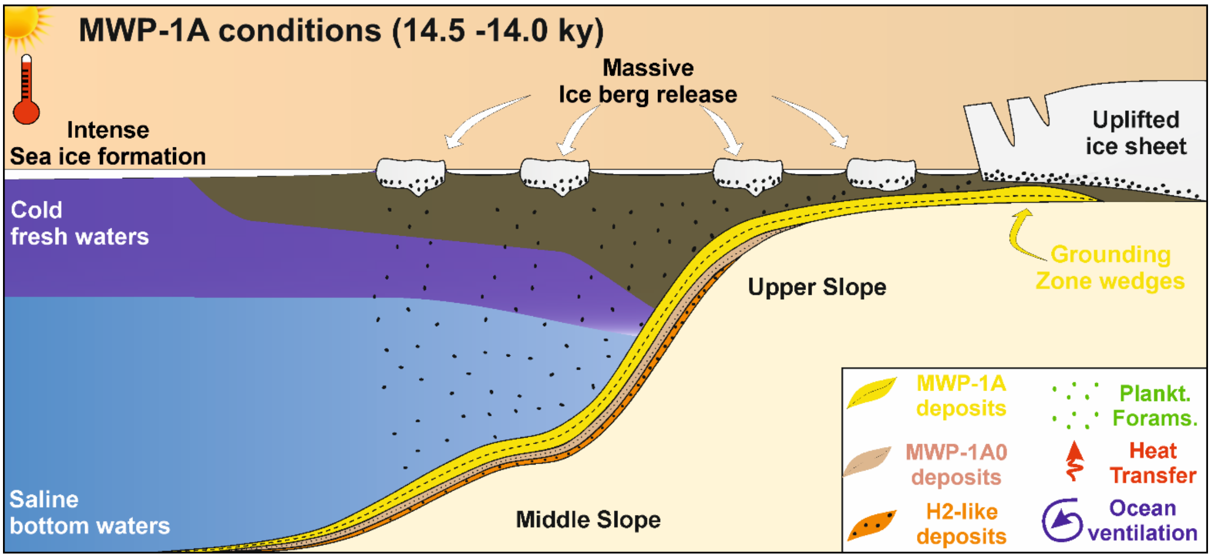

Figure 2.4.6: Conceptual model of the climate and oceanographic settings during the MWP-1A.

2.4.1.7 Holocene inception

Foraminiferal repopulation in this area only occurred at 10.97 ky cal BP, with the onset of the Holocene period. This event is marked by the lithofacies transition from IRD rich sediments to the Heavily bioturbated mud recognized on the upper part of the cores. The absence of IRD, the high $CaCO_3$ contents and the low rations of Corg/Ntot (>10) are the main evidence of the marine source of those sediments. The onset of the Holocene is also marked by the arrival of *C. wuellerstorfi* at the bottom of this lithofacies, indicating the arrival of North Atlantic intermediate waters through the WSC (Fig.2.4.7) along the middle-slope (Rasmussen et al., 2007). Under low sedimentation rates, this current is responsible for the formation of contourite drifts in the area (Andreassen et al., 2008; Pedrosa et al., 2011; Rebesco et al., 2013).

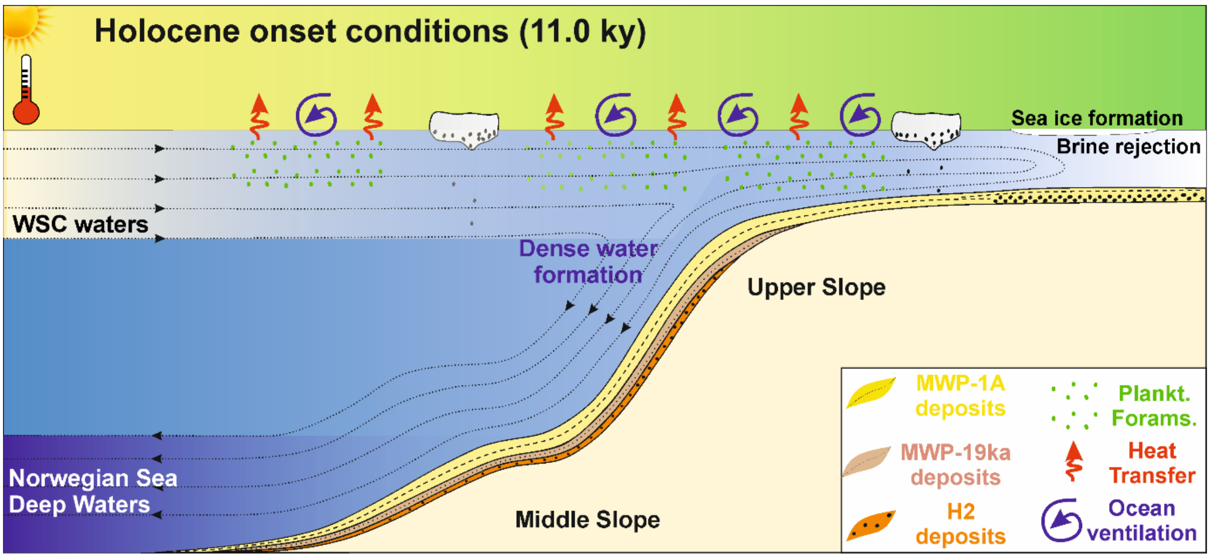

Figure 2.4.7: Conceptual model of the climate and oceanographic settings on the Holonce onset.

Chapter 3 – Automated counting of sediment laminations on X-ray images

3.1 Introduction

Glacial terminations are characterized by ice sheet instability generating accelerated iceberg calving and intense sediment laden meltwater effluxes both accompanying the ice sheet decay. A large amount of sediments are therefore released into the ocean. When turbid fluxes overcome the ice front, a large-scale fractionation process occurs, with fresh water rising to the sea surface carrying a load of suspended fine-fraction of sediments, and forming an apron-shaped surface plume (hypo-pycnal flow), whereas the coarse grained sediments sink generating dense bottom waters (hyper-pycnal flow) that descend the continental slope having characteristics similar to that of the turbidity currents (Fig. 3.1). Those hyper- and hypo-pycnal flows are responsible for the deposition of a typical deposit called plumites (sensu Hesse et al., 1997) that is commonly found in high-latitude marine environments. A plumite is characterised by fine-grained, silty-clay sediments interbedded with centimetric to millimetric thick sand/silt layers/horizons (Hesse et al., 1997). On the western continental margin of Svalbard, the fine-grained interval forming plumites is characterised by fine, planar laminations generated by shear strength of persistent bottom currents corresponding to the deep core of the Western Spitsbergen Current (Lucchi et al., 2013).

According to (Lucchi et al., 2013; 2015), the interlaminated sediments recognized in the studied cores, are the plumites associated with the major melting events (meltwater pulses) that occurred after the LGM, during the glacial termination T1. The details of the sedimentary structure within plumites may not be always very clear during a simple visual core-log description, but they can be easily recognized on X-radiographs of the cores, due to the different densities between the fine- and coarse-grained intervals (Fig. 3.2). Therefore, X-ray images are ideal for high-resolution, detailed counting and measuring of those sedimentary structures in a completely non-destructive analysis. The investigation of the quantity, thickness, and frequency of interlaminations in a deposit has the potential to reveal internal dynamics of meltwater pulse events (MWPs), and to investigate the possible trigger mechanisms. Such kind of analysis can be performed in an automatic and easily reproduced way by using image processing programs.

The first software used for the investigation of the interlaminated sediments was the BMPix and PEAK tools, which was firstly developed and tested on sediment cores from the southeastern Weddell Sea, in Antarctica by (Weber et al., 2010). However, there are other image processing softwares that also contains tools with potential to be tested for this kind of sedimentological and statistical analyses. In this chapter, the interlaminated deposits associated with the record of the MWP-1A recovered in the studied cores, were investigated using two independent imaging processing methods, the BMPix software using the PEAK tools, and the ImageJ software with the plot lanes tool. After comparing both methods, the final results were matched with the age-depth model described in Chapter 1, to understand the timeframe and the possible climatic significance and/or information on the ice sheet dynamics of the measured interlaminations within the meltwater event.

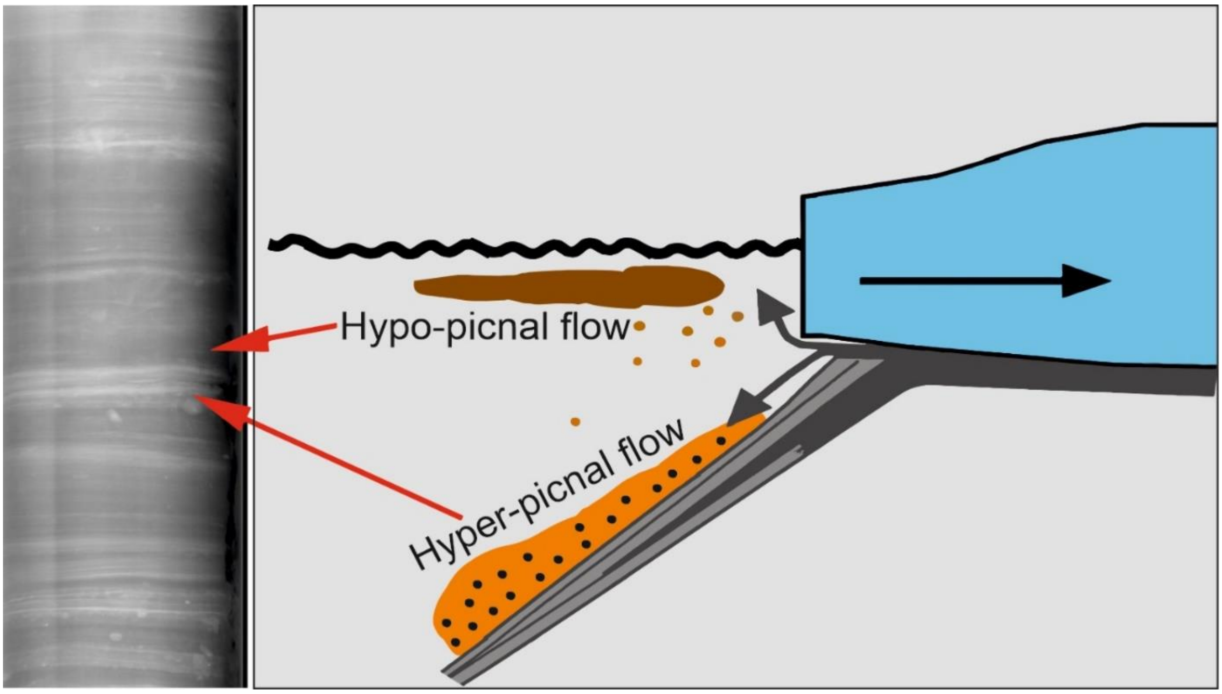

Figure 3.1 Illustration of the Hypo- and Hyper-picnal flows associated with meltwater release and plumite formation that is visible on the sediment core X-radiograph on the left side.

As the MWP-1A has occurred in a very short period of time (*ca.* 340 years, (Deschamps et al., 2012), the internal number of layers (either coarse- or fine-grained intervals), representing a major melting event, must be related with some internal short-term cyclicity (e.g. seasonal, annual, 11 year solar cycle), while the layering thickness is directly proportional to the accumulation rates (acc.rates) at each core. Therefore, the frequency (lamina/cm) will be inversely proportional to the acc.rate (years/cm), and intervals with lower frequencies clearly indicate periods when a greater amount of sediments was carried by the hyper- and hypo-pycnal flows released from the ice sheet, and *vice-versa*. Therefore, the frequency variations can be used as a proxy to recognize changes in flow intensity, revealing maximum and minimum periods of freshwater release during the event.

Once, the average acc.rate for the event was obtained from the Bayesian age-depth model of the core CAGE-15 with the best resolution possible, layering frequencies could be converted from lamina/cm to lamina/year. Furthermore, it became possible to determine the precise timing of whether changes in the freshwater flux occurred during the meltwater pulse.

3.2 Materials and Methods

3.2.1 ImageJ software

The first image processing method tested on X-radiographs taken from the studied cores was performed using an application called "*Plot lanes*" available in the software *ImageJ* (Schneider et al., 2012). This tool recognizes the brightness variation along an interval selected by the user on the images, generating a brightness curve. Thus, each concave-up along that curve means a lighter lamina corresponding with coarse-grained sediments, while each concave-down means a darker lamina corresponding with fine-grained sediments (Fig.3.2). Therefore, the number of concave-up and concave-down intervals along the curve represents the number of sandy laminae and muddy intervals present along the studied interval.

To understand the sensitiveness and limitations of the *ImageJ* method, the analyses were applied on images of interlaminated sediments having different resolutions: two intervals were selected from both cores CAGE-15 and IRIDYA-02 having 300 dpi image resolution, and one interval was selected from core GS-02 having only 72 dpi of resolution. The results obtained were also compared with the lightness curve generated by the multi-sensor core logger (MSCL) colour-scan as an additional product from the high-resolution digital photographs of the cores (Fig.3.2.1). On both image resolutions, the main peaks on the brightness curves, corresponding with the sandy layers, match very well with the peaks of the colour-scan curves, however, using the 300 dpi higher resolution (CAGE-15 and IRIDYA-02 cores), the *ImageJ* method was able to detect also the minor peaks associated with the fine-laminations in the mud intervals, which was checked by comparing the results with the colour-scan curve.

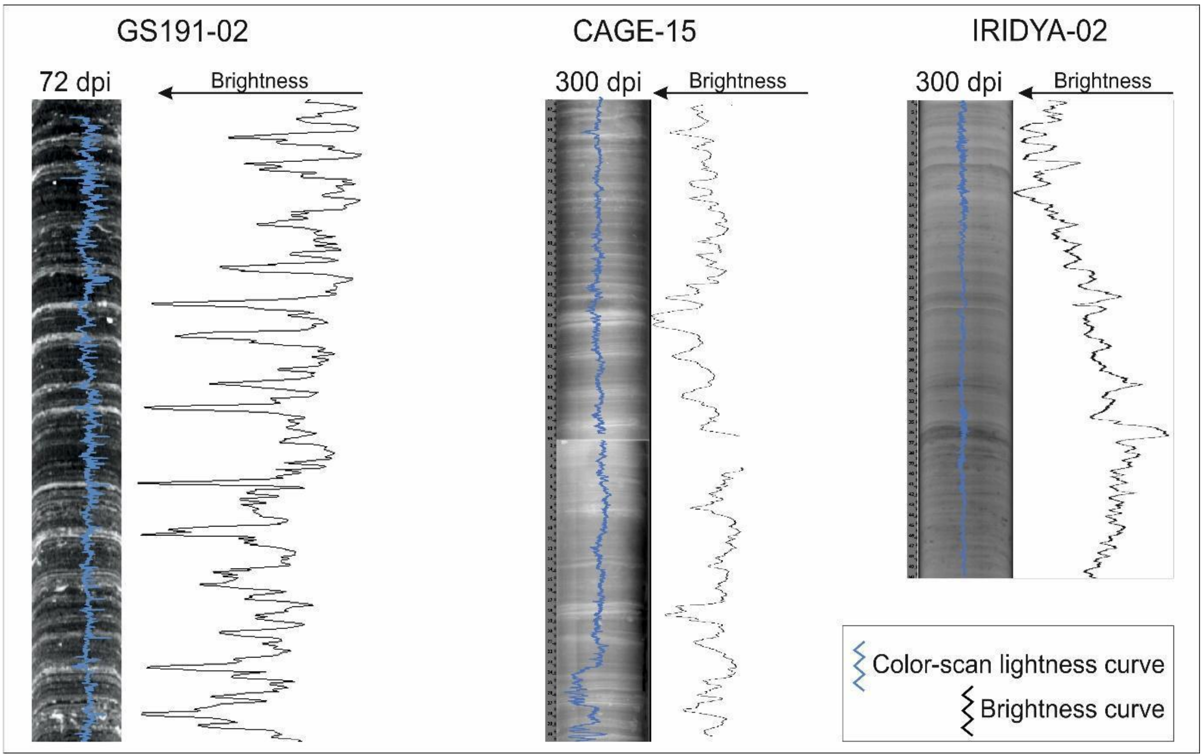

Figure 3.2.1: Plot lanes tool from Image J software applied on x-ray images of interlaminated sediments.

3.2.2 *BMPix method*

The second method that was tested to count and measure the laminations on sediment cores is the *Automated Tools for Layer Recognition (BMPix) and the Counting (PEAK tools)*, developed by (Weber et al., 2010). These two programs are used in conjunction with the Microsoft Excel to extract gray-scale values at the pixel resolution along a profile line fixed between adjustable end-points on the image. Such a method allows for quantitative evaluations of even small discrete transitions on the brightness curve of X-ray images. The *PEAK tools* application allows four different quantitative evaluations along the brightness curve: (1) minimum peaks, or very dark lamina, corresponding with mud intervals; (2) maximum peaks or very bright lamina, that corresponds with sandy layers; (3) positive slopes or rises, meaning the change from a finer material lamina to a coarser one; (4) negative slopes, or falls, which are the boundaries between a coarser to a finer lamina and *vice versa*. Even though the first two kinds of counting are overlapping and complementary, both evaluations were still performed on the designed cores intervals. Furthermore, during the lamina counting, the application automatically calculates the average thickness of themself laminae (Fig.3.2.2).

Parameters Of The Picture		Number Of Layers	187
x-Width [pix]	6336		
y-Width [pix]	552	Too Narrow	0
Depth At Start [cm]	1.3	Too Flat	339
Depth At End [cm]	98.9		
		Average Thickness Of Layers [cm]	0.519148936
Parameters Of The Measurement			
Start(x) [pix]	1		
End(x) [pix]	6336		
Start(y) [pix]	166		
End(y) [pix]	166		
FWHM_Gauss(Max_Count):	2		
Minimum width(Max_Count):	1		
Minimum height(Max_Count):	0.02		

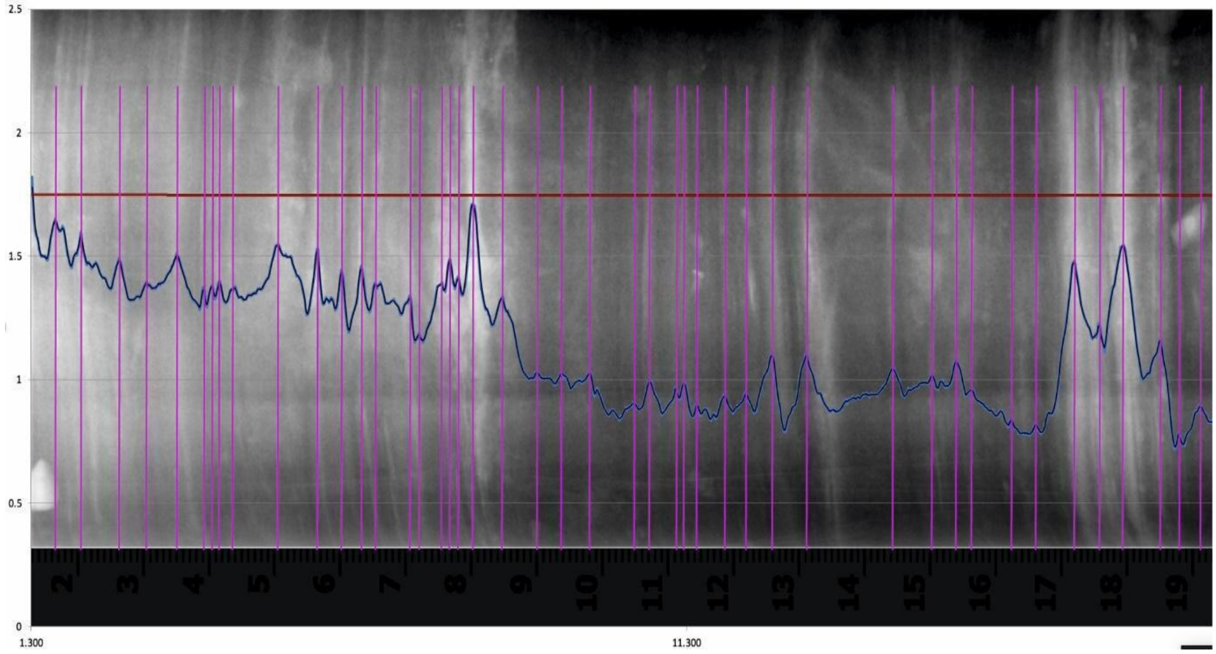

Figure 3.2.2: Example of the BMPix and PEAK tools quantitative evaluation of brightness peaks corresponding with sandy laminae and layers in core CAGE-15.

3.3 Results

The record of the MWP-1A plumite recovered by the studied sediment cores is contained in more than one consecutive section at each core. Hence the analyses had to be performed separately in the X-ray image of each section, and the resulting numbers were combined later. On the core CAGE-15, the record of the MWP-1A occurs from 324 to 253 cm below sea-floor (cm bsf), being contained in two sections (sections 3 and 4). On core IRIDYA-02 the same event was found between 345 and 292 cm bsf (sections 3 and 4), and the core GS-02 contains the interlaminations of that event located between 396 to 284 cm bsf (sections 4 and 5). In the following, it is reported the detailed results obtained applying both methods.

2.3.1 ImageJ results

The *ImageJ* method was capable of recognizing the lightness variation between sand and silt laminae within the MWP-1A plumite, the laminae were counted, and trends of recurrences along the deposits were determined to outline internal depositional cyclicity. For the cores CAGE-15 and IRIDYA-02, images with 300 dpi resolution were used. The length of these particular plumite deposits vary from 71 cm in the core CAGE-15 to 53 cm in the core IRIDYA-02, due to the natural differences in the accumulation rates between these two cored sites.

In core CAGE-15 a total of 196 laminas (98 pairs of darker and brighter laminae) were counted. The average layering frequency is 2.74 Lamina per cm (L/m), with average thickness of 0.36 cm, and seven trends recognized (Table 3.2.1).

In core IRIDYA-02, only 125 laminae were identified, with 2.35 L/cm frequency and 0.42 cm of average thickness (Table 3.3.1). Along the core IRIDYA-02 brightness curve, three trends or tendencies, separated by a typing point, were identified respectively at 329 cm bsf, with a less abrupt change located between 304 and 300 cm (Fig. 3.3.1).

On the core GS-02, the record of the MWP-1A is longer than on the other cores, with a total of 112 cm. However, the image resolution available for this core was 72 dpi. In this case 148 laminae were recognized with 1.32 L/cm frequency, and 8 prominent trends at the bottom of the record while the upper part has a regular cyclicity without clear trends. The main peaks on the brightness curve match with the colour-scan curve, but colour-scan but the low image resolution did not allow the recognition of smaller peaks or trends associated with minor horizons along the interlaminated deposit.

ImageJ software	**GS-02**	**CAGE-15**	**IRIDYA-02**
MWP-1A length (cm)	112	71	53
Number of layers	340	196	125
Frequency (L/cm)	3.03	2.74	2.35
Average thickness (cm)	0.33	0.36	0.42

Table 3.3.1: Synthesis of the counting laminations results on the MWP-1A using the ImageJ method.

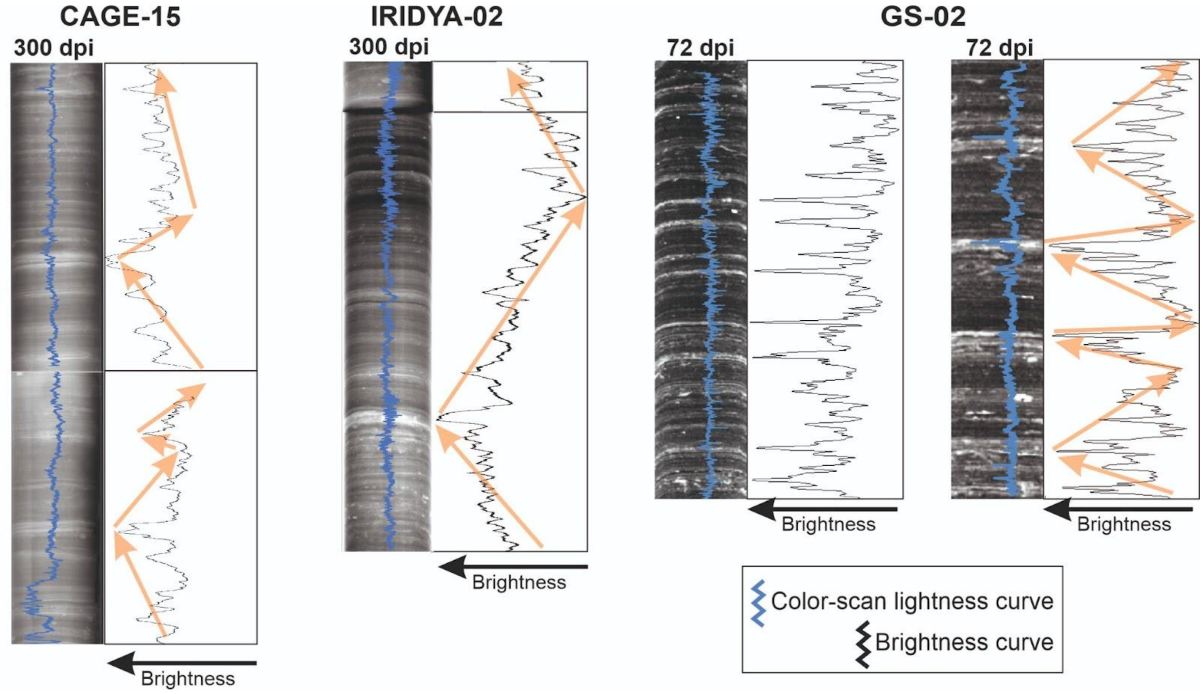

Figure 2.3.1: Brightness curve (black) and trends recognized (orange arrows) using ImageJ`s plot lanes tool, compared with the lightness curve (blue) from colour-scan along the MWP-1A intervals.

4.6.2 BMPIX results

Within the same 71 cm interval of the MWP-1A recovered in the core CAGE-15, the *BMPIX* and *Peak tools* were able to recognize a total of 320 laminae (160 pairs of darker and brighter laminae). The software measured an average thickness of 0.22 cm per lamina. Thus, the layering frequency along the entire interval is 4.50 L/cm. Although the frequency is fairly constant, there are two thin intervals with lower layer frequencies located between 274 – 276 and 302 – 307 cm bsf, reaching up to 3 L/cm, (Fig. 3.3.2) (Table 3.3.2).

On the core IRIDYA-02, the interval of this event is only 53 cm long, but contains the highest number of layers, totalizing with 224 pairs of darker and brighter laminae. The average thickness is considerably short (0.12 cm), with a higher frequency (8.45 L/cm). Two lower frequency intervals were also recognized on the record of the core IRDYA-02, respectively located between 300 – 304, and 328 – 330 cm bsf.

Although, the X-ray images available from the GS-02 core have a lower resolution (72 dpi) than the other cores (300 dpi), the analysis performed with BMPIX and Peak tools were capable to recognize and count 340 laminae (170 pairs of darker and brighter laminae) along the 112 cm interval associated with the record of the MWP-1A, having an average thickness of 0.33 cm, with a layering frequency of 3.03 L/cm. The values determined through BMPIX method are, therefore, exactly the same achieved with the imageJ software further outlining the problem related to low-resolution imaging.

BMPIX software	GS-02	CAGE-15	IRIDYA-02
MWP-1A length (cm)	112	71	53
Number of layers	340	320	448
Frequency (L/cm)	3.03	4.50	8.45
Average thickness (cm)	0.33	0.22	0.12
Lower frequency intervals	-----	274 – 276 305 - 307	328 - 330 300 - 304

Table 3.3.2: Synthesis of the counting laminations results on the MWP-1A using the BMPix method.

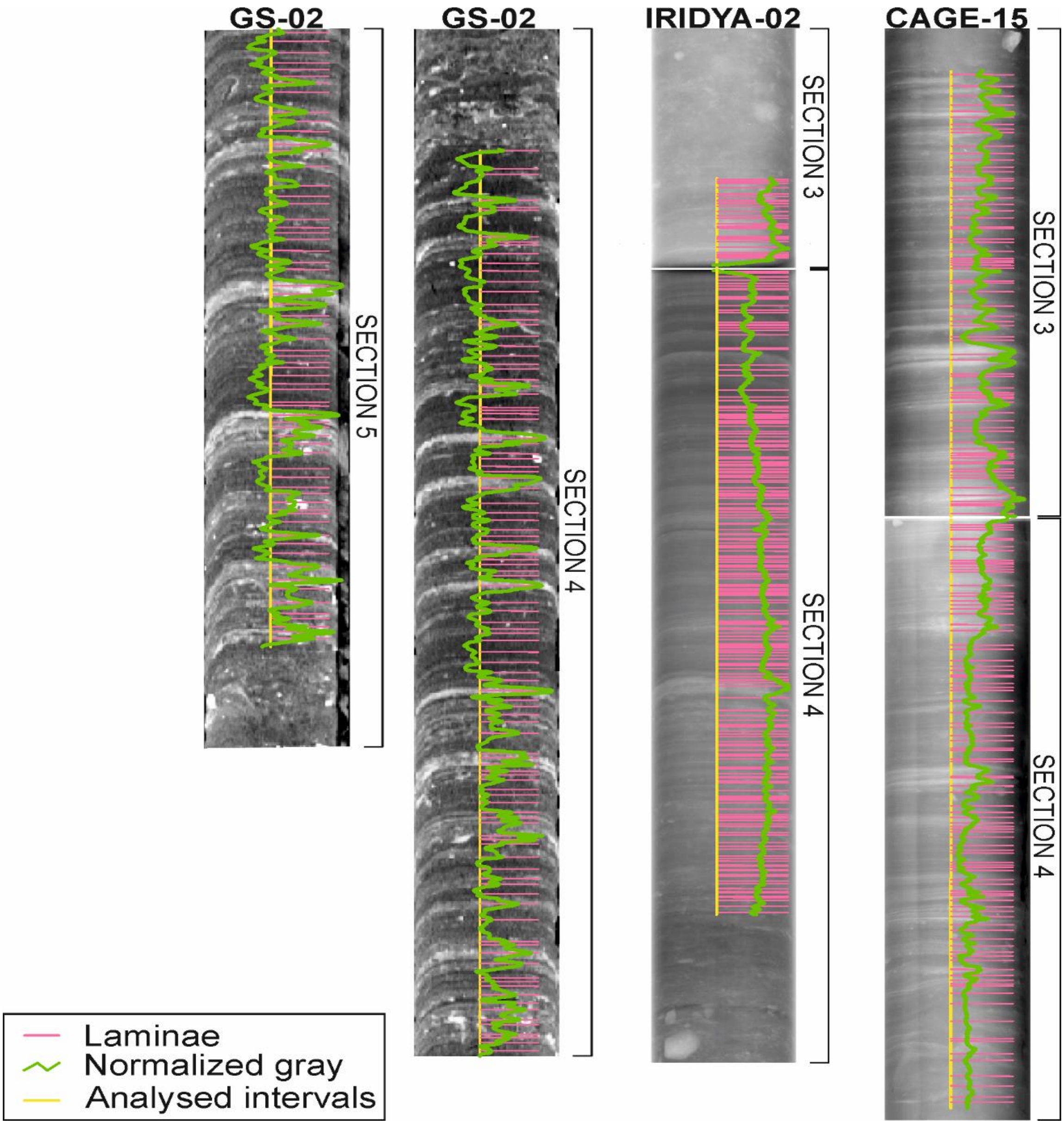

Figure 3.3.2: BMPIX and Peak tools measurement and count of laminations of the MWP-1A on the CAGE-15 and IRIDYA-02 cores. Orange horizontal line shows the analysed interval. Dark blue curve represents the Normalised grey recognized. Pinki vertical lines indicate layers recognized.

3.4 Discussion

Comparing the results obtained by *ImageJ* and *BMPIX* and *Peak tools*, both methods were capable of recognizing, counting and measuring the interlaminations associated with the plumite of the MWP-1A. Furthermore, both imaging processing techniques showed the limitations related to the X-ray image resolution. The relatively lower number of layers identified, and consecutively the lower frequency results obtained from the 72 dpi images of the core GS-02 indicate that this resolution is not suitable for the layer counting. The fact that both softwares determined the exact same index numbers, points to a common limitation. Therefore, this study suggests that 300 dpi resolution should be considered the minimum image resolution necessary to correctly apply this analytical method, although the 72 dpi images resolution are still useful to recognize trends/cyclicities along the grayscale profile that outline variations on the depositional process.

On the contrary, comparing the cores having 300 dpi images (IRIDYA-02 and CAGE-15), the total number of layers recognized are considerably different between the two methods because the ImageJ software recognized lower numbers in both cores. After a careful visual inspection of the X-ray data and the resulting lightness curves, it became clear that the *BMPIX* and *Peak tools* method is indeed more sensitive than the ImageJ method. Although this result was already expected, as the former is a program that was specifically developed to investigate laminated sedimentary records. However, as it is a relatively new method, it is worth carrying out tests that can be compared with other ways of analysing the same dataset.

Considering only the *BMPIX* results, a total of 448 laminae were recognized along the MWP-1A deposit recovered in core IRIDYA-02, indicating a total of 128 more laminas than those measured in the core CAGE-15 (Table 3.3.2). This difference is thought to be related to the position of the cored sites with respect to the efflux point of meltwaters (location of the ice stream terminus). The sedimentation related to meltwater plume deposition is characterised by a rapid seaward decay of sediments dispersion that is confined within a few tens of kilometres from the efflux point (Hesse et al., 1997; Lucchi et al., 2002, 2013). The significant difference in layering numbers between the two sampled sites is clear evidence that the ice-front of the Storfjorden ice stream feeding the Bellsund Drift, where IRIDYA-02 is located, persisted for a longer period close to the sampled site with respect to the ice-front of the Bellsund ice stream that fed the Isfjorden Drift, hosting site GAGE-15. The Storfjorden ice-stream, which had a much larger catchment area than the Bellsund's, with about 82,500 km^2 in the NW Barents Sea (Ottesen et al., 2005; Andreassen et al, 2008; Pedrosa et al., 2011) persisted close to the shelf break releasing turbid meltwaters for a longer time, while the Bellsund and Isfjorden ice-streams had already retreated into the shelf allowing deposition of plumites mainly on the outer continental shelf but not on the slope where CAGE-15 site is located.

A fundamental aspect that should be considered when working with such kind of analysis is the age control of the sedimentary record, specially at continental slopes, where sedimentation rates can change dramatically in a very short time of period due to abrupt behaviour of climate shifts. In this study, the AMS radiocarbon dating was performed as close as possible to the top and bottom boundaries of the plumite deposits in the core CAGE-15. Therefore, its age-depth model is accurate enough to consider a specific sediment acc.rate for the MWP. Hence, layering thickness and frequencies obtained from X-ray image processing were analysed not only with respect of depth bsf, but also in time-scale.

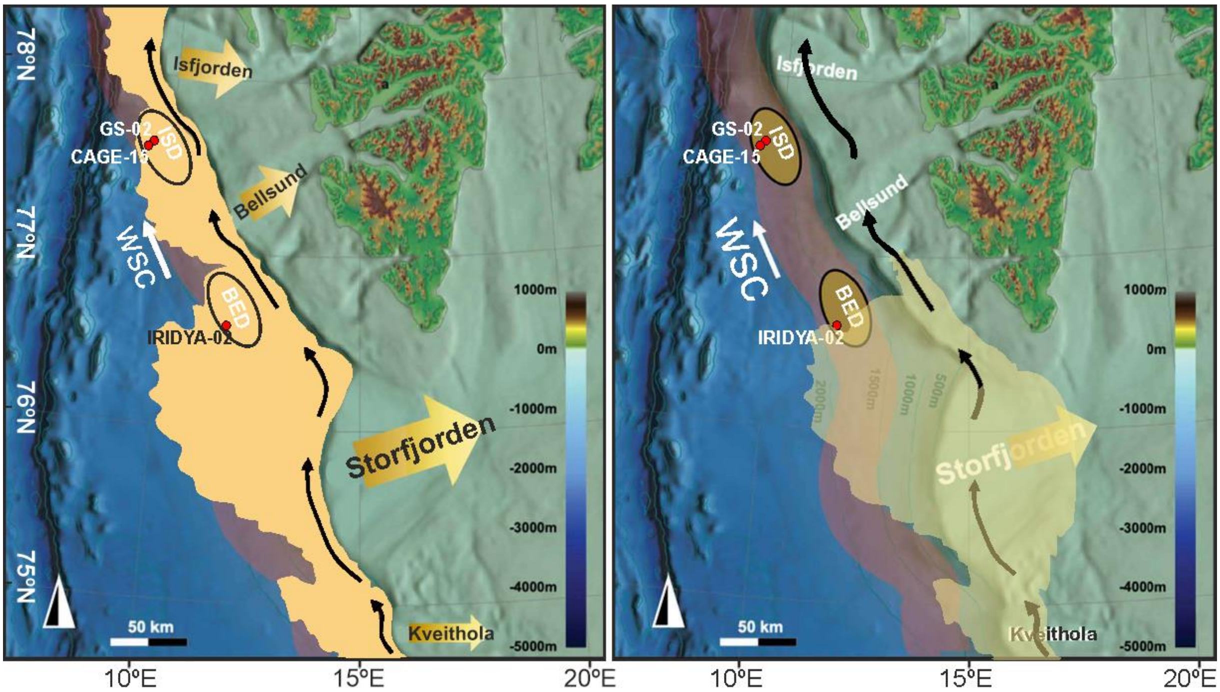

Figure 3.4.1: Image modified from Lucchi et al., (2023). Larger golden arrows indicate advances and retreats of ice streams. Thin black arrows indicate depositional processes contributing sediments to contourite depositional system deposit, BED = Bellsund drift, ISD = Isfjorden drift, WSC = West Spitsbergen Current.

The best information that can be extracted from the layering frequencies is based on the inversely proportional relationship between layering frequency and acc. rates. The maximum frequency found between 286 and 284 of plumites of core CAGE-15 are probably related to a period with a relatively lower meltwater release occurring at 14.24 cal ky BP. On the other hand, the two intervals with minimal frequencies located between 307 – 305 and 274 – 276 cm bsf are clear indications of episodes with higher sedimentation rates, which can be interpreted as periods of maximum meltwater fluxes occurred during the MWP-1A event. According to the age-depth model those levels would have occurred at 14.408 and 14.156 cal ky BP (Fig. 3.4.1). Additionally, two lower frequency intervals were observed also along the IRIDYA-02 record, located between 330 – 328 cm bsf, and between 304 – 300 cm bsf, coinciding with the levels where the brightness curves from the *ImageJ* software shifts its tendencies due to tipping points (Fig. 2.3.1). The two detected intervals of maximum sedimentation rate could have occurred at the same time at the two studied coring sites, indicating a main event impacting at a regional scale. However, a large number of age-dated levels on the IRIDYA-02 would be necessary to comprove the correlation and the hypothesis of simultaneity.

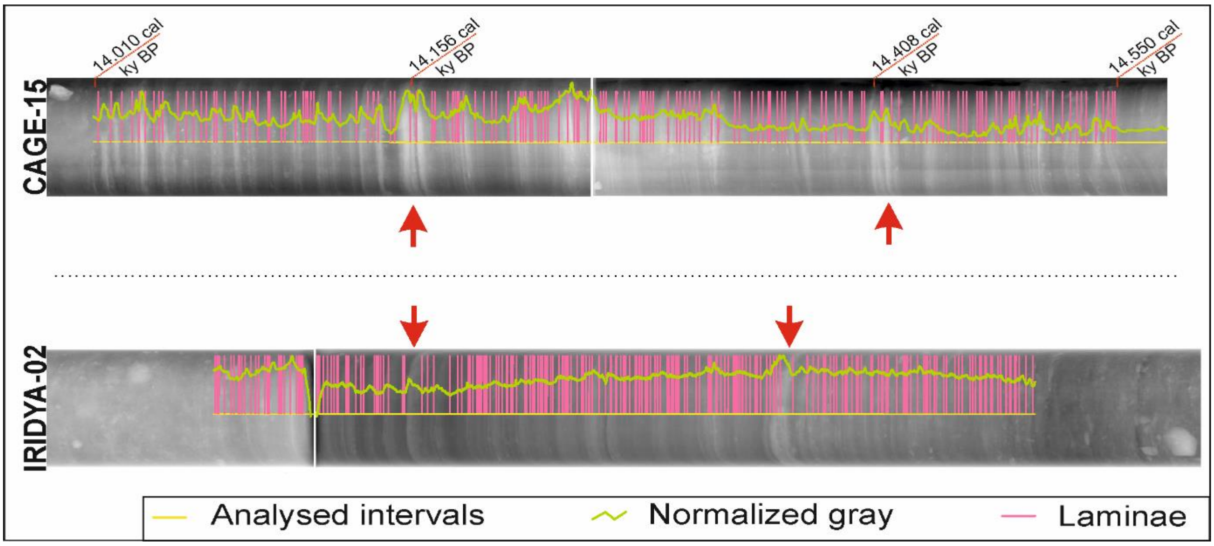

Figure 3.4.2: X-ray images processed with BMPIX. Red arrows indicate the intervals with lower layering frequencies on the cores. Age-dates obtained with Bayesian statistics explained in Chapter 1.

Since the average layering frequency identified with *BMPIX* and *Peak tools* method was 4.50 L/cm, and the average acc.rate of 8.2 years/cm along the MWP-1A was obtained from the Bayesian age-depth model build for the core (Fig 4.5A), it became possible to calculate in how much time, on average, each layer was deposited. The combination of those completely different kinds of data (age-depth model and layer recognition) indicate that each lamina would have been deposited within 1.70 years on average. Consequently, each pair of laminae represents 3.40 years. However, as both the raw radiocarbon dates obtained at the top and bottom boundaries of the MWP-1A plumite, and the calibration ΔR applied to the raw data during the age-calibration process have their own standard deviations (Table 1.3.1), both uncertainties had to be considered and distributed for each lamina using a geometric mean. Therefore, the calculated 1.70 years/Layer would have a ± 1.38 deviation, which lead to maximum and minimum time intervals of 3.08 and 0.32 years, respectively. Hence, each layer could represent one season, one, two or even two years. Such uncertainty is considerably large in comparison to the measured value, unfortunately limiting a confident interpretation.

To solve the problem, it would be necessary to improve the age model by dating additional levels within the plumite deposit. However, as it was discussed in Chapter 2, MWP events are characterised by a massive detritic input through sediment laden meltwaters that a) dilute the presence of biogenic fraction within the sediments, and b) hamper the biologic primary productivity by reducing the sun light penetration in the upper part of the ocean column by the presence of abundant, dispersed sediments at the ocean surface. For those reasons foraminifera sampling for additional radiocarbon dating would require a large amount of sediments to be investigated.

III - General Discussions and Final Conclusions

Taking into consideration the different results obtained during this research, some key aspects related with the record of the MWPs and H-like events that occurred in the Arctic during the last glacial and glacial termination T1 were identified. Thus, in the following, a holistic view of the 3 Chapters is presented and compared with the previous knowledge on the paleoclimatic and paleoceanographic history of the Western margin of Svalbard over the last 28 thousand years, and its implications to the Northern Hemisphere climate.

The stratigraphic sequence assessed by the studied cores contains three different intervals of *plumite* deposits, which were correlated by (Caricchi et al., 2019) to the H2-like event, the MWP-$1A_0$, and the MWP-1A, using the core GS-02 for a paleomagnetic study. As introduced in Chapter 3, plumite deposition is naturally expected during glacial terminations (Lucchi et al., 2013), but that is simply not the case for the H2-like deposit, which took place during the glacial stage of the MIS-2. Thus, the oldest melting event assessed by this study is probably the most puzzling, and illustrates well how complex ice-sheet dynamics and feedbacks with climate can be during glacial-interglacial transitions, and its internal millennial scale climate shifts.

Part of the Heinrich (H) events complexity comes from a fundamental ambiguity related to the IRD signal on marine records. Episodes of massive ice rafting can occur during ice-sheet fast decay or growth , respectively triggered by the summer maximum, and summer minimum insolation predicted in the Milankovitch cycles (Heinrich, 1988). In both scenarios, the Earth's climate is considerably unstable due to mutual interaction between ocean-atmosphere-cryosphere. Actually, the H2 has been deeply debated since the revision of the CLIMAP project reconstruction for the LGM discussed by the EPILOG program and presented by (Mix et al., 2001). In that occasion a number of researchers came to a consensus that the LGM chronozone should start at 24 or 23 ky, specifically to not include the H2, exactly because the climate was not steady during such an event. However, years later, members of the same group compiled multiple ice volume reconstructions, and it became clear that most of the global icesheets were already near the maximum at 26.5 (Clark et al., 2009), and the H2 interval was entirely fitting in the LGM period.

Initially, the H events were described to occur in the Labrador Sea with an "armada" of icebergs coming from the Laurentide Ice-sheet via the Hudson Strait (Heinrich, 1988; Andrews and Tedesco, 1992; Bond et al., 1993), which is also the reason why I have been using the term "H-like" to refer to these episodes of IRD depositions next to Svalbard. Later, some of these events, including the H2, have been linked to the

Eurasian Ice Sheet complex using IRD petrographic provenance in the Irish Sea (Scourse et al., 2000), Sr-Nd fingerprints across the North Atlantic (Scourse et al., 2000), and meltwater signature on PF $\delta^{18}O$ from South Norwegian Sea (Lekens et al., 2006). Also, according to (Darby et al., 2002), the Eurasian icebergs discharges into the Arctic precedes the ones originating from the North America in the Labrador Sea by ~500 years, which agrees with an idea ventilated by (Hemming, 2004), about a small Relative Sea Level (RSL) rise derived from surges of another ice-sheet contributing as one of the trigger mechanism for the collapse of the ice stream across the Atlantic, at the Hudson Strait.

Indeed, more recent works that focused in the H2 event (and others H events) trigger mechanisms have recognized sea surface cooling starting a few centuries before the settling time of IRD layers at IODP sites 980 and 983 located Southwest of Iceland (Barker et al., 2015), indicating that the icebergs release were not the initial cause of the cooling, but have given a positive feedback for the stadial conditions by weakening the AMOC. Furthermore, transitions from Heinrich Stadials (HS) to Greenland Interstadials (GI) were described as commonly marked by large meltwater plumes and iceberg releases in the Fram Strait (Jessen et al., 2010; Müller and Stein, 2014; T. L. Rasmussen et al., 2014; Jessen and Rasmussen, 2019; El bani Altuna et al., 2024). Unequivocal evidence of such sediment plume were presented by Lucchi et al., (2013) for the transition from the Order Dryas Stadial (HS-1) to the Bolling warming (GS-0), but undisturbed sedimentological evidence for the previous stadial-interstadial transition are not very easily found along the Fram Strait. Due to grounded ice erosion over the continental shelf, and gravitational processes that includes Mass Transport Deposits (MTDs) or glaciogenic debris flows near the Storfjorden and the others TMFs (Laberg and Vorren, 1995; Vorren and Laberg, 1997; Dowdeswell et al., 2008; Laberg and Dowdeswell, 2016).

Nevertheless, MTDs physically disrupt and rework previously deposited sequences including the stratigraphical records associated with the period between 24 and 19 ky BP. For such a reason, most of the stratigraphic studies carried out in this region have focused on the late-deglacial phase (above the MTDs), specifically the Bølling warm period, the Younger Dryas stadial, and the onset of the Holocene warm period (e.g. (Hald et al., 2004, 2007; Werner, Robert F. Spielhagen, et al., 2013; T. L. Rasmussen et al., 2014; Carbonara et al., 2016; Rigual-Hernández et al., 2017; Nielsen and Rasmussen, 2018; Jang et al., 2021; Devendra et al., 2023).

To avoid the MTDs stratigraphic disruption associated to their emplacement, a few studies recovered continuous sequences at sites beyond the continental slope, in deeper areas of the Fram strait, been successful in recognize IRD layers associated with Heinrich events (hereafter called Heinrich-like event), and periods with high productive zones with high concentrations of foraminifera during the Weichselian period (Hebbeln, 1992; Hebbeln et al., 1994; Dokken and Hald, 1996). However, the exact onset and dynamics of H-like and MWP events, and the time between causes and responses of this complex cryosphere-ocean-atmosphere mechanism remained not completely understood. Furthermore, a smaller number of studies from this area have recovered continuous and expanded stratigraphic sequences containing MWP events records without MTDs disturbance during the LGM (e.g. Müller et al., (2009); Müller and Stein, (2014); Caricchi et al., (2019); (2020).

To this debate, the present thesis added the multi-proxy high-resolution evidence from sites not affected by MTDs, that was presented in Chapter 2. The results clearly showed periods of reactivation of the WSC during the LGM and termination T1. The WSC carried heat from the North Atlantic to the Barents Sea and Svalbard and caused sea-ice free conditions generating a regional-scale polynya responsible for deepwater formation that ventilated the deep ocean and fed the AMOC. The presence of the benthic foraminifera *C. wuellerstorfi*, during foraminiferal blooms at the polynya is clear evidence of active strong bottom currents moving along the western continental slope of Svalbard. Except for these intervals, such benthic species was found only within the heavily bioturbated sediments of the Holocene period found at the topmost part of the studied cores, and more generally, topping the upper part of the stratigraphic sequence in this area.

Those findings are in good agreement with previous studies that recognized the presence of polynya activities in the southern and northern part of the western margin of Svalbard and in the Fram Strait (Müller et al., 2009; J. Müller and Stein, 2014; Knies et al., 2018). The reactivation of the WSC immediately after the LGM has delivered enough heat to destabilize the ice-sheet but its effect was stopped by a strong negative feed-back generated by the meltwater release inducing ocean stratification and sea-ice formation which, in turn, led to a new cold environment, as illustrated step by step in Chapter 2. At the same time, the new chronology discussed in Chapter 1 allowed for the comparison with other paleoclimate records and revealed a strong temporal correlation between the H2-like plumite deposit recovered in the studied cores but also along the whole margin (e.g. Plaza-Faverola et al., (2023) with the Greenland Interglacial GI-2 (S.O. Rasmussen et al., 2014) therefore to a warm atmospheric period. The present study demonstrated the occurrence of warm interstadials during the glacial stage MIS-2, with AMOC reactivation increasing the amount of heat delivered to the SBSIS. The negative feedback associated with meltwater release and ocean stratification led to a gradual readvance of the ice sheet indicated by the cooling tendency recorded on the $\delta^{18}O$ until a tipping point recorded at the base of the MWP-$1A_0$, that can be seen on curves presented on depth and time-scale for the core CAGE-15, on Fig. 2.3.7 and Fig. 2.3.9. The MWP-$1A_0$ marks the beginning of last glacial termination T1.

The age-depth models built along this research, points to a later onset for both the H2-like and the MWP-$1A_0$ events, starting at 23.44 and 18.44 cal ky BP respectively. Comparing these ages with the ones defined by (Caricchi et al., 2019), the events were 1.54 and 1.33 ky younger than initially thought. The original data implementation with

2 recently made calibration curves to calculate a variable ΔR effect is the main explanation for such differences. It is also possible that those events can be correlated with the plumite depositions with high IRD content recovered in the Southern Norwegian Sea, described to be deposited at 21.5 and 18.6 cal ky BP by (Lekens et al., 2005). It is possible that those events were the H2-like and MWP-1A0.

Based on that, it seems that a very similar ocean-cryosphere mechanism would have triggered the collapses of the SBSIS during all three plumite deposition episodes here recorded (H2-like, MWP-1A$_0$, MWP-1A). Comparing the case of the H2-like with the other events, the cooling feedback on sea-surface temperature would have lasted for a much longer period due to minimal summer insolation at 65N occurring ~22 ky BP (Laskar, 2006). While widespread sea-ice covering contributed to increase the Albedo, which was already very high due to huge continental ice masses over the Northern Hemisphere (Clark and Mix, 2002).

The data presented in this study highlighted a significantly large difference between the MWP-1A$_0$ and MWP-1A depositional contributions from the SBSIS. Even though the icefront was probably reaching a more distal position during the first event, right after the LGM period (Clark et al., 2009), the interlaminated deposit of the second event is always thicker on the studied cores. On the shallowest site (GS-02), the MWP-1A plumite interval is 20% longer than MWA-1A$_0$, while in the deepest site (IRIDYA-02) the deposit is ten times thicker (Table 2.1.3). Even though the plumites areal distribution is considered to be limited to a few tens of kilometers (Hesse et al., 1997; (Lucchi et al., 2013), the hypo and hyperpycnal formed by the second event clearly covered a much larger area along the margin, and delivered a greater amount of sediments to the slope region of the Svalbard margin. This would suggest a more local origin of the MWP-1A$_0$ event, possibly associated with the deeply grounded ice streams, whereas the MWP-1A had a more regional impact affecting the whole margin.

According to current knowledge, the MWP-1A occurred during just ~340 years, between 14.65 and 14.31 cal ky BP (Deschamps et al., 2012), and 20–35% of the ice volume would have been released by the Eurasian ice complex (Lin et al., 2021). Previous investigations that also used age-dating on the MWP-1A record from the Barents and Baltic Seas has indicated 14.7 and 14.6 cal ky BP as the starting age (Rinterknecht et al., 2006; Lucchi et al., 2013). Therefore, the chronology presented here for this event (14.55 – 14.01 cal Ky BP) is considered in very good agreement with those previous works. The 100 years late start, and 300 years late termination recorded in the core CAGE-15 are entirely, or almost entirely covered by the respectively 230 and 250 years of standard deviation on the AMS ^{14}C raw data.

Another original contribution from this thesis that increased our knowledge on the emplacement and evolution of the Late-Quaternary MWPs is the use of automatic layering recognition applied to Northern high-latitudes plumite deposits. The computational program developed and tested by (Weber et al., 2010) in the sedimentary records from Antarctica was applied in the Arctic for the first time during this research. The autonomous measurements recognized two thin intervals with lower interlaminations frequencies due to episodes of maximum accumulation rates during the settling of the MWP-1A as recorded in cores CAGE-15 and IRIDYA-02. The age-depth model indicates those episodes were probably centered at 14.156 and 14.408 cal ky BP, lasting for no more than a few years, since the average acc.rate for the event is 8.2 yr/cm. Furthermore, despite the lamina counting tests made using the ImageJ program on X-radiographs had recognized an unrealistic number of layers, this software interface resulted to be particularly successful in identifying general trends or tendencies along the plumite record. Actually, the tipping points identified along the ImageJ curve strongly agree with the intervals characterized by lower interlamination frequencies intervals, which can be considered a second confirmation of those maximum depositional episodes within the MWP-1A.

The combination of those results and interpretations presented add completely new information about the internal dynamics of the MWP-1A event, increasing the knowledge on this major event. Such kind of analysis will be repeated in a near future on new recently taken X-radiographs of the core GS-02 using 300 dpi resolution, and other cores collected along the margin during previous research projects involving the OGS together with Italian and International partners, in order to fully investigate also the MWP-1A0 and the H2-like records both present along the margin.

This research also recognized the stratigraphic signal related to the H1-like event, which emplacement is marked by an oxidized layer (Ox-2) of a few to several centimeters thick. The H1-like sediments are characterized by an increased concentration of IRD without interlaminations. The two peaks along the IRD flux curve are in very good agreement with the idea of two separated phases for this event (H1a and H1b), as described by Bard et al., (2000) and (Clark et al., 2009). In core CAGE-15, those phases were dated respectively at ~16.27 and 15.72 cal ky BP. The sedimentary record of the H1-like suggests increasing calving, delivering an “armada” of icebergs released along the margin during about 500 years. This record cannot be recognized in all cores representing a more restricted event like the MWP-1A$_0$.

Finally, the Younger Dryas, also known as H0 event, was identified in the cores just by a thinner oxidized level (Ox-1) pointing to a much smaller event, in comparison to the previous, older events described. That event was also identified by Lucchi et al., (2013) and Carbonara et al., (2016) along this region. Any clear evidence of the MWP-1B (11.5-11.0 cal ky BP) or the MWP-1C (about 8 cal ky BP) was identified on the studied core. This lack of evidence on the slope clearly indicates the paleo SBSIS was already fairly retreated on the continental shelf so any meltwater plume could reach the continental slope depositing the typical interlaminated facies.

IV- Outlooks and future possibilities for this research

During the course of this doctoral research, a few unexpected findings caused changes on the methodologies applied to the research. Originally, all three cores would have been quantitatively analyzed for the micropaleontological content using a 10-cm sampling spacing. However, after analyzing the first 67 samples of core CAGE-15, the large variation on the Planktonic Foraminiferal abundance and distribution within the LGM was evident. Thus, in order to better investigate such an unexpected and intriguing finding, a second sampling party was performed applying the 1-cm resolution to the core. By doing that, the oceanographical trigger mechanisms of the MWP and H-like events were revealed, and we could age-date them. Even though each one of the additional 234 fresh samples required ~4 hours of laboratory work, I personally considered that work fulfilling the targets of the thesis research plan and would appreciate to have more time and expand the 1-cm resolution sampled towards the core top, or doing the same investigation along the core IRIDYA-02 to testify the regional significance of this study. Hence, that would be one of the possible future works for the study area, which I would really like to have the chance to do in the future.

One of the difficulties found during this study was the extremely low numbers of foraminiferal content within the melting events. That increased the errors of the ^{14}C results, because it was necessary to put together the planktonic foraminifera picked from 2 or 3 successive samples to reach the required minimum amount of Carbon necessary to perform the AMS analyses. As only the working-half of the cores can be sampled and some material must be kept intact for other analysis, the sediments used during this study represented only a ¼ slice of the horizontal section of the core. Therefore, for future studies on this matter, I suggest the use of the entire slice available on the working-half, specifically for the bottom and top limits of the plumite deposits, in order to reach a bigger number of planktonic foraminifera to reduce the ^{14}C raw errors to a decadal scale.

A very recommendable continuation of what was started during this doctoral study is to replicate the interlamination recognition using 300 dpi resolution X-ray images of the core GS-02, because it contains an expanded stratigraphic sequence. Also, it would be interesting to extend the lamina counting on the record of the MWP-1A_0 that contrary to the other cores investigated, in core GS-02 appear very well developed and almost unique along the margin, and possibly hiding new interesting information on the paleo SBSIS dynamic at the inception of last deglaciation.

Acknowledgements

By the end of this doctoral course, I am grateful to many people, but I must start by thanking my life partner and beloved Julia, who encouraged me in every single step of this long journey with infinite support and patience. Together, we move to Italy in the middle of a pandemic, having no idea of how hard and complicated it would be. I am sure that without her I would never have made it. I want to thank my family in Brazil, especially my parents and brothers, who gave me the skills to be someone capable of going around the world without fear. Also, my grandparents, who had left this world before I finished this stage of my life but remained vivid in my consciousness.

I would like to thank my supervisor, professor Monica Bini, who agreed to supervise me and was always very supportive. My co-supervisor, Dr. Renata G. Lucchi, encouraged me to write the PhD project, and followed my entire journey. I also want to thank the professor Caterina Morigi, who introduced me to micropaleontology, and welcomed me in the laboratory where I always felt happy to be in. For these three incredible women, I will always cherish a deep feeling of gratitude and respect because they consistently guided me to go forward with the research. They always encouraged me to attend conferences, workshops and summer school that greatly enriched my doctorate experience. Furthermore, as a foreign student, I had to deal with complex bureaucratic situations during my first year in Italy, and they helped me on a number of occasions on that matter.

I'm absolutely grateful for all my colleagues, from the Earth Science Department of the University of Pisa, who quickly became my friends, taught me the language and shared the rich culture of this beautiful country, and other countries too, once there were people from many other places in the same office. I`m also grateful to the professors, and workers of the department, who were always so nice to me while I was there.

Also, I would like to thank the University of Florence for the PhD grant that I received, during the 37th PhD cycle in Earth Sciences, within the *Dottorato Regionale Toscano*. The PRA-IRIDYA project (PRA2021-0012) for all the technical and financial support. The Instituto Nazionale di Oceanografia e Geofisica Sperimentale (OGS) and the University of Trieste for the laboratory facilities and technical support during the analyses. The University of Cambridge for the support during the age calibration and modeling performed in the Geography Department of the Downing College under the guidance of Dr Marco Aquino Lopez and the professor Dr. Francesco Muschitiello. The University and CSIC of Barcelona, and ENI-Italy respectively for the XRF-core scan, MSCL and X-radiographs on core GS-02.

Finally, I acknowledge the participants, officers, and crews of the expeditions Eurofleets2-PREPARED on the RV G.O. Sars, CAGE 19-3KH of RV Kronprins Haakon, and the RV Laura Bassi Arctic Expedition 2021. Without their hard work, this research would not be possible.

References

Aagaard, K. and Carmack, E.C. (1989) ‘The Role of Sea Ice and Other Fresh Water in the Arctic Circulation’, *Journal of Geophysical Research*, 94(1), pp. 14485–14498. Available at: https://doi.org/10.1021/jp0010379.

Aagaard, K. and Coachman, L.K. (1968) ‘The East Greenland Current North of Denmark Strait: Part II’, *Arctic*, 21(464), pp. 267–290. Available at: http://citeseerx.ist.psu.edu/viewdoc/summary?doi=10.1.1.490.2616.

Agnihotri, R. et al. (2008) ‘Subdecadally resolved paleoceanography of the Peru margin during the last two millennia’, *Geochemistry, Geophysics, Geosystems*, 9(5). Available at: https://doi.org/10.1029/2007GC001744.

Alley, R.B. et al. (1997) ‘Holocene climatic instability: A prominent, widespread event 8200 yr ago’, *Geology*, 25(6), pp. 483–486. Available at: https://doi.org/10.1130/0091-7613(1997)025<0483:HCIAPW>2.3.CO;2.

Alley, R.B. et al. (2005) ‘Ice-sheet and sea-level changes’, *Science*, 310(5747), pp. 456–460. Available at: https://doi.org/10.1126/science.1114613.

Andersen, K.K. et al. (2004) ‘High-resolution record of Northern Hemisphere climate extending into the last interglacial period’, *Nature*, 431(7005), pp. 147–151. Available at: https://doi.org/10.1038/nature02805.

Anderson, E.C. et al. (1947) ‘Radiocarbon from cosmic radiation’, *Science*, 105(2735), p. 576. Available at: https://doi.org/10.1126/science.105.2735.576.

Andreassen, K., Laberg, J.S. and Vorren, T.O. (2008) ‘Seafloor geomorphology of the SW Barents Sea and its glaci-dynamic implications’, *Geomorphology*, pp. 157–177. Available at: https://doi.org/10.1016/j.geomorph.2007.02.050.

Andrews, J.T. and Tedesco, K. (1992) ‘Detrital carbonate-rich sediments, northwestern Labrador Sea: implications for ice-sheet dynamics and iceberg rafting (Heinrich) events in the North Atlantic’, *Geology*, 20(12), pp. 1087–1090. Available at: https://doi.org/10.1130/0091-7613(1992)020<1087:DCRSNL>2.3.CO;2.

Arrhenius, G. (1953) ‘Sediment cores from the east pacific’, *Geologiska Föreningen i Stockholm Förhandlingar*, 75(1), pp. 115–118. Available at: https://doi.org/10.1080/11035895309454862.

Baeten, N. et al. (2014) ‘Journal of Geophysical Research : Earth Surface’, *Journal of Geophysical Research: Earth Surface*, (119), pp. 2335–2360. Available at: https://doi.org/10.1002/2013JF002871.Received.

El bani Altuna, N. et al. (2024) ‘Sea ice-ocean coupling during Heinrich Stadials in the Atlantic–Arctic gateway’, *Scientific Reports*, 14(1), pp. 1–12. Available at: https://doi.org/10.1038/s41598-024-51532-7.

Bard, E. et al. (1990) ‘Calibration of the 14C timescale over the past 30,000 years using mass spectrometric U-Th ages from Barbados corasl’, *Nat*, 345, pp. 405–410.

Bard, E. et al. (1996) ‘Deglacial sea-level record from Tahiti corals and the timing of meltwater discharge’, *Nature*, 382, pp. 241–244.

Bard, E. et al. (2000) 'Hydrological impact of Heinrich events in the subtropical Northeast Atlantic', *Science*, 289(5483), pp. 1321–1324. Available at: https://doi.org/10.1126/science.289.5483.1321.

Bard, E., Hamelin, B. and Delanghe-Sabatier, D. (2010) 'Deglacial meltwater pulse 1B and younger dryas sea levels revisited with boreholes at tahiti', *Science*, pp. 1235–1237. Available at: https://doi.org/10.1126/science.1180557.

Bard, E., Rostek, F. and Ménot-Combes, G. (2004) 'Radiocarbon calibration beyond 20,000 14C yr B.P. by means of planktonic foraminifera of the Iberian Margin', *Quaternary Research*, 61(2), pp. 204–214. Available at: https://doi.org/10.1016/j.yqres.2003.11.006.

Barker, S. et al. (2015) 'Icebergs not the trigger for North Atlantic cold events', *Nature*, 520(7547), pp. 333–336. Available at: https://doi.org/10.1038/nature14330.

Bassett, S.E. et al. (2005) 'Ice Sheet and Solid EarthInfluences on Far-FieldSea-Level Histories', *SCIENCE*, 309, pp. 925–929. Available at: https://doi.org/10.1029/2002gl016722.

Bellwald, B. et al. (2020) 'Meltwater sediment transport as the dominating process in mid-latitude trough mouth fan formation', *Nature Communications*, 11(1), pp. 1–10. Available at: https://doi.org/10.1038/s41467-020-18337-4.

Bender, M. et al. (1994) 'Climate correlations between Greenland and Antarctica during the past 100,000 years', *Nature*, pp. 663–666. Available at: https://doi.org/10.1038/372663a0.

Bensi, M. et al. (2019) 'Deep flow variability offshore south-west Svalbard (fram strait)', *Water (Switzerland)*, 11(4), pp. 1–21. Available at: https://doi.org/10.3390/w11040683.

Bentley, M.J. et al. (2010) 'Deglacial history of the West Antarctic Ice Sheet in the Weddell Sea embayment: Constraints on past Ice volume change', *Geology*, 38(5), pp. 411–414. Available at: https://doi.org/10.1130/G30754.1.

Betts, A.K. and Ball, J.H. (1997) 'Albedo over the boreal forest', *Journal of Geophysical Research*, 102(96), pp. 901–909. Available at: https://doi.org/doi:10.1029/96JD03876.

Bird, M.I. et al. (2010) 'Punctuated eustatic sea-level rise in the early mid-Holocene', *Geology*, 38(9), pp. 803–806. Available at: https://doi.org/10.1130/G31066.1.

Blaauw, M. and Christen, J.A. (2011) 'Flexible paleoclimate age-depth models using an autoregressive gamma process', *Bayesian Analysis*, 6(3), pp. 457–474. Available at: https://doi.org/10.1214/11-ba618.

Blanchon, P. (2011) 'MELTWATER PULSES', in *Encyclopedia of Modern Coral Reefs*, pp. 683–690. Available at: https://doi.org/10.1016/S0012.

Blanchon, P. and Shaw, J. (1995) 'Reef drowning during the last deglaciation: Evidence for catastrophic sea-level rise and ice-sheet collapse', *Geology*, 23, pp. 4–8. Available at: https://doi.org/10.1016/B978-0-323-60984-5.00062-7.

Bond, G. et al. (1993) 'Correlations between climate records from North Atlantic sediments and Greenland ice', *Nature*, 365, pp. 143–147.

Boyd, T. and D’Asaro, E. (1994) ‘Cooling of the West Spitsbergen Current Wintertime Observations West of Svalbard’, *Journal of Geophysical Research*, 99, pp. 22597–22618. Available at: https://doi.org/10.1016/j.dsr.2015.06.003.

Boyd, T. and D`Asaro, E. (1994) ‘Cooling of the West Spitsbergen Current : Wintertime Observations West of Svalbard’, (November), p. 1994. Available at: https://doi.org/10.1029/94JC01824.

Brendryen, J. et al. (2020) ‘Eurasian Ice Sheet collapse was a major source of Meltwater Pulse 1A 14,600 years ago’, *Nature Geoscience*, 13(5), pp. 363–368. Available at: https://doi.org/10.1038/s41561-020-0567-4.

Broecker, W.S. (1982) ‘Glacial to interglacial changes in ocean chemistry’, *Progress in Oceanography*, 11(2), pp. 151–197. Available at: https://doi.org/10.1016/0079-6611(82)90007-6.

Broecker, W.S. et al. (2010) ‘Putting the Younger Dryas cold event into context’, *Quaternary Science Reviews*, pp. 1078–1081. Available at: https://doi.org/10.1016/j.quascirev.2010.02.019.

Broecker, W.S. (2013) ‘Radiocarbon’, *Treatise on Geochemistry: Second Edition*, 5, pp. 257–271. Available at: https://doi.org/10.1016/B978-0-08-095975-7.00409-5.

Buizert, C. et al. (2014) ‘Greenland temperature response to climate forcing during the last deglaciation’, *Science*, 345(6201), pp. 1177–1180. Available at: https://doi.org/10.1126/science.1254961.

Butt, F.A. et al. (2000) ‘Deciphering late cenozoic development of the western Svalbard Margin from ODP Site 986 results’, *Marine Geology*, 169(3–4), pp. 373–390. Available at: https://doi.org/10.1016/S0025-3227(00)00088-8.

Carbonara, K. et al. (2016) ‘Palaeoclimatic changes in Kveithola, Svalbard, during the Late Pleistocene deglaciation and Holocene: Evidences from microfossil and sedimentary records’, *Palaeogeography, Palaeoclimatology, Palaeoecology*, 463, pp. 136–149. Available at: https://doi.org/10.1016/j.palaeo.2016.10.003.

Caricchi, C. et al. (2019) ‘A High-Resolution Geomagnetic Relative Paleointensity Record From the Arctic Ocean Deep-Water Gateway Deposits During the Last 60 kyr’, *Geochemistry, Geophysics, Geosystems*, 20(5), pp. 2355–2377. Available at: https://doi.org/10.1029/2018GC007955.

Caricchi, C. et al. (2020) *A refined age calibrated paleosecular variation and relative paleointensity stack for the NW Barents Sea: Implication for geomagnetic field behavior during the Holocene*, *Quaternary Science Reviews*. Elsevier Ltd. Available at: https://doi.org/10.1016/j.quascirev.2019.106133.

Cayre, O. et al. (1999) ‘Paleoceanographic reconstructions from planktonic foraminifera off the Iberian Margin: Temperature, salinity, and Heinrich events’, *Paleoceanography*, 14(3), pp. 384–396. Available at: https://doi.org/10.1029/1998PA900027.

Cetto, P.H. et al. (2024) ‘MWP-1C and reef drowning: Morphological evidence along the eastern Brazilian margin’, *Marine Geology*, 469(February), p. 107243. Available at:

https://doi.org/10.1016/j.margeo.2024.107243.

Chappellaz, J. et al. (1997) ‘Changes in the atmospheric CH 4 gradient between Greenland and Antarctica during the Holocene’, *Journal of Geophysical Research*, 102(D13), pp. 15,987-15,997.

Chen, J. et al. (2006) ‘Zr/Rb ratio in the Chinese loess sequences and its implication for changes in the East Asian winter monsoon strength’, *Geochimica et Cosmochimica Acta*, 70(6), pp. 1471–1482. Available at: https://doi.org/10.1016/j.gca.2005.11.029.

Clark, P.U. et al. (1996) ‘Origin of the first global meltwater pulse following the last glacial maximum’, *Paleoceanography*, 11(5), pp. 563–577. Available at: https://doi.org/10.1029/96PA01419.

Clark, P.U. et al. (2002) ‘Sea-level fingerprinting as a direct test for the source of global meltwater pulse IA’, *Science*, 295(5564), pp. 2438–2441. Available at: https://doi.org/10.1126/science.1068797.

Clark, P.U. et al. (2004) ‘Rapid rise of sea level 19,000 years ago and its global implications’, *Science*, pp. 1141–1144. Available at: https://doi.org/10.1126/science.1094449.

Clark, Peter U. et al. (2009) ‘The Last Glacial Maximum’, *Science*, 325(5941), pp. 710–714. Available at: https://doi.org/10.1126/science.1172873.

Clark, P. U. *et al.* (2009) ‘The last glacial maximun’, *Science*, pp. 710–714. Available at: https://doi.org/10.1126/science.1172873.

Clark, P.U., Alley, R.B. and Pollard, D. (1999) ‘Northern Hemisphere Ice-Sheet Influences on Global Climate Change’, *Science*, 286(November), pp. 1104–1111. Available at: https://doi.org/doi:10.1126/science.286.5442.

Clark, P.U. and Mix, A.C. (2002) ‘Ice sheets and sea level of the Last Glacial Maximum’, *Quaternary Science Reviews*, 21(1–3), pp. 1–7. Available at: https://doi.org/10.1016/S0277-3791(01)00118-4.

Crocket, K.C. et al. (2011) ‘Persistent Nordic deep-water overflow to the glacial North Atlantic’, *Geology*, 39(6), pp. 515–518. Available at: https://doi.org/10.1130/G31677.1.

Croudace, I.W. et al. (2019) ‘Current perspectives on the capabilities of high resolution XRF core scanners’, *Quaternary International*, 514, pp. 5–15. Available at: https://doi.org/10.1016/j.quaint.2019.04.002.

Dansgaard, W. et al. (1993) ‘Evidence for general instability of past climate from a 250-kyr ice-core record’, *Nature*, 364(6434), pp. 218–220. Available at: https://doi.org/10.1038/364218a0.

Darby, D.A. et al. (2002) ‘Arctic ice export events and their potential impact on global climate during the late Pleistocene’, *Paleoceanography*, 17(2), pp. 15-1-15–17. Available at: https://doi.org/10.1029/2001pa000639.

De Geer, G., (1900). Om östra Spitsbergens glaciation under istiden. Geologiska Föreningens i Stockholm Förhandlingar 22, 427e436.

Denton, G.H. et al. (2010) ‘The last glacial termination’, *Science*, 328(5986), pp. 1652–1656. Available at: https://doi.org/10.1126/science.1184119.

Deschamps, P. et al. (2012) ‘Ice-sheet collapse and sea-level rise at the Bølling warming 14,600 years ago’, *Nature*, 483(7391), pp. 559–564. Available at: https://doi.org/10.1038/nature10902.

Devendra, D. et al. (2023) ‘The development of ocean currents and the response of the cryosphere on the Southwest Svalbard shelf over the Holocene’, *Global and Planetary Change*, 228. Available at: https://doi.org/10.1016/j.gloplacha.2023.104213.

Dimakis, P. et al. (2000) ‘Submarine slope stability on high-latitude glaciated Svalbard-Barents Sea margin’, *Marine Geology*, 162(2–4), pp. 303–316. Available at: https://doi.org/10.1016/S0025-3227(99)00076-6.

Dokken, T.M. and Hald, M. (1996) ‘Rapid climatic shifts during isotope stages 2-4 in the Polar North Atlantic’, *Geology*, 24(7), pp. 599–602. Available at: https://doi.org/10.1130/0091-7613(1996)024<0599:RCSDIS>2.3.CO;2.

Douss, N. (2023) '*Interplay of bottom currents and glacial input on western margin of the Svalbard: evidence from giant piston cores spanning the last 90 ka'. Available at: https://arts.units.it/handle/11368/3059808.*

Dowdeswell, J.A. et al. (2008) ‘A major trough-mouth fan on the continental margin of the Bellingshausen Sea, West Antarctica: The Belgica Fan’, *Marine Geology*, 252(3–4), pp. 129–140. Available at: https://doi.org/10.1016/j.margeo.2008.03.017.

Duplessy, J.C. et al. (1988) ‘Deepwater source variations during the last climatic cycle and their impact on the global deepwater circulation’, *Paleoceanography*, 3(3), pp. 343–360. Available at: https://doi.org/10.1029/PA003i003p00343.

Duplessy, J.C., Moyes, J. and Pujol, C. (1980) ‘Deep water formation in the North Atlantic Ocean during the last ice age’, *Nature*, 286(5772), pp. 479–482. Available at: https://doi.org/10.1038/286479a0.

Dypvik, H. and Harris, N.B. (2001) ‘Geochemical facies analysis of fine-grained siliciclastics using Th/U, Zr/Rb and (Zr + Rb)/Sr ratios’, *Chemical Geology*, 181(1–4), pp. 131–146. Available at: https://doi.org/10.1016/S0009-2541(01)00278-9.

Edwards, R.L. *et al.* (1993) ‘A large drop in atmospheric 14C/12C and reduced melting in the Younger Dryas, documented with 230Th ages of corals’, *Science*, 260(5110), pp. 962–968. Available at: https://doi.org/10.1126/science.260.5110.962.

Elverhøi, A. *et al.* (1995) ‘Elverhoi_et_al_1995_Late_Quaternary_Sediment_Yield_from_.pdf’, *The Journal of Geology*, 103, pp. 1–17. Available at: https://doi.org/https://doi.org/10.1086/629718.

Emiliani, C. (1955) ‘Pleistocene temperatures’, *Journal of Geology*, 63(6), pp. 538–578. Available at: https://doi.org/doi:10.1086/626295.

EPICA community members (2004) ‘Eight glacial cycles from an Antarctic ice core EPICA community members*’, *Nature*, 429, pp. 623–628. Available at: www.nature.com/nature.

Ericson, D.B. (1953) *Sediments of the Atlantic Ocean*. New York City.

Fagel, N. et al. (2024) ‘Environmental significance of kaolinite variability over the last centuries in crater lake sediments from Central Mexico’, *Applied Clay Science*, 247(November 2023). Available at: https://doi.org/10.1016/j.clay.2023.107211.

Fairbanks, R. (1989) ‘A 17,000-years glacio -eustatic sea level record: Influence of glacial melting rates on the younger Dryas event and deep-ocean circulation’, *Nature*, (342), pp. 637–642.

Fairbanks, R.G. et al. (2005) ‘Radiocarbon calibration curve spanning 0 to 50,000 years BP based on paired 230Th/234U/238U and 14C dates on pristine corals’, *Quaternary Science Reviews*, 24(16–17), pp. 1781–1796. Available at: https://doi.org/10.1https://doi.org/10.1038/342637a0.

Faleide, J.I. et al. (1996) ‘Late Cenozoic evolution of the western Barents Sea-Svalbard continental margin’, *Global and Planetary Change*, 12(1–4), pp. 53–74. Available at: https://doi.org/10.1016/0921-8181(95)00012-7.

Fan, Y. et al. (2023) ‘Fan et al (2023) Southward shift of the Westerlies during Heinrich Event 2. Evidence from loess deposits in Central Asia.pdf’, *Palaeogeography, Palaeoclimatology, Palaeoecology*, 630(111815), pp. 1–10. Available at: https://doi.org/https://doi.org/10.1016/j.palaeo.2023.111.

Ferreira, J., Cachão, M. and González, R. (2008) ‘Reworked calcareous nannofossils as ocean dynamic tracers: The Guadiana shelf case study (SW Iberia)’, *Estuarine, Coastal and Shelf Science*, 79(1), pp. 59–70. Available at: https://doi.org/10.1016/j.ecss.2008.03.012.

Fredin, O. et al., (2012) 'Distribution of ice marginal moraines in NWRussia', Journal of Maps 8, 236–241. Available at: https://doi:10.1080/17445647.2012.708536.

Fuchs, A. and Leuenberger, M.C. (1996) ‘δ18O of atmospheric oxygen measured on the GRIP Ice Core Document Stratigraphic disturbances in the lowest 10% of the core’, *Geophysical Research Letters*, 23(9), pp. 1049–1052. Available at: https://doi.org/10.1029/96GL00588.

Gales, J. et al. (2019) ‘Processes influencing differences in arctic and antarctic trough mouth fan sedimentology’, *Geological Society Special Publication*, 475(1), pp. 203–221. Available at: https://doi.org/10.1144/SP475.7.

Golledge, N.R. et al. (2014) ‘Antarctic contribution to meltwater pulse 1A from reduced Southern Ocean overturning’, *Nature Communications*, 5. Available at: https://doi.org/10.1038/ncomms6107.

Golledge, N.R. et al. (2019) ‘Global environmental consequences of twenty-first-century ice-sheet melt’, *Nature*, 566(7742), pp. 65–72. Available at: https://doi.org/10.1038/s41586-019-0889-9.

Gordon, D.C. (1970) ‘Some studies on the distribution and composition of particulate organic carbon in the North Atlantic Ocean’, *Deep-Sea Research and Oceanographic Abstracts*, 17(2), pp. 233–243. Available at: https://doi.org/10.1016/0011-7471(70)90017-3.

Gornitz, V. (2007) *Sea-level curve since the Last Glacial Maximum from*, *NASA*.

Grootes, P.M. et al. (1993) 'Comparison of oxygen isotope records from the GISP2 and GRIP Greenland ice cores', *Nature*, 366(6455), pp. 552–554. Available at: https://doi.org/10.1038/366552a0.

Gruetzner, J. et al. (2022) 'A revised core-seismic integration in the Molloy Basin (ODP Site 909): Implications for the history of ice rafting and ocean circulation in the Atlantic-Arctic gateway', *Global and Planetary Change*, 215(June), p. 103876. Available at: https://doi.org/10.1016/j.gloplacha.2022.103876.

Hain, M.P., Sigman, D.M. and Haug, G.H. (2010) 'Carbon dioxide effects of Antarctic stratification , North Atlantic Intermediate Water formation , and Subantarctic nutrient drawdown during the last ice age : Diagnosis and synthesis ... Carbon dioxide effects of Antarctic stratification , North Atlantic', *Global Biogeochemical cycles*, 24(GB4023). Available at: https://doi.org/10.1029/2010GB003790.

Hald, M. et al. (2004) 'Holocene paleoceanography and glacial history of the West Spitsbergen area, Euro-Arctic margin', *Quaternary Science Reviews*, 23(20-22 SPEC. ISS.), pp. 2075–2088. Available at: https://doi.org/10.1016/j.quascirev.2004.08.006.

Hald, M. et al. (2007) 'Variations in temperature and extent of Atlantic Water in the northern North Atlantic during the Holocene', *Quaternary Science Reviews*, 26(25–28), pp. 3423–3440. Available at: https://doi.org/10.1016/j.quascirev.2007.10.005.

Hanebuth, T., Stattegger, K. and Bojanowski, A. (2008) 'Termination of the Last Glacial Maximum sea-level lowstand. The Sunda-Shelf data revisited.pdf', *Global and Planetary Change*, 66, pp. 79–84.

Hanebuth, T., Stattegger, K. and Grootes, P.M. (2000) 'Rapid flooding of the Sunda Shelf: A late-glacial sea-level record', *Science*, 288(5468), pp. 1033–1035. Available at: https://doi.org/10.1126/science.288.5468.1033.

Hansen, B. et al. (2004) 'Already the day after tomorrow?', *Science*, 305(5686), pp. 953–954. Available at: https://doi.org/10.1126/science.1100085.

Hansen, K.E. et al. (2022) 'Deglacial to Mid Holocene environmental conditions on the northeastern Greenland shelf, western Fram Strait', *Quaternary Science Reviews*. Available at: https://doi.org/10.1016/j.quascirev.2022.107704.

Harrison, S., Smith, D.E. and Glasser, N.F. (2019) 'Late Quaternary meltwater pulses and sea level change', *Journal of Quaternary Science*, 34(1), pp. 1–15. Available at: https://doi.org/10.1002/jqs.3070.

Hays, J.D., Imbrie, J. and Shackleton, N.J. (1976) 'Variations in the earth's orbit: Pacemaker of the ice ages', *Science*, 194(4270), pp. 1121–1132. Available at: https://doi.org/10.1126/science.194.4270.1121.

Heaton, T.J. et al. (2020) 'Marine20 - The Marine Radiocarbon Age Calibration Curve (0-55,000 cal BP)', *Radiocarbon*, 62(4), pp. 779–820. Available at: https://doi.org/10.1017/RDC.2020.68.

Heaton, T.J. et al. (2023) 'Marine radiocarbon calibration in polar regions: A simple approximate approach using marine20', *Radiocarbon*, 65(4), pp. 848–875. Available at: https://doi.org/10.1017/RDC.2023.42.

Hebbeln, D. (1992) 'Weichselian glacial history of the Svalbard area: corretaling the marine and terrestrial records', *Boreas*, 21, pp. 295–304. Available at: https://doi.org/10.1111/j.1502-3885.1992.tb00035.x.

Hebbeln, D. et al. (1994) 'Moisture supply for northern ice-sheet growth during the Last Glacial Maximum', *Nature*, 370(6488), pp. 357–360. Available at: https://doi.org/10.1038/370357a0.

Heinrich, H. (1988) 'Origin and consequences of cyclic ice rafting in the Northeast Atlantic Ocean during the past 130,000 years', *Quaternary Research*, 29(2), pp. 142–152. Available at: https://doi.org/10.1016/0033-5894(88)90057-9.

Hemming, S.R. (2004) 'Heinrich events: Massive late Pleistocene detritus layers of the North Atlantic and their global climate imprint', *Reviews of Geophysics*, 42(1). Available at: https://doi.org/10.1029/2003RG000128.

Hesse, R. et al. (1997) 'Asymmetrical turbid surface-plume deposition near ice-outlets of the Pleistocene Laurentide ice sheet in the Labrador Sea', *Geo-Marine Letters*, 17(3), pp. 179–187. Available at: https://doi.org/10.1007/s003670050024.

Hodell, D. et al. (2013) 'Response of Iberian Margin sediments to orbital and suborbital forcing over the past 420 ka', *Paleoceanography*, 28(1), pp. 185–199. Available at: https://doi.org/10.1002/palo.20017.

Hogg, A.G. et al. (2020) 'SHCal20 Southern Hemisphere Calibration, 0-55,000 Years cal BP', *Radiocarbon*, 62(4), pp. 759–778. Available at: https://doi.org/10.1017/RDC.2020.59.

Hossain, A. et al. (2021) 'Opening of the Fram Strait led to the establishment of a modern-like three-layer stratification in the Arctic Ocean during the Miocene', *Arktos*, 7(1–3), pp. 1–12. Available at: https://doi.org/10.1007/s41063-020-00079-8.

Hough, J.L. (1953) 'Pleistocene Climatic Record in a Pacific Ocean Core Sample', *The Journal of Geology*, 61(3), pp. 252–262.

Hughes, A. L. C., Gyllencreutz, R., Lohne, Ø. S., Mangerud, J., & Svendsen, J.-I. (2016). The last Eurasian ice sheets – a chronological database and time-slice reconstruction, DATED-1. *Boreas, 45*(1), 1–45. Available at: https://doi.org/10.1111/bor.12142

Ingólfsson, Ó., & Landvik, J. Y. (2013). The Svalbard–Barents Sea ice-sheet – Historical, current and future perspectives. *Quaternary Science Reviews, 64*, 33–60. Available at: https://doi.org/10.1016/j.quascirev.2012.11.034

Jakobsson, M. et al. (2007) 'The early Miocene onset of a ventilated circulation regime in the Arctic Ocean', *Nature*, 447(7147), pp. 986–990. Available at: https://doi.org/10.1038/nature05924.

Jakobsson, M. et al. (2014) 'Arctic Ocean glacial history', *Quaternary Science Reviews*, 92, pp. 40–67. Available at: https://doi.org/10.1016/j.quascirev.2013.07.033.

Jakobsson, M. et al. (2020) 'The International Bathymetric Chart of the Arctic Ocean Version 4.0', *Scientific Data*, 7(1), pp. 1–14. Available at: https://doi.org/10.1038/s41597-020-0520-9.

Jang, K. et al. (2021) 'Glacial and environmental changes in northern Svalbard over the last 16.3 ka inferred from neodymium isotopes', *Global and Planetary Change*, 201(March). Available at: https://doi.org/10.1016/j.gloplacha.2021.103483.

Jansen, J.H.F. et al. (1998) 'CORTEX, a shipboard XRF-scanner for element analyses in split sediment cores', *Marine Geology*, 151(1–4), pp. 143–153. Available at: https://doi.org/10.1016/S0025-3227(98)00074-7.

Jenkins, R. and Vries, J.L. (1970) *Practical X-ray Spectrometry*. Red Globe Press London. Available at: https://doi.org/doi.org/10.1007/978-1-349-00055-5.

Jessen, S.P. et al. (2010) 'A new Late Weichselian and Holocene marine chronology for the western Svalbard slope 30,000-0calyearsBP', *Quaternary Science Reviews*, 29, pp. 1301–1312. Available at: https://doi.org/https://doi.org/10.1016/j.quascirev.2010.02.020.

Jessen, S.P. and Rasmussen, T.L. (2019) 'Ice-rafting patterns on the western Svalbard slope 74–0 ka: interplay between ice-sheet activity, climate and ocean circulation', *Boreas*, 48(1), pp. 236–256. Available at: https://doi.org/10.1111/bor.12358.

Johannessen, O.M. (1986) 'BRIEF OVERVIEW OF THE PHYSICAL OCEANOGRAPHY', in *The Nordic Seas*, pp. 103–127. Available at: https://doi.org/https://doi.org/10.1007/978-1-4615-8035-5_4.

Johnsen, S.J. et al. (1992) 'recorded in a new Greenland IK2', 662(August), pp. 311–313.

Jokat, W. et al. (2016) 'Magnetic signature of North-East Greenland, the Morris Jesup Rise, the Yermak Plateau, the central Fram Strait: Constraints for the rift/drift history between Greenland and Svalbard since the Eocene', *Tectonophysics*, 691, pp. 98–109. Available at: https://doi.org/10.1016/j.tecto.2015.12.002.

Jordan, R.W., Cros, L. and Young, J.R. (2004) 'A revised classification scheme for living haptophytes', *Micropaleontology*, 50(SUPPL. 1), pp. 55–79. Available at: https://doi.org/10.2113/50.Suppl_1.55.

Kern, O.A. et al. (2019) 'XRF core scanning yields reliable semiquantitative data on the elemental composition of highly organic-rich sediments: Evidence from the Füramoos peat bog (Southern Germany)', *Science of the Total Environment*, 697, p. 134110. Available at: https://doi.org/10.1016/j.scitotenv.2019.134110.

Key, R.M. et al. (2004) 'A global ocean carbon climatology: Results from Global Data Analysis Project (GLODAP)', *Global Biogeochemical Cycles*, 18(4), pp. 1–23. Available at: https://doi.org/10.1029/2004GB002247.

King, E.L. et al. (1998) 'Glacigenic debris flows on the North Sea Trough Mouth Fan during ice stream maxima', *Marine Geology*, 152(1–3), pp. 217–246. Available at: https://doi.org/10.1016/S0025-3227(98)00072-3.

Kleiven, K.H., Kissel, C. and Laj, C. (2008) ‘Reduced North Atlantic deep water coeval with the glacial Lake Agassiz freshwater outburst’, *Science*, 319(January), pp. 64–69. Available at: https://doi.org/10.1126/science.1148924.

Klenke, M. and Schenke, H.W. (2002) ‘A new bathymetric model for the central Fram Strait’, *Marine Geophysical Researches*, 23(4), pp. 367–378. Available at: https://doi.org/10.1023/A:1025764206736.

Knies, J. et al. (2014) ‘Effect of early Pliocene uplift on late Pliocene cooling in the Arctic-Atlantic gateway’, *Earth and Planetary Science Letters*, 387, pp. 132–144. Available at: https://doi.org/10.1016/j.epsl.2013.11.007.

Knies, J. et al. (2018) ‘Nordic Seas polynyas and their role in preconditioning marine productivity during the Last Glacial Maximum’, *Nature Communications*, 9(1), pp. 1–10. Available at: https://doi.org/10.1038/s41467-018-06252-8.

Knies, J. and Vadakkepliyambatta, S. (2019) *19-3 CAGE Cruise report*. Available at: https://doi.org/https://doi.org/10.7557/cage.6911.

Knox, F. and McElroy, M.B. (1984) ‘Changes in atmospheric CO2: influence of the marine biota at high latitude.’, *Journal of Geophysical Research*, 89(D3), pp. 4629–4637. Available at: https://doi.org/10.1029/JD089iD03p04629.

Knutz, P.C. et al. (2002) ‘Glacimarine slope sedimentation, contourite drifts and bottom current pathways on the Barra Fan, UK North Atlantic margin’, *Marine Geology*, 188(1–2), pp. 129–146. Available at: https://doi.org/10.1016/S0025-3227(02)00278-5.

Kobashi, T. et al. (2007) ‘Precise timing and characterization of abrupt climate change 8200 years ago from air trapped in polar ice’, *Quaternary Science Reviews*, 26(9–10), pp. 1212–1222. Available at: https://doi.org/10.1016/j.quascirev.2007.01.009.

Kozdon, R. et al. (2009) ‘Intratest oxygen isotope variability in the planktonic foraminifer N. pachyderma: Real vs. apparent vital effects by ion microprobe’, *Chemical Geology*, 258(3–4), pp. 327–337. Available at: https://doi.org/10.1016/j.chemgeo.2008.10.032.

Kristensen, D.K., Rasmussen, T.L. and Koç, N. (2013) ‘Palaeoceanographic changes in the northern Barents Sea during the last 16 000 years – new constraints on the last deglaciation of the Svalbard – Barents Sea Ice Sheet’, *Boreas*, 42, pp. 798–813. Available at: https://doi.org/10.1111/j.1502-3885.2012.00307.x.

Kuhlbrodt, T. et al. (2007) ‘On the driving processes of the Atlantic meridional overturning circulation’, *Reviews of Geophysics*, 45(2). Available at: https://doi.org/10.1029/2004RG000166.

Kullenberg, B. (1948) ‘Piston Core Sampler’, *The International Hydrographic Review*, pp. 1006–1006. Available at: https://doi.org/10.1007/978-3-642-41714-6_162051.

Laberg, J.S. and Dowdeswell, J.A. (2016) ‘Glacigenic debris-flows on the Bear Island Trough-Mouth Fan, Barents Sea margin’, *Geological Society Memoir*, 46(1), pp. 367–368. Available at: https://doi.org/10.1144/M46.77.

Laberg, J.S., Johansen, R. and Bünz, S. (2012) *Submarine Mass Movements and Their Consequences*, *A Surging Behaviour of Glacigenic Debris Flows*. Available at:

https://doi.org/10.1007/978-94-007-2162-3.

Laberg, J.S. and Vorren, T.O. (1995) ‘Late Weichselian submarine debris flow deposits on the Bear Island Trough Mouth Fan.pdf’. Marine Geology 127, pp. 45–72. Available at: https://doi.org/https://doi.org/10.1016/0025-3227(95)00055-4.

Laberg, J.S. and Vorren, T.O. (1996) ‘The glacier-fed fan at the mouth of Storfjorden trough, western Barents Sea: A comparative study’, *International Journal of Earth Sciences*, 85(2), pp. 338–349. Available at: https://doi.org/10.1007/s005310050079.

Labeyrie, L.D. et al. (1992) ‘Changes in the vertical structure of the North Atlantic Ocean between glacial and modern times’, *Quaternary Science Reviews*, 11(4), pp. 401–413. Available at: https://doi.org/10.1016/0277-3791(92)90022-Z.

Labeyrie, L.D., Duplessy, J.C. and Blanc, P.L. (1987) ‘Variations in mode of formation and temperature of oceanic deep waters over the past 125,000 years’, *Nature*, 327, pp. 477–482. Available at: https://doi.org/https://doi.org/10.1038/327477a0.

Lambeck, K. et al. (2014) ‘Sea level and global ice volumes from the Last Glacial Maximum to the Holocene’, *Proceedings of the National Academy of Sciences of the United States of America*, 111(43), pp. 15296–15303. Available at: https://doi.org/10.1073/pnas.1411762111.

Landvik, J.Y. et al. (1998) ‘The he last glacial maximum of Svalbard and the Barents Sea area: Ice Sheet Extent and Configuration’, *Quaternary Science Reviews*, 17, pp. 43–75. Available at: https://doi.org/https://doi.org/10.1016/S0277-3791(97)00066-8.

Laskar, J. (2006) ‘Long-term solution for the insolation quantities of the Earth’, *Proceedings of the International Astronomical Union*, 2(14), p. 465. Available at: https://doi.org/10.1017/S1743921307011404.

Lekens, W.A.H. et al. (2005) ‘Laminated sediments preceding Heinrich event 1 in the Northern North Sea and Southern Norwegian Sea: Origin, processes and regional linkage’, *Marine Geology*, 216(1–2), pp. 27–50. Available at: https://doi.org/10.1016/j.margeo.2004.12.007.

Lekens, W.A.H. et al. (2006) ‘Meltwater and ice rafting in the southern Norwegian Sea between 20 and 40 calendar kyr B.P.: Implications for Fennoscandian Heinrich events’, *Paleoceanography*, 21(3), pp. 1–17. Available at: https://doi.org/10.1029/2005PA001228.

Libby, W.F. (1946) ‘Atmospheric Helium Three and Radiocarbon from Cosmic Radiation’, *Physical Review*, 69(11–12), pp. 671–672. Available at: https://doi.org/doi.org/10.1103/PhysRev.69.671.2.

Libby, W.F., Anderson, E.C. and Arnold, J.R. (1949) ‘Age determination by radiocarbon content: World-wide assay of natural radiocarbon’, *Science*, 109(2827), pp. 227–228. Available at: https://doi.org/10.1126/science.109.2827.227.

Lin, Y. et al. (2021) ‘A reconciled solution of Meltwater Pulse 1A sources using sea-level fingerprinting’, *Nature communications*, 12(1), p. 2015. Available at: https://doi.org/10.1038/s41467-021-21990-y.

Liu, J.P. and Milliman, J.D. (2004) ‘Reconsidering melt-water pulses 1A and 1B: Global impacts of rapid sea-level rise’, *Journal of Ocean University of China*, 3(2), pp. 183–190. Available at: https://doi.org/10.1007/s11802-004-0033-8.

Lucchi, R.G. et al. (2002) ‘Mid-late Pleistocene glacumarine sedimentaryu processes of a hight-latitude, deep-sea sediment drift.pdf’. Marine Geology 189, pp. 343–370.

Lucchi, R.G. et al. (2013) ‘Postglacial sedimentary processes on the Storfjorden and Kveithola trough mouth fans: Significance of extreme glacimarine sedimentation’, *Global and Planetary Change*, 111, pp. 309–326. Available at: https://doi.org/10.1016/j.gloplacha.2013.10.008.

Lucchi, R.G. et al. (2014) *EUROFLEETS-2 Cruise Summary Report. PREPARED Present and past flow regime. On contourite drifts west of Spitsbergen*. Available at: https://www.researchgate.net/publication/266556598_PREPARED_Present_and_past_flow_regime._On_contourite_drifts_west_of_Spitsbergen.

Lucchi, R.G. et al. (2015) ‘Marine sedimentary record of Meltwater Pulse 1a along the NW Barents Sea continental margin’, *Arktos*, 1(1). Available at: https://doi.org/10.1007/s41063-015-0008-6.

Lucchi, R.G. et al. (2021) *Project Cruise Report - IRIDYA: Integrated reconstruction of ice sheet dynamics during Late Quaternary Arctic climatic transitions*. Available at: https://doi.org/10.13120/5e6d8d78-ad64-4bcb- 9023-.

Lucchi, R.G., St. John, K. and Ronge, T.A. (2023) '*Expedition 403 Scientific Prospectus: Eastern Fram Strait Paleo-Archive (FRAME)*, *International Ocean Discovery Program'*. Available at: https://doi.org/https://doi.org/10.14379/iodp.sp.403.2023.

Manabe, S. and Stouffer, R.B. (1995) ‘Freshwater input to the North Atlantic Ocean’, *Nature*, 378(1980), pp. 165–167.

Mangerud, J. et al., (1996). 'Late Cenozoic history of the Scandi- navian and Barents Sea ice sheets', Global and Planetary Change 12, pp. 11-26. Available at: http://doi:10.1016/0921-8181(95)00009-7.

Mangerud, J. et al. (2006) ‘Marine 14C reservoir ages for 19th century whales and molluscs from the North Atlantic’, *Quaternary Science Reviews*, 25(23–24), pp. 3228–3245. Available at: https://doi.org/10.1016/j.quascirev.2006.03.010.

Martínez, I. et al. (2003) ‘La Niña-like conditions in the eastern equatorial Pacific and a stronger Choco jet in the northern Andes during the last glaciation’, *Paleoceanography*, 18(2). Available at: https://doi.org/10.1029/2002PA000877.

März, C. et al. (2011) ‘Manganese-rich brown layers in Arctic Ocean sediments: Composition, formation mechanisms, and diagenetic overprint’, *Geochimica et Cosmochimica Acta*, 75(23), pp. 7668–7687. Available at: https://doi.org/10.1016/j.gca.2011.09.046.

Meland, M.Y. et al. (2008) ‘Water mass properties and exchange between the Nordic seas and the northern North Atlantic during the period 23-6 ka: Benthic oxygen isotopic evidence’, *Paleoceanography*, 23(1). Available at:

https://doi.org/10.1029/2007PA001416.

Melis, R. et al. (2018) ‘A new multi-proxy investigation of Late Quaternary palaeoenvironments along the north-western Barents Sea (Storfjorden Trough Mouth Fan)’, *Journal of Quaternary Science*, 33(6), pp. 662–676. Available at: https://doi.org/10.1002/jqs.3043.

Mesa-Fernández, J.M. et al. (2022) ‘Paleocirculation and paleoclimate conditions in the western Mediterranean basins over the last deglaciation: New insights from sediment composition variations’, *Global and Planetary Change*, 209(May 2021). Available at: https://doi.org/10.1016/j.gloplacha.2021.103732.

Milne, G.A. and Mitrovica, J.X. (2008) ‘Searching for eustasy in deglacial sea-level histories’, *Quaternary Science Reviews*, 27(25–26), pp. 2292–2302. Available at: https://doi.org/10.1016/j.quascirev.2008.08.018.

Mix, A.C., Bard, E. and Schneider, R. (2001) ‘Environmental processes of the ice age: Land, oceans, glaciers (EPILOG)’, *Quaternary Science Reviews*, pp. 627–657. Available at: https://doi.org/10.1016/S0277-3791(00)00145-1.

Montaggioni, L.F. et al. (1997) ‘Continuous record of reef growth over the past 14 k.y. On the mid-Pacific island of Tahiti: Reply’, *Geology*, 25, pp. 555–558. Available at: https://doi.org/10.1130/0091-7613(1998)026<0479:CRORGO>2.3.CO;2.

Müller, J. et al. (2009) ‘Variability of sea-ice conditions in the Fram Strait over the past 30,000 years’, *Nature Geoscience*, 2(11), pp. 772–776. Available at: https://doi.org/10.1038/ngeo665.

Müller, Juliane and Stein, R. (2014) ‘High-resolution record of late glacial and deglacial sea ice changes in Fram Strait corroborates ice-ocean interactions during abrupt climate shifts’, *Earth and Planetary Science Letters*, 403, pp. 446–455. Available at: https://doi.org/10.1016/j.epsl.2014.07.016.

Müller, J. and Stein, R. (2014) ‘High-resolution record of late glacial and deglacial sea ice changes in Fram Strait corroborates ice ocean interactions during abrupt climate shifts.pdf’, *Earth and Planetary Science Letters*, 403, pp. 446–455.

Munsell (2009). *Munsell soil color charts*. Grand Rapids, MI: Munsell Color, X-Rite, Incorporated.

Nilsen, J. and Nilsen, F. (2007) 'The Atlantic Water flow along the Vøring Plateau: Detecting frontal structures in oceanic station time series', Deep-Sea Res. I, 54, 297–319, Available at: https://doi:10.1016/ j.dsr.2006.12.012.

Nielsen, T. and Rasmussen, T.L. (2018) ‘Reconstruction of ice sheet retreat after the Last Glacial maximum in Storfjorden, southern Svalbard’, *Marine Geology*, 402(December 2017), pp. 228–243. Available at: https://doi.org/10.1016/j.margeo.2017.12.003.

Nieuwenhuize, J., Maas, Y.E.M. and Middelburg, J.J. (1994) ‘Rapid analysis of organic carbon and nitrogen in particulate materials’, *Marine Chemistry*, 45(3), pp. 217–224. Available at: https://doi.org/10.1016/0304-4203(94)90005-1.

Nilsen, F. et al. (2016) ‘A simple shelf circulation model: Intrusion of Atlantic water on the West Spitsbergen Shelf’, *Journal of Physical Oceanography*, 46(4), pp. 1209–1230. Available at: https://doi.org/10.1175/JPO-D-15-0058.1.

Nygård, A. et al. (2005) ‘The glacial North Sea Fan, southern Norwegian Margin: Architecture and evolution from the upper continental slope to the deep-sea basin’, *Marine and Petroleum Geology*, 22(1-2 SPEC. ISS.), pp. 71–84. Available at: https://doi.org/10.1016/j.marpetgeo.2004.12.001.

Ó Cofaigh, C. et al. (2013) ‘Glacimarine lithofacies, provenance and depositional processes on a West Greenland trough-mouth fan’, *Journal of Quaternary Science*, 28(1), pp. 13–26. Available at: https://doi.org/10.1002/jqs.2569.

Ó Cofaigh, C. et al. (2018) ‘The role of meltwater in high-latitude trough-mouth fan development: The Disko Trough-Mouth Fan, West Greenland’, *Marine Geology*, 402(January), pp. 17–32. Available at: https://doi.org/10.1016/j.margeo.2018.02.001.

Ottesen, D., Dowdeswell, J.A. and Rise, L. (2005) ‘Submarine landforms and the reconstruction of fast-flowing ice streams within a large Quaternary ice sheet: The 2500-km-long Norwegian-Svalbard margin (57°-80°N)’, *Bulletin of the Geological Society of America*, 117(7–8), pp. 1033–1050. Available at: https://doi.org/10.1130/B25577.1.

Patton, H. et al. (2016) ‘The build-up, configuration, and dynamical sensitivity of the Eurasian ice-sheet complex to Late Weichselian climatic and oceanic forcing’, *Quaternary Science Reviews*, 153, pp. 97–121. Available at: https://doi.org/10.1016/j.quascirev.2016.10.009.

Patton, H. et al. (2017) ‘Deglaciation of the Eurasian ice sheet complex’, *Quaternary Science Reviews*, 169, pp. 148–172. Available at: https://doi.org/10.1016/j.quascirev.2017.05.019.

Pedro, J.B. et al. (2022) ‘Dansgaard-Oeschger and Heinrich event temperature anomalies in the North Atlantic set by sea ice, frontal position and thermocline structure’, *Quaternary Science Reviews*, 289. Available at: https://doi.org/10.1016/j.quascirev.2022.107599.

Pedrosa, M.T. et al. (2011) ‘Seabed morphology and shallow sedimentary structure of the storfjorden and kveithola trough-mouth fans (north west barents sea)’, *Marine Geology*, 286(1–4), pp. 65–81. Available at: https://doi.org/10.1016/j.margeo.2011.05.009.

Pella, E. and Colombo, B. (1973) ‘Study of carbon, hydrogen and nitrogen determination by combustion-gas chromatography’, *Mikrochimica Acta*, 61(5), pp. 697–719. Available at: https://doi.org/10.1007/BF01218130.

Phleger, F.B. (1951) ‘Part I. Foraminifera distribution’, *Memoir of the Geological Society of America*, 46(1), pp. 1–83. Available at: https://doi.org/10.1130/MEM46-p1-0001.

Phleger, F.B., Parker, F.L. and Peirson, J.F. (1953) ‘Title North Atlantic foraminifera’, *Swedish Deep-Sea Exped., R*, pp. 3–122.

Plaza-Faverola, A. et al. (2023) ‘Spatial Changes in Gas Transport and Sediment Stiffness Influenced by Regional Stress: Observations From Piezometer Data Along Vestnesa Ridge, Eastern Fram Strait’, *Journal of Geophysical Research: Solid Earth*, 128(5), pp. 1–21. Available at: https://doi.org/10.1029/2022JB025868.

Rae, J.W.B. et al. (2014) ‘Deep water formation in the North Pacific and deglacial CO2 rise’, *Paleoceanography*, 29(6), pp. 645–667. Available at: https://doi.org/10.1002/2013PA002570.

Rahmstorf, S. (1995) ‘Bifurcations of the Atlantic thermohaline circulation in response to changes in the hydrological cycle’, *Nature*, 378(6553), pp. 145–149. Available at: https://doi.org/10.1038/378145a0.

Rahmstorf, S. (2002) ‘Ocean circulation and climate during the past 120,000 years’, *Nature*, 419(September), pp. 207–214. Available at: https://doi.org/https://doi.org/10.1038/nature01090.

Rahmstorf, S. et al. (2015) ‘Exceptional twentieth-century slowdown in Atlantic Ocean overturning circulation’, *Nature Climate Change*, 5(5), pp. 475–480. Available at: https://doi.org/10.1038/nclimate2554.

Ramsey, C.B. (2009) ‘Bayesian analysis of radiocarbon dates’, *Radiocarbon*, 51(1), pp. 337–360. Available at: https://doi.org/10.1017/s0033822200033865.

Rashid, H. et al. (2019) ‘Sedimentology and history of sediment sources to the NW Labrador Sea during the past glacial cycle’, *Quaternary Science Reviews*, 221, p. 105880. Available at: https://doi.org/10.1016/j.quascirev.2019.105880.

Rasmussen, S.O. et al. (2014) ‘A stratigraphic framework for abrupt climatic changes during the Last Glacial period based on three synchronized Greenland ice-core records: Refining and extending the INTIMATE event stratigraphy’, *Quaternary Science Reviews*, 106, pp. 14–28. Available at: https://doi.org/10.1016/j.quascirev.2014.09.007.

Rasmussen, T. et al. (2007) ‘Paleoceanographic evolution of the SW Svalbard margin (76 ° N) since 20 , 000 14 C yr BP’, *Quaternary Research*, 67, pp. 100–114. Available at: https://doi.org/10.1016/j.yqres.2006.07.002.

Rasmussen, T.L. et al. (2014) ‘Spatial and temporal distribution of Holocene temperature maxima in the northern Nordic seas : interplay of Atlantic- , Arctic- and polar water masses’, *Quaternary Science Reviews*, 92, pp. 280–291. Available at: https://doi.org/10.1016/j.quascirev.2013.10.034.

Rasmussen, T.L. and Thomsen, E. (2008) ‘Warm Atlantic surface water inflow to the Nordic seas 34-10 calibrated ka B.P’, *Paleoceanography*, 23(1), pp. 0–13. Available at: https://doi.org/10.1029/2007PA001453.

Rebesco, M. et al. (2011) ‘Deglaciation of the western margin of the Barents Sea Ice Sheet - A swath bathymetric and sub-bottom seismic study from the Kveithola Trough’, *Marine Geology*. Marine Geology, pp. 141–147. Available at: https://doi.org/10.1016/j.margeo.2010.10.018.

Rebesco, M. et al. (2013) ‘Onset and growth of Trough-Mouth Fans on the North-

Western Barents Sea margin e implications for the evolution of the Barents Sea/Svalbard Ice Sheet', *Quaternary Science Reviews*, 92, pp. 227–234. Available at: https://doi.org/http://dx.doi.org/10.1016/j.quascirev.2013.08.015.

Rebesco, Michele et al. (2013) 'Quaternary contourite drifts of the Western Spitsbergen margin', *Deep-Sea Research Part I: Oceanographic Research Papers*, 79, pp. 156–168. Available at: https://doi.org/10.1016/j.dsr.2013.05.013.

Reimer, P.J. et al. (2020) 'The IntCal20 Northern Hemisphere Radiocarbon Age Calibration Curve (0-55 cal kBP)', *Radiocarbon*, 62(4), pp. 725–757. Available at: https://doi.org/10.1017/RDC.2020.41.

Rigual-Hernández, A.S. et al. (2017) 'Svalbard ice-sheet decay after the Last Glacial Maximum: New insights from micropalaeontological and organic biomarker paleoceanographical reconstructions', *Palaeogeography, Palaeoclimatology, Palaeoecology*, 465, pp. 225–236. Available at: https://doi.org/10.1016/j.palaeo.2016.10.034.

Rinterknecht, V. et al. (2006) 'The last deglaciation of Alaska', *Science*, 311, pp. 1449–1452. Available at: https://doi.org/10.18172/cig.3229.

Risebrobakken, B. et al. (2011) 'Early Holocene temperature variability in the Nordic Seas : The role of oceanic heat advection versus changes in orbital forcing', *Palaeogeography, Palaeoclimatology, Palaeoecology*, 26. Available at: https://doi.org/10.1029/2011PA002117.

Rohling, E.J. and Pa, H. (2005) 'Centennial-scale climate cooling with a sudden cold event around 8,200 years ago', *Nature*, 434(April), pp. 975–979. Available at: https://doi.org/doi.org/10.1038/nature03421.

Rosenthal, Y., Boyle, E. a and Labeyrie, L. (1997) 'Last glacial maximum paleochemistry and deepwater circulation Ocean : Evidence from foraminiferal cadmium', *Paleoceanography*, 12(6), pp. 787–796. Available at: https://doi.org/https://doi.org/10.1029/97PA02508.

S´ lubowska-Woldengen, M. et al. (2008) 'Time-slice reconstructions of ocean circulation changes on the continental shelf in the Nordic and Barents Seas during the last 16 , 000 cal yr B . P .', *Quaternary Science Reviews*, 27, pp. 1476–1492. Available at: https://doi.org/10.1016/j.quascirev.2008.04.015.

Sarmiento, J.L. and Toggweiler, J.R. (1984) 'A new model for the role of the oceans in determining atmospheric pC02', *Nature*, 308, pp. 621–624.

Sarnthein, M. and Grootes, P.M. (2013) 'of the Past Peak glacial 14 C ventilation ages suggest major draw-down of carbon into the abyssal ocean', *Climate of the Past*, 9, pp. 2595–2614. Available at: https://doi.org/10.5194/cp-9-2595-2013.

Saupe, A. et al. (2023) 'Benthic foraminifera in high latitude contourite drift systems (North Atlantic: Björn, Gardar and Eirik drifts)', *Palaeogeography, Palaeoclimatology, Palaeoecology*, 609(September 2022). Available at: https://doi.org/10.1016/j.palaeo.2022.111312.

Schauer, U. et al. (2004) 'Arctic warming through the Fram Strait: Oceanic heat transport from 3 years of measurements', *Journal of Geophysical Research: Oceans*, 109(6), pp. 1–14. Available at: https://doi.org/10.1029/2003JC001823.

Schneider, C.A., Rasband, W.S., Eliceiri, K.W (2012). "NIH Image to ImageJ: 25 years of image analysis". Nature Methods 9, 671-675, 2012. Available at: https://doi.org/10.1038/nmeth.2089.

Schott, W. (1952) 'Zur Klimaschichtung der Tiefseesedimente Im äquatorialen Atlantischen Ozean', *Geologische Rundschau*, 40(1), pp. 20–31. Available at: https://doi.org/10.1007/bf01803204.

Scourse, J.D. et al. (2000) 'The origin of Heinrich layers: Evidence from H2 for European precursor events', *Earth and Planetary Science Letters*, 182(2), pp. 187–195. Available at: https://doi.org/10.1016/S0012-821X(00)00241-7.

Seierstad, I.K. et al. (2005) 'The duration of the Bølling-Allerød period (Greenland Interstadial 1) in the GRIP ice core', *Annals of Glaciology*, 42(3), pp. 337–344. Available at: https://doi.org/10.3189/172756405781812556.

Seigenthaler, U. and Wenk, T. (1984) 'Rapid atmospheric CO2 variations and ocean circulation', *Nature*, 308, pp. 12–14.

Shackleton, N.J. (1967) 'Oxygen Isotope Analyses and Pleistocene Temperatures Re-assessed', *Nature Publishing Group*, 215, pp. 15–17. Available at: https://doi.org/DOI:10.1038/215015A0.

Shakun, J.D. et al. (2012) 'Global warming preceded by increasing carbon dioxide concentrations during the last deglaciation', *Nature*, 484, pp. 49–54. Available at: https://doi.org/10.1038/nature10915.

Shakun, J.D. (2017) 'Modest global-scale cooling despite extensive early Pleistocene ice sheets', *Quaternary Science Reviews*, 165, pp. 25–30. Available at: https://doi.org/10.1016/j.quascirev.2017.04.010.

Sigman, D.M., Hain, M.P. and Haug, G.H. (2010) 'The polar ocean and glacial cycles in atmospheric CO 2 concentration', *Nature*, 466, pp. 47–55. Available at: https://doi.org/10.1038/nature09149.

Skinner, L.C. et al. (2010) 'Ventilation of the Deep Southern', *Science*, 328(May), pp. 1147–1151. Available at: https://doi.org/doi:10.1126/science.1183627.

Skinner, L.C. et al. (2017) 'Radiocarbon constraints on the glacial ocean circulation and its impact on atmospheric CO2', *Nature Communications*, 8(16010), pp. 1–10. Available at: https://doi.org/10.1038/ncomms16010.

Spahni, R. et al. (2003) ' The attenuation of fast atmospheric CH 4 variations recorded in polar ice cores ', *Geophysical Research Letters*, 30(11), pp. 2–5. Available at: https://doi.org/10.1029/2003gl017093.

Stanford, J.D. et al. (2006) 'Timing of meltwater pulse 1a and climate responses to meltwater injections', *Paleoceanography*, 21(4), pp. 1–9. Available at: https://doi.org/10.1029/2006PA001340.

Stärz, M. et al. (2017) 'Threshold in North Atlantic-Arctic Ocean circulation controlled by the subsidence of the Greenland-Scotland Ridge', *Nature Communications*, 8, pp. 1–13. Available at: https://doi.org/10.1038/ncomms15681.

Stocker, T.F. and Wright, D.G. (1991) 'Stocker & Wright (1991) Rapid transitions of the oceans deeo circulation indiced by changes in suface water fluxes.pdf', *Nature*, 351, pp. 729–732.

Stouffer, R.J. et al. (2006) 'Investigating the causes of the response of the thermohaline circulation to past and future climate changes', *Journal of Climate*, 19, pp. 1365–1387. Available at: https://doi.org/https://doi.org/10.1175/JCLI3689.1.

Stuiver, M. and Polach, H.A. (1977) 'Disscussion Reporting of 14C Data', *Radiocarbon*, 19(3), pp. 355–363. Available at: https://doi.org/doi.org/10.1017/S0033822200003672.

Swift, J.H. and Koltermann, K.P. (1988) 'The Origin of Norwegian Sea Deep Water', *Journal of Geophysical Research*, 93, pp. 3563–3569.

Tamura, T., Ohshima, K. and Nihashi, S. (2008) 'Mapping of sea ice production for Antarctic coastal polynyas', *Geophysical Research Letters*, 35(7), pp. 1–5. Available at: https://doi.org/10.1029/2007GL032903.

Taylor, J. et al. (2002) 'Late Quaternary architecture of trough-mouth fans: Debris flows and suspended sediments on the Norwegian margin', *Geological Society Special Publication*, 203, pp. 55–71. Available at: https://doi.org/10.1144/GSL.SP.2002.203.01.04.

Telford, R.J., Heegaard, E. and Birks, H.J.B. (2004) 'The intercept is a poor estimate of a calibrated radiocarbon age', *Holocene*, 14(2), pp. 296–298. Available at: https://doi.org/10.1191/0959683604hl707fa.

Thompson, B. et al. (2012) 'A model study of the first ventilated regime of the Arctic Ocean during the early Miocene', *Polar Research*, 31(1), p. 10859. Available at: https://doi.org/10.3402/polar.v31i0.10859.

Thomson, J., Croudace, I.W. and Rothwell, R.G. (2006) 'A geochemical application of the ITRAX scanner to a sediment core containing eastern Mediterranean sapropel units', *Geological Society Special Publication*, 267, pp. 65–77. Available at: https://doi.org/10.1144/GSL.SP.2006.267.01.05.

Toggweiler, J.R., Russell, J.L. and Carson, S.R. (2006) 'Midlatitude westerlies , atmospheric CO 2 , and climate change during the ice ages', 21(April), pp. 1–15. Available at: https://doi.org/10.1029/2005PA001154.

Torell, O., (1878). 'On the causes of the glacial phenomena', Kungliga Svenska Vetenskapsakademiens Förhandlingar 5, 1e7.

Törnqvist, T.E. and Hijma, M.P. (2012) 'Links between early Holocene ice-sheet decay, sea-level rise and abrupt climate change', *Nature Geoscience*, 5(9), pp. 601–606. Available at: https://doi.org/10.1038/ngeo1536.

Tripsanas, E.K. and Piper, D.J.W. (2008) 'Glaciogenic debris-flow deposits of orphan basin, offshore eastern Canada: Sedimentological and rheological properties, origin, and relationship to meltwater discharge', *Journal of Sedimentary Research*, 78(11–

12), pp. 724–744. Available at: https://doi.org/10.2110/jsr.2008.082.

Vilanova, I. et al. (2019) 'The last glacial termination in the Coyhaique sector of central Patagonia', *Quaternary Science Reviews*. Available at: https://doi.org/10.1016/j.quascirev.2019.105976.

Vorren, T.O. et al. (1989) 'Glacigenic sediments on a passive continental margin as exemplified by the Barents Sea', *Marine Geology*, pp. 251–272. Available at: https://doi.org/10.1016/0025-3227(89)90156-4.

Vorren, T.O. and Laberg, J.S. (1997) 'Trough Mouth Fans - Paleocimate and ice-sheet monitors.pdf'. Quaternary Science Reviews 16, pp. 865–881.

De Vries, H. (1958) *Variation in concentration of radiocarbon with time and local on earth*, *Koninkl. Nederlandse Acad.*

Weaver, A.J. et al. (2003) 'Meltwater pulse 1A from Antarctica as a trigger of the Bølling-Allerød warm interval', *Science*, 299(5613), pp. 1709–1713. Available at: https://doi.org/10.1126/science.1081002.

Weber, M.E. et al. (2010) 'BMPix and PEAK tools: New methods for automated laminae recognition and counting-Application to glacial varves from Antarctic marine sediment', *Geochemistry, Geophysics, Geosystems*, 11(3), pp. 1–18. Available at: https://doi.org/10.1029/2009GC002611.

Weber, M.E. et al. (2011) 'Interhemispheric ice-sheet synchronicity during the last glacial maximum', *Science*, 334(6060), pp. 1265–1269. Available at: https://doi.org/10.1126/science.1209299.

Webster, J.M. *et al.* (2004) 'Drowning of the - 150 m reef off Hawaii: A casualty of global meltwater pulse 1A?', *Geology*, 32(3), pp. 249–252. Available at: https://doi.org/10.1130/G20170.1.

Werner, K., Spielhagen, Robert F, et al. (2013) 'Atlantic Water advection versus sea-ice advances in the eastern Fram Strait during the last 9 ka : Multiproxy evidence for a two- phase Holocene', *Paleoceanography*, 28, pp. 283–295. Available at: https://doi.org/10.1002/palo.20028.

Werner, K., Spielhagen, Robert F., et al. (2013) 'Atlantic Water advection versus sea-ice advances in the eastern Fram Strait during the last 9 ka: Multiproxy evidence for a two-phase Holocene', *Paleoceanography*, 28(2), pp. 283–295. Available at: https://doi.org/10.1002/palo.20028.

Whitehouse, P.L. and Bradley, S.L. (2013) *Eustatic Sea-Level Changes Since the Last Glacial Maximum*. 2nd edn, *Encyclopedia of Quaternary Science: Second Edition*. 2nd edn. Elsevier B.V. Available at: https://doi.org/10.1016/B978-0-444-53643-3.00131-X.

Willis, E.H., Tauber, H. and Münnich, K.O. (1960) 'Variations in the Atmospheric Radiocarbon Concentration over the Past 1300 Years', *American Journal of Science. Radiocarbon Supplement*, 2, pp. 1–4. Available at: https://doi.org/10.1017/s1061592x00020548.

Wu, L. et al. (2020) 'Evaluating Zr/Rb Ratio From XRF Scanning as an Indicator of

Grain-Size Variations of Glaciomarine Sediments in the Southern Ocean', *Geochemistry, Geophysics, Geosystems*, 21(11), pp. 1–26. Available at: https://doi.org/10.1029/2020GC009350.

Yokoyama, Y. et al. (2000) 'Timing of the Last Glacial Maximum from observed sea-level minima', *Nature*, pp. 713–716. Available at: https://doi.org/10.1038/35021035.

Young, J.R. et al. (2003) 'A guide to extant coccolithophore taxonomy.', *Journal of Nannoplankton Research*, S1(October 2017), pp. 1–132. Available at: https://doi.org/10.58998/jnr2297.

Zeuner, F.E. (1950) 'Dating the past by radioactive carbon', *Nature*, 166(4227), pp. 756–757. Available at: https://doi.org/10.1038/166756a0.

Appendix

Summary table of analysis, instruments and quantity of samples used for the study.

Analysis	Micropaleontological	IRD	Oxygen stable isotopes	14C Age dating	Nano fossils	Ca/Mg	OM	CaCO3	CHN
Location	DST UNIPI	DST UNIPI	University of Cambridge - UK	Woods Hole Oceanographic Institution - USA	INGV PISA	Rutgers University - EUA	OGS-BIO	OGS-BIO	OGS-BIO
Equipment	Binocular Microscope	Binocular Microscope	Thermo MAT253 IRMS coupled to a Kiel IV	Continuous-Flow AMS System	Light-polarized microscope	Thermo Element ICP-MS-XR	ECS 4010, Costech	ECS 4010, Costech	ECS 4010, Costech
Quantity	301	234	224	19	23	7	205	205	205